



Technische Universität Ilmenau
Fakultät für Elektrotechnik und Informationstechnik

**Profile simulations of plasma etching of silicon under
consideration of charging effect and cryogenic condition**

Dissertation

Zur Erlangung des akademischen Grades

Doktor-Ingenieur

(Dr.-Ing.)

vorgelegt der Fakultät für Elektrotechnik und Informationstechnik
der Technischen Universität Ilmenau

von

Dipl.-Ing. Valentyn Ishchuk

geboren am 23 November 1981 in Kiew (Ukraine)

eingereicht am 4. Dezember 2013

1. Gutachter: Prof. Dr.-Ing. habil. Ivo W. Rangelow (Technische Universität Ilmenau)
2. Gutachter: Prof. Dr. rer. nat. Gerhard Franz (Hochschule München)
3. Gutachter: Dr. Deirdre Olynick (Lawrence Berkeley National Laboratory, USA)

Verteidigung am: 1. Juli 2014

angefertigt am

Fachgebiet Mikro- und Nanoelektronische Systeme
Technische Universität Ilmenau
Ilmenau, 2014



Ilmenau University of Technology
Faculty of Electrical Engineering and Information Technology

**Profile simulations of plasma etching of silicon under
consideration of charging effect and cryogenic condition**

Dissertation

by

Dipl.-Ing. Valentyn Ishchuk
born on 23 November 1981 in Kyiv (Ukraine)

A dissertation submitted to
Faculty of Electrical Engineering and Information Technology
at Ilmenau University of Technology
in partial fulfillment of the requirements for the degree of

**Doctor of Philosophy
(Dr.-Ing.)**

submitted on 4 December 2013

- 1. Reviewer: Prof. Dr.-Ing. habil. Ivo W. Rangelow (supervisor)
- 2. Reviewer: Prof. Dr. rer. nat. Gerhard Franz
- 3. Reviewer: Dr. Deirdre Olynick

Day of the defense: 1 July 2014

Department of Microelectronic and Nanoelectronic Systems,
Ilmenau University of Technology
Ilmenau, 2014

Reviewers:

1. **Prof. Dr. -Ing. habil. Ivo W. Rangelow** (supervisor)
*(Department of Microelectronic and Nanoelectronic Systems,
Faculty of Electrical Engineering and Information Technology,
Ilmenau University of Technology,
Ilmenau, Thuringia, Germany)*
2. **Prof. Dr. rer. nat. Gerhard Franz**
*(Department of Applied Sciences and Mechatronics,
Munich University of Applied Sciences,
Munich, Bavaria, Germany)*
3. **Dr. Deirdre Olynick**
*Nanofabrication Facility, The Molecular Foundry,
Ernest Orlando Lawrence Berkeley National Laboratory,
Berkeley, California, USA*

This thesis is dedicated to:

my father Mykola Ishchuk,

my mother Olena Ishchuk,

my sister Ira,

my wife Tanya and my son Igor



Цю роботу я присвячую:

моєму батькові Миколі Іщуку,

моїй матері Олені Іщук,

моїй сестрі Ірі,

моїй дружині Тані та моєму сину Ігорю

Acknowledgements

I would like to express my sincere gratitude to my supervisor, Prof. Dr. Ivo W. Rangelow, who took me into his group. I couldn't really ask for a better advisor. Being an amazing scientist, Prof. Rangelow has been for me more than just an advisor, he has been an incredible mentor. Without his work and support, without his constant encouragement and enthusiasm, there is no way I would be where I am. I really appreciate it all. Prof. Rangelow also put me in contact and collaboration with many scientists of universities or research institutes across the globe. As a result, I have obtained a lot of experience while visiting best plasma etching research companies and laboratories in Europe. Moreover, the successful collaboration with the Lawrence Berkeley National Laboratory (LBNL), California, USA has made a great contribution to my work and experience.

My sincere thanks go to the members of our workgroup (present and past), Dr. Burkhard Volland, Dr. Maik Hauguth, Alexander Reum and Tim Gnörrlich, for the intensive exchange of ideas during the work, as well as for their really valuable contributions to the program code implementation of our simulation software. Special thanks go to Dr. Volland for his support and always comprehensive advisory. Our fruitful discussions while addressing various scientific problems have significantly extended my knowledge in many aspects of physics, chemistry and mathematics, which was critically important for my work. I am very thankful to Dr. Hauguth for his valuable suggestions regarding software development. His very good expertise in this field has always been for me a constant source of motivation to improve my skills in programming techniques.

I would like to acknowledge the funding in frame of the European research project NanoPlasma by the European Commission Sixth Framework Programme (Contract No.016424). In the context of the project, I truly enjoyed the collaborative work with Dr. Mike Cooke and Dr. Andy Goodyear from Oxford Instruments Plasma Technology, Bristol, UK, as well as the cooperation with Dr. George Kokkoris and Dr. Evangelos Gogolides from IMEL Demokritos Institute, Athens, Greece. Special thanks go to Dr. Mike Cooke for providing the experimental data, that I used for validation of the developed charging effect simulation model.

My sincere thanks go to Dr. Deirdre Olynick, a staff scientist at Molecular Foundry, Lawrence Berkeley National Laboratory (LBNL), for such a valuable collaboration and for her very good support during my stay in Berkeley. I would like to acknowledge the funding by the Lawrence Berkeley National Laboratory, which gave me the great possibility to spend unforgettable 6 months in California, conducting plasma etching experiments at the Nanofabrication facility, Molecular Foundry, LBNL in Berkeley. During the stay, I gained a lot of useful practical experience while working in cleanroom, especially with cryogenic ICP plasma etcher and scanning electron microscope. Also, I am very thankful to Dr. Zuwei Liu from Oxford Instruments Plasma Technology, USA, for his experimental results that I used for calibration of the developed cryogenic silicon etching model.

I wish also to thank Dr. John W. Coburn – one of the most well-known and successful scientists in the field of plasma etching technology – for his helpful suggestions during our discussions in Berkeley.

I would like to thank all my colleagues from the *Department of Micro- and Nanoelectronic Systems* at Ilmenau University of Technology, past and present, especially Dr. Elshad Guliyev, Manuel Hofer, Dr. Maik Hauguth, Alexander Reum, Ahmad Ahmad, Dr. Tzvetan Ivanov, Dr. Yanko Sarov, Dr. Stefan Klett and Dr. Jens-Peter Zöllner for the enjoyable atmosphere during my work. Also thanks to all the excellent staff at Ilmenau University of Technology, who always were willing to contribute their time to help out.

My special thanks go to my friends in Ilmenau, Elshad Guliyev, Marat Karibayev and Patrick Mäder, who supported, encouraged and inspired me throughout all my work. Thanks for all, for our research discussions, going in for sport, or just having fun – without you, guys, my stay in Ilmenau would never have been so pleasant and memorable. Also, I would like to thank my very good old friends, Oleksii Fedorenko, Igor Vytyaz, Olexandr Protsyuk and Viktor Solodiy for being who they are and for the time we spend together.

My sincere thanks go to my father, Mykola Ishchuk (who dreamed about the successful completion of this thesis at least as well as I did), and my beloved mother, Olena Ishchuk, for their love, tireless support and understanding. I am grateful to them for everything they taught me, that helped me to make my dream come true. Also, I am thankful for the support and love I received from my sister Ira, my grandmother Valentina and my grandfather Evgeniy.

Finally, I am most grateful to my wonderful and beloved wife Tanya for her patience and understanding. She inspired, supported and encouraged me throughout all these years. I thank her for her love and for all the sacrifices she has made for us. Special thanks to my little son, Igor, who has become an additional and very important source of inspiration for me.

*Valentyn Ishchuk
November 2013
Ilmenau, Germany*

Selbstständigkeitserklärung

Ich versichere, dass ich die vorliegende Arbeit ohne unzulässige Hilfe Dritter und ohne Benutzung anderer als der angegebenen Hilfsmittel angefertigt habe. Die aus anderen Quellen direkt oder indirekt übernommenen Daten und Konzepte sind unter Angabe der Quelle gekennzeichnet. Weitere Personen waren an der inhaltlich-materiellen Erstellung der vorliegenden Arbeit nicht beteiligt gewesen. Insbesondere habe ich hierfür nicht die entgeltliche Hilfe von Vermittlungs- beziehungsweise Beratungsdiensten (Promotionsberater oder anderer Personen) in Anspruch genommen. Niemand hat von mir unmittelbar oder mittelbar geldwerte Leistungen für Arbeiten erhalten, die im Zusammenhang mit dem Inhalte der vorgelegten Dissertation stehen. Die Arbeit wurde bisher weder im In- noch im Ausland in gleicher oder ähnlicher Form einer Prüfungsbehörde vorgelegt. Ich bin darauf hingewiesen worden, dass die Unrichtigkeit der vorstehenden Erklärung als Täuschungsversuch angesehen wird und den erfolglosen Abbruch des Promotionsverfahrens zur Folge hat.

Ilmenau, den 03. Dezember 2013

Declaration

I hereby declare that this submission is my own work and that, to the best of my knowledge and belief, it contains no material previously published or written by another person nor material which to a substantial extent has been accepted for the award of any other degree or diploma of the university or other institute of higher learning, except where due acknowledgement has been made in the text.

Ilmenau, December 3, 2013

Abstract

This work focuses on simulations of plasma etching of high aspect ratio (HAR) structures in silicon. Plasma etching technology plays a critical role for the production of microelectronic devices, and micro- and nanoelectronic systems (M(N)EMS). Due to the great complexity of physical and chemical phenomena occurring in the plasma reactor during the processing, plasma etching technique is still not fully understood. Economizing time and costs needed for numerous experiments in the context of the process development, simulation software can significantly help in the detailed investigation of the technology. **ViPER** simulator, developed by the MNES group at Ilmenau University of Technology, allows conducting virtual experiments where various secondary effects of plasma etching can be considered and analyzed for better insight into the process. In terms of the presented work, new models were developed for the **ViPER**, to address the following two objectives: 1) simulation of the influence of local surface charging (charging effect) on the evolving feature profile; 2) simulation of cryogenic HAR silicon plasma etching.

For the first time, by utilizing the charging effect simulation model developed in this work, the influence of local charging of the microstructure insulating surfaces on the evolving feature profile was simulated over the entire course of the etching process and, *at the same time*, the obtained results were validated by comparison with real plasma etching experiment. The model simulates transport of charged particles in the intra-feature area accounting for the influence of local electric field induced by the local surface charging. By using finite element method (FEM) for electric field calculation, the model is able to handle complicated geometry of the area of interest which can often arise during the simulations. If needed, the developed model can also allow for electric field in the insulating materials of the sample. The particle trajectories are analytically calculated using the FEM mesh. A HAR etching experiment, employing a $\text{SF}_6/\text{C}_4\text{F}_8$ gas chopping process, was used for the validation. The model is general and can be applied across many etching chemistries.

For the first time, by using the developed in this work cryogenic silicon etching model, a low-temperature SF_6/O_2 plasma etching of nano-features (linewidth 35 nm) in silicon was simulated. The obtained results were tested with the real experimental data, showing a good agreement. Hence, the developed model is a very attractive tool for further research and development of sub-10 nm HAR nano patterning. The model provides feature scale (in the microstructure area) simulations without modelling the plasma within the entire reactor chamber. Thus, many of the model parameters (the arising plasma species, the plasma species' fluxes to the wafer, ion angular and energy distributions at the sample, sticking coefficients of plasma species arriving at the target surface, etc.) were assessed and calibrated. To this end, a large number of experiments was conducted in cooperation with the Lawrence Berkeley National Laboratory, California, USA. The internal model parameters were estimated by calibrations, where, using different configurations of plasma etch equipment parameters, cryogenic (-120°C) HAR etching of micro-features (1.5–0.5 μm) was simulated and tested with the corresponding experimental data.

Kurzfassung

Diese Arbeit befasst sich mit der Simulation von Plasmaätz-Prozessen zur Erzeugung von HAR-Strukturen (engl.: "high aspect ratio") in Silizium. Plasmaätz-Technologie spielt eine kritische Rolle für die Herstellung mikroelektronischer Geräte und mikro-/nano-elektromechanischer Systeme (M(N)EMS). Aufgrund der Komplexität physikalischer und chemischer Phänomene, welche während der Prozessierung im Plasmareaktor auftreten, ist die Technologie noch nicht vollständig verstanden. Simulationssoftware kann einen wesentlichen Beitrag zu deren Untersuchung leisten, indem sie Zeit und Kosten für eine Vielzahl von Experimenten zur Entwicklung von Plasmaätz-Prozessen reduziert. Der **ViPER** Simulator, der am Fachgebiet MNES der Technischen Universität Ilmenau entwickelt wurde, ermöglicht die Durchführung virtueller Experimente, in denen verschiedene sekundäre Effekte des Plasmaätzens zum besseren Verständnis des Prozesses berücksichtigt und analysiert werden können. In der vorliegenden Arbeit wurden neue Modelle für **ViPER** entwickelt, die folgenden Zielstellungen hatten: 1) Simulation des Einflusses von lokaler Aufladung (engl.: "charging effect") auf das entstehende Oberflächenprofil; 2) Simulation von kryogenischem HAR-Plasmaätzen von Silizium.

Erstmalig wurde der Einfluss der lokalen Aufladung an dielektrischen Oberflächen der Mikrostrukturen auf das entstehende Oberflächenprofil über die gesamte Dauer des Ätzprozesses simuliert und *gleichzeitig* mit den Ergebnissen realer Experimente validiert. Das Modell simuliert den Transport von geladenen Teilchen im Bereich der prozessierten Mikrostruktur unter Berücksichtigung lokaler elektrischer Felder, die durch den erwähnten Aufladungseffekt erzeugt werden. Durch die Nutzung der Finite-Elemente-Methode (FEM) zur Berechnung des elektrischen Feldes kann das Modell sehr gut mit komplexer Geometrie des betrachteten Bereichs umgehen, welche häufig während der Simulation auftritt. Falls nötig, kann das Modell elektrische Felder auch in dielektrischen Materialien der prozessierten Probe berücksichtigen. Teilchentrajektorien werden analytisch anhand des FEM-Netzes berechnet. Zur Validierung des Modells wurde ein HAR-Ätzexperiment auf Basis eines $\text{SF}_6/\text{C}_4\text{F}_8$ -Gas-Chopping-Prozesses genutzt. Das Modell ist allgemein und kann auf viele Ätzchemien angewendet werden.

Zum ersten Mal wurde ein Niedertemperatur- SF_6/O_2 -Plasmaätzprozess von Nanostrukturen (Linienbreite 35 nm) in Silizium unter Verwendung eines im Rahmen dieser Arbeit entwickelten Kryo-Ätzmodells simuliert. Die Ergebnisse boten eine gute Übereinstimmung mit experimentellen Daten. Das entwickelte Modell ist folglich ein sehr attraktives Werkzeug für die weitere Erforschung und Entwicklung der HAR-Nanostrukturierung unterhalb 10 nm. Es liefert Simulationen im Mikrostrukturbereich ohne das Plasma in der gesamten Reaktorkammer zu modellieren. Daher wurden viele Modellparameter geschätzt und kalibriert (die entstehenden Plasmaspezies und deren Flüsse zur Waferoberfläche, Winkel- und Energieverteilungen von einfallenden Ionen an der Probenoberfläche, etc.). Zu diesem Zweck wurde in Kooperation mit dem Lawrence Berkeley National Lab (Kalifornien, USA) eine Vielzahl von Experimenten durchgeführt. Die internen Modellparameter wurden bestimmt, indem kryogenisches HAR-Ätzen (-120°C , Linienbreite 1,5–0,5 μm) mit verschiedenen Ätzrezepten simuliert und mit Experimentaldaten verglichen wurde.

Contents

Acknowledgements	iv
Selbstständigkeitserklärung	v
Declaration	v
Abstract	vii
Kurzfassung	ix
1 Introduction	1
2 Plasma	5
2.1 Debye length	6
2.2 Temperature of plasma particles	7
2.3 Plasma oscillations	8
2.4 Potential distribution in plasma and plasma sheath	10
2.4.1 Floating potential	10
2.4.2 Presheath and the Bohm criterion	11
3 Plasma generation for material processing	15
3.1 Capacitively coupled plasma (CCP) sources	16
3.2 Inductively coupled plasma (ICP) sources	18
4 Plasma etching of silicon	21
4.1 Chemical etching	23
4.2 Sputtering	24

4.3	Ion-assisted etching	25
4.4	The role of sidewall passivation	27
4.5	Gas chopping etching technique	28
4.6	Cryogenic etching of silicon	29
4.7	Mixed mode technique	31
4.8	Summary	32
5	Transport phenomena	33
5.1	Transport across the sheath and particle angular distribution at the sample	33
5.2	Feature scale transport	34
5.2.1	Transport of neutral reactants	34
5.2.2	Ion transport	35
5.2.2.1	Charging effect	36
5.2.3	Pattern shape effects	36
6	ViPER simulation software	39
6.1	Motivation	39
6.2	Existing plasma etch simulators	40
6.3	ViPER simulator overview	41
6.3.1	Plasma bulk model	42
6.3.2	Plasma sheath model	43
6.3.3	Feature scale transport models	43
6.3.4	Surface reaction models and surface profile evolution	43
7	Charging effect simulation	45
7.1	Motivation	45
7.2	Position of the charging simulation model in the ViPER software architecture	47
7.3	General structure of the developed charging model	48
7.4	Definition of charging simulation area	50
7.5	Electric field calculation module	50
7.5.1	Definition of the boundary conditions	53
7.5.2	The finite element method (FEM) solver	56

7.5.2.1	The general FEM formulation	57
7.5.2.2	The FEM element-related formulation	62
7.5.2.3	Compilation of the FEM equation system	67
7.5.2.4	Consideration of the boundary integral	68
7.5.2.5	Meshing	70
7.6	Particle trajectories calculation	71
7.7	Results. Application of the implemented charging model	75
7.8	Conclusions to the developed charging model	79
8	Simulations of cryogenic silicon etching	81
8.1	Experiments	82
8.2	Simulations	82
8.2.1	State of the art	82
8.2.2	The implemented model	84
8.2.2.1	Plasma species and plasma sheath transport	84
8.2.2.2	Feature scale transport of plasma species	86
8.2.2.3	Surface kinetics and the importance of the oxygen sputtering yield	87
8.2.2.4	Chemical etching parameters calibration	92
8.2.2.5	Ion-assisted etching parameters calibration	93
8.2.3	Aspect ratio dependent etching and the effect on passivation composition	95
8.2.4	Nanoscale cryoetching simulation	100
8.3	Conclusion to the implemented cryogenic etch simulation model	101
9	Conclusions and outlook	105
	Appendix A Neumann boundary condition between two insulators	109
	Bibliography	126
	List of figures	128
	List of tables	129
	List of publications	131

Curriculum Vitae	133
Theses	135

Chapter 1

Introduction

Plasma dry etching of silicon is a crucial technology in the modern manufacturing of integrated circuits (ICs) and is in large part responsible for the continuous miniaturization of semiconductor devices, thus increasing their density on a chip. Due to the demands on further increasing of functionality, silicon-on-insulator (SOI) wafers are nowadays intensively used by the vast majority of electronic companies for fabrication of very large scale integrated (VLSI) circuits. To form VLSI circuits, multiple levels of lithography and plasma etching are required.

One critical step of the VLSI process is plasma etching of high aspect ratio (HAR) silicon features with SOI wafers. The process is well established for linewidths down to 100 nm; however, as feature sizes shrink, profile control is needed with tolerances approaching several nanometers. This technology has also been critical to the manufacturing of micro electromechanical systems (MEMS). Further miniaturization of MEMS and their transition to nano electromechanical systems (NEMS) requires unprecedented quality in profile control for small HAR structures.

Feature profile control in the high aspect ratio silicon dry etching is complicated by numerous critical parameters. *Inter alia*, to these effects belong surface charging [1], reactive ion etching (RIE) lag and pattern factor [2], bowing and faceting [3], microtrenching [4], as well as aspect ratio dependent etching (ARDE) [5], and others.

Because understanding of the complex physical and chemical phenomena is limited, the plasma etching technique remains highly empirical. Despite 20 years of intensive investigation of these phenomena, they are only partially understood. This is not surprising given the complexity of plasma etching which includes plasma processes to create reactive species, transport of these species through the plasma sheath to the sample and inside the etched microstructure, plasma–surface kinetics, etc. Consequently, in order to improve the process, significant experience and intuition are necessary to compensate the limited understanding of the various physical and chemical phenomena associated with the process [6]. Without this experience and significant experimentation – or alternatively, better understanding – device producers find difficulties in applying plasma process technology and face lower product yields [2].

Clearly, a fast way for experimenters to gain critical process insight while minimizing exper-

imentation would be a clear benefit. This can be realized with plasma etching profile simulation software. Simulation software can numerically model evolution of etching profiles revealing the dominant factors in the plasma etching process. This understanding can in turn be used to control the actual process with minimal experimentation, resulting in significant reduction of time and costs needed for the establishment and improvement of the process.

To this end, based on the previous works [7, 8], a new plasma processing simulation software named **ViPER** (**V**irtual **P**lasma **E**tch **R**eactor) was developed by the MNES workgroup at Ilmenau University of Technology [9–11] in the context of the European Union sponsored project *NanoPlasma*.

The **ViPER** simulator was designed in modules addressing plasma etch simulation at both, macro level (reactor scale) and micro level (feature scale). In common, the simulator consists of a plasma module (simulation of plasma chemistry in the reactor), transport module (implements transport of plasma species to the sample and inside the microstructure) and feature profile evolution module (simulates the profile geometry using etch rate values obtained by surface reaction modeling). The aforementioned common modules consist of sub-modules used for the modeling of various physical and chemical phenomena peculiar to the plasma etching process. This work focuses on development of surface charging effect and cryogenic silicon etching simulation modules, for application to HAR silicon etching. The physical and chemical models are developed, implemented in code, and then rigorously tested with real plasma etching experiments.

Surface charging of the insulating materials of the sample is particularly problematic with high aspect ratio features [2]. As a first objective, by using the model developed in this work, the influence of the surface charging (charging effect) was investigated to address problems in HAR on SOI due to the presence of the insulating oxide under the silicon layer being etched. For the first time, the charging effect was simulated over the entire course of the etching process accompanied by validation of the obtained results using comparison with real plasma etching experiments.

As a second objective, a new simulation model focusing on cryogenic SF_6/O_2 etching of silicon was developed. Low temperature silicon etching, first introduced by Tachi *et al.* in the late 1980s [12], allows advanced surface chemistry control during etching. Furthermore, this technique, recently investigated by Lawrence Berkeley National Laboratory for sub-10 nm etching shows great promise for HAR silicon etching at feature linewidths of several nanometers [13, 14]. The cryogenic etching simulation model, developed in this work, was successfully tested with real nanoscale plasma etching experiments conducted at Lawrence Berkeley National Laboratory, California, USA.

The common structure of the presented work is described as follows.

First part of the work provides a common introduction into the plasma processing technology with the focus on plasma etching of silicon. Short overview of plasma basics is followed by a description of typical plasma sources and configurations of plasma etching hardware. Emphasis is laid on the chemistries and the etch equipment configurations which are most commonly used for anisotropic silicon etching. After that, a description of the considered etching mechanisms is

followed by a discussion about the transport phenomena which occur while the plasma species travel from the plasma towards the sample and inside the microstructure.

Second part of the work makes a short overview of the **ViPER** simulator.

In the third part, the developed charging effect simulation model is presented, where the model algorithms are described together with the validation procedure.

Fourth part of the work describes the developed simulation model for SF_6/O_2 cryogenic silicon etching. Overview of the developed model is followed by description of the model calibration procedure, in which all necessary parameters of the model are estimated.

The work closes by making conclusions and giving outlook to further improvement of the developed models in terms of future challenges of plasma etching simulations.

Chapter 2

Plasma

The state of plasma is often considered a fourth state of matter and is very wide-spread in the universe. It was Irving Langmuir who assigned to it the term *plasma* in 1928. Plasma is 99% from a total amount of the whole existing matter. For example, stars, as well as most interstellar matter, are plasmas [15].

Due to definition, a plasma is a chaotic gaseous partly ionized system consisting of equal numbers of positive (ions) and negative (electrons, negatively charged ions) particles, and a different number of un-ionized neutral molecules[16, 17]. Plasmas maintain themselves by collisions of electric carriers with neutrals, whereas the inelastic collisions between rapidly moving electrons and slow heavy particles are the reason for almost all of the gaseous ionizations within a plasma [16]. Physics of plasma is maybe much more difficult to understand in comparison to electromagnetics in insulators or to fluid dynamics [18]. This is explained by the plasma nature. On the one hand, containing charged particles, a plasma is electrically conductive and can be influenced by external electromagnetic fields, forcing the particles to move in order to shield each other from this fields [19]. On the other hand, the particle-particle collisions inside plasma also contribute to the particle motion. The overlapping of this two plasma properties greatly complicates a deep understanding of plasma physics[18].

Containing equal concentrations of positive and negative charge carriers, the plasma is on average neutral from the outside. Simultaneously it is influenced by the external electromagnetic fields. Such state is often called *quasi-neutral* [19] and is one of the most important properties of plasma.

Let n_0 be the *plasma density* – a common charged particle density in particles/m³ within plasma, thus it is valid:

$$n_0 \approx n_i \approx n_e, \quad (2.1)$$

where n_i and n_e are appropriately the concentrations of the positive and negative charge carriers in the plasma.

The fractional ionization of the plasma is as follows:

$$\alpha_{iz} = \frac{n_i}{n_a + n_i}, \quad (2.2)$$

where n_a is the density of the neutral atoms.

The focus of this work are the plasmas used for material processing (etching/deposition) in the fabrication of semiconductor devices. These are high-density and low-pressure discharges, which are electrically driven and weakly ionized. Since the degree of ionization for typical processing conditions is in the range of 10^{-4} to 10^{-3} , the gas consists mostly of neutrals [17]. Typical values of the plasma density for the discharges are in the range of 10^9 cm^{-3} to 10^{12} cm^{-3} [17].

2.1 Debye length

The electron *Debye length* λ_D is the characteristic length scale in a plasma. The Debye length is the distance scale over which significant charge densities can spontaneously exist [15]. Being a key characteristic of a plasma, the Debye length will be discussed in this section.

Containing freely and randomly moving positive and negative charge carriers, the plasma is effectively screened against disturbing fields, whereas the groups of electrons are arranged around the ions, thus reducing the range of the Coloumb potential to very small values [16]. The effect was first described by Debye and Hückel in their theory of strong electrolytes in aqueous solutions [19]. According to the theory, clouds of the lighter ions will be formed around the more heavy ions. In case of a plasma, the lighter ions are represented by the electrons, while the positively charged ions stand for the heavier ones [7].

We assume that the majority of ions in the plasma are positively charged. Hence in further considerations, the negative ions will be always neglected. The ions are too massive to be instantaneously influenced by the space charge. Hence, the positive ions are considered here to be homogeneously distributed with the constant density n_i .

At varying positions in a plasma, the density of electrons in thermal equilibrium with respect to a spatially varying electric potential can be expressed by means of the *Boltzmann's relation* [15], which is one of the most important relations in plasma physics. Using the Boltzmann's relation for the electrons, the electron density around a certain ion is written as follows:

$$n_e(\vec{r}) = n_{e,0} \exp \left\{ \frac{e\varphi(\vec{r})}{kT_e} \right\}, \quad (2.3)$$

where $n_{e,0} = zn_i$ is the undisturbed electron density, e is the elementary charge, φ is the electric potential, k is Boltzmann's constant, T_e is the temperature of the electrons, and z is the ionization state of the ions.

For simplicity, it is also assumed that the positive charge carriers in the plasma are *singly* charged positive ions ($z = 1$), implying $n_{e,0} = n_i$. Considering the position of the ion to be \vec{r}_i , the

net charge density will look as follows:

$$\rho(\vec{r}) = e\delta(\vec{r} - \vec{r}_i) - \frac{e}{\varepsilon_0}(n_i - n(\vec{r})), \quad (2.4)$$

where $\delta(\vec{r} - \vec{r}_i)$ is the Dirac delta function.

After substitution of the electron density (Eq. 2.3) and the charge density (Eq. 2.4) into *Poisson's equation*, one obtains the differential equation for the electric potential $\varphi(\vec{r})$:

$$\Delta\varphi(\vec{r}) = -\frac{e\delta(\vec{r} - \vec{r}_i)}{\varepsilon_0} - \frac{en_{e,0}}{\varepsilon_0} \left(1 - \exp\left\{\frac{e\varphi(\vec{r})}{kT_e}\right\}\right). \quad (2.5)$$

Now, assuming the electric energy is much smaller than the thermal energy, namely $e\varphi(\vec{r}) \ll kT_e$, Eq. 2.5 can be linearized by means of expanding into a Taylor series and truncating after the linear term [15]. After [20], the radially symmetric solution is as follows:

$$\varphi(\vec{r}) = \varphi_0 \exp\left\{-\frac{r}{\lambda_D}\right\}, \quad (2.6)$$

where $r = |\vec{r} - \vec{r}_i|$ is the distance from the considered ion and φ_0 is the unshielded potential of a singly charged positive ion, given by

$$\varphi_0 = \frac{e}{4\pi\varepsilon_0 r}. \quad (2.7)$$

In Eq. 2.6, λ_D is the Debye length, which is described by the expression:

$$\lambda_D = \sqrt{\frac{\varepsilon_0 kT_e}{e^2 n_{e,0}}}. \quad (2.8)$$

The Debye length shows how rapidly the perturbation of the electric potential decays in the plasma. Due to the Irving Langmuir's definition of plasma, λ_D has to be small with regard to the spatial dimensions of plasma. Then, the unperturbed plasma will be equipotential except for small fluctuating voltages which are attenuated over distances of the order of the Debye length [17]. Evidently, the ionized gases with very small n_e and thus having very large values of the Debye length, that are in the order of the dimensions of the reactor, cannot be termed quasi-neutral any more [16].

Concluding, we note that the Debye length is a key parameter allowing to clearly distinguish between ionized gases and plasmas.

2.2 Temperature of plasma particles

Because of such phenomena like recombination, diffusion and particle reaction with reactor walls, the concentration of the charge carriers in a plasma constantly reduces. In order to keep the plasma density unchanged, an external energy source should be used, for instance, external electric fields.

In such a case, this extra energy, coupled into the plasma, is represented as the work W , done to a singly charged particle by the electric field \vec{E} , namely: $W = eEx$, where $x = \frac{1}{2}at^2$ [19]. Considering m be the particle mass, the acceleration becomes $a = \frac{eE}{m}$, resulting in the following expression for the work:

$$W = \frac{(eEt)^2}{2m}. \quad (2.9)$$

Since the mass of an electron is at the least 1836 times less than the mass of an ion, the most part of the energy is transferred to the plasma electrons. Let m_e be the mass of an electron and m_i is that of a considered generic positive singly charged ion. If we consider a Maxwell-Boltzmann distribution for the electrons, their mean speed will be: $\langle v_e \rangle = \sqrt{\frac{8k_B T_e}{\pi m_e}}$. Then the electron current density ($j = \rho v/4$), is about a factor 10^3 higher, than the current density of the Ar-ions.

This means, that the plasma is not in thermal equilibrium, that is, the ions, electrons and neutrals have different temperatures. For the low-pressure material processing plasmas, the electron temperature can be more than 20000 K. On the other hand, the temperature of ions and neutrals is close to the ambient temperature (500 K (0.004 eV) for ions and 300 K (0.02 eV) for neutrals) [16, 17, 19]. A low-pressure plasma is also considered as a *cold plasma*, where the plasma density values are in the range of 10^9 to 10^{12} cm⁻³.

2.3 Plasma oscillations

If we consider the all electrons in the plasma are removed from their equilibrium position by x , a large restoring force $F = -eE$ (E is the electric field) will act on them striving to keep the charge neutrality, yielding the expression [7]:

$$m_e \frac{d^2x}{dt^2} = -eE = -\frac{e^2 n_e}{\epsilon_0} x. \quad (2.10)$$

This is the equation of the so called *Langmuir oscillations* [7] with the frequency

$$\omega_e = \sqrt{\frac{n_e e^2}{m_e \epsilon_0}}, \quad (2.11)$$

being also called the *plasma frequency*.

The importance of this parameter is revealed while calculating the time τ , needed to balance out the deviations from equilibrium in the plasma. Provided the electrons in the plasma are distributed due to a Maxwell-Boltzmann distribution, their speed is expressed as follows:

$$f(v) = \frac{4}{\sqrt{\pi}} \frac{v^2}{v_{pr}^3} \exp \left\{ - \left(\frac{v}{v_{pr}} \right)^2 \right\}, \quad (2.12)$$

where v_{pr} is the most probable speed:

$$v_{\text{pr}} = \sqrt{\frac{2kT_e}{m_e}}. \quad (2.13)$$

The mean speed $\langle v \rangle$ is given by

$$\langle v \rangle = \int_0^{\infty} v f(v) dv = \sqrt{\frac{8kT_e}{\pi m_e}}. \quad (2.14)$$

The mean kinetic energy of the electrons will be

$$E_{\text{kin},e} = \frac{1}{2} m_e v_{\text{rms}}^2 = \frac{3}{2} kT_e, \quad (2.15)$$

where v_{rms} is the root mean square speed, expressed by

$$v_{\text{rms}} = \sqrt{\int_0^{\infty} v^2 f(v) dv} = \sqrt{\langle v^2 \rangle} = \sqrt{\frac{3kT_e}{m_e}}. \quad (2.16)$$

The considered time τ can be now expressed as follows [7]:

$$\tau = \frac{\lambda_D}{v_{\text{rms}}} = \frac{1}{\sqrt{3}} \sqrt{\frac{\epsilon_0 m_e}{n_e e^2}} \approx 0.6 \frac{1}{\omega_e}. \quad (2.17)$$

Due to Eq. 2.17, the time needed to balance out the perturbations in the plasma stands in direct proportion to the Debye length and is inversely proportional to the v_{rms} , which reflects the thermal energy of the electrons. Hence, increasing of the electron temperature will force the perturbations in the plasma to relax more rapidly.

Two scenarios are possible in case the plasma perturbations are caused by external fields. Until the plasma frequency is higher than that of the external fields, the perturbations are compensated very rapidly by the displacement of electrons. Once the frequency of the external fields becomes higher than the plasma frequency, the plasma will not be able to follow the instantaneous external fields anymore. It will follow the resulting time-averaged fields.

The Debye length λ_D and the plasma frequency ω_e are the spatial and temporal limits for the extension of plasma perturbations [7].

Considering the ion mass m_i and the ion density n_i and following the same considerations as that for the electrons, one can derive a plasma frequency ω_i for the ions:

$$\omega_i = \sqrt{\frac{n_i e^2}{m_i \epsilon_0}}. \quad (2.18)$$

2.4 Potential distribution in plasma and plasma sheath

As follows from Eq. 2.9, the mean electron velocity in the plasma is several orders of magnitude higher than the mean ion velocity. Therefore, a considerably larger number of electrons is captured by the reactor walls due to recombination, thereby leaving behind a positive net charge. In other words, the plasma obtains a positive electric potential φ_p , also called *plasma potential*, with respect to the reactor walls. The potential difference is built up across a small distance of only several Debye lengths [16]. The layer, where the described potential drop occurs, is called *sheath*. One of important properties of the sheath is a formation of potential barrier, which prevents the electrons from leaving the plasma [19]. The positive ions, on the contrary, have a potential downhill in the direction out of the plasma.

2.4.1 Floating potential

The potential, which is set up at all isolating walls contacting with plasma, is called a *floating potential* φ_f . The sheath can also form around each electrically isolated electrode, that is immersed into the plasma. In such a case, the electrons, having much higher velocities than that of the ions, reach very quickly the electrode and start to charge it up negatively. The negative potential build up continues, until it becomes strong enough, to repel other electrons, further coming from the plasma. Then some amount of positive ions from the plasma is attracted. And so on, until the steady-state potential at the electrode surface is reached, that is, the electron and ion fluxes are equal in each point of the surface. As a result, the plasma acquires a positive potential φ_p with respect to all the walls or electrodes, which are in contact with it.

In order to determine the floating potential φ_f , the electrons are again considered a subject to the Maxwell-Boltzmann distribution of speed, whereas $\langle v_e \rangle$ stands for the mean speed of the electrons and $\langle v_i \rangle$ is that for the positive ions. Quasi-neutrality $n_0 = n_e = n_i$ holds for the plasma bulk. Since the electrons entering the sheath should climb the potential barrier in the direction of the floating electrode, we use a Boltzmann retarding factor from Eq. 2.3 in order to express the reduction of the mean electron current due to the floating potential φ_f . The resulting electron current in the sheath is given by

$$j_e = -e \frac{\langle v_e \rangle}{4} n_e \exp \left\{ -\frac{e\varphi_f}{kT_e} \right\}. \quad (2.19)$$

The positive ions do not have to overcome any potential barrier. Then, the mean ion current is

$$j_i = +e \frac{\langle v_i \rangle}{4} n_i. \quad (2.20)$$

Using $n_e = n_i$ and the steady state condition, $j_i + j_e = 0$ [7], we get:

$$\varphi_f = -\frac{kT_e}{e} \ln \frac{\langle v_i \rangle}{\langle v_e \rangle}. \quad (2.21)$$

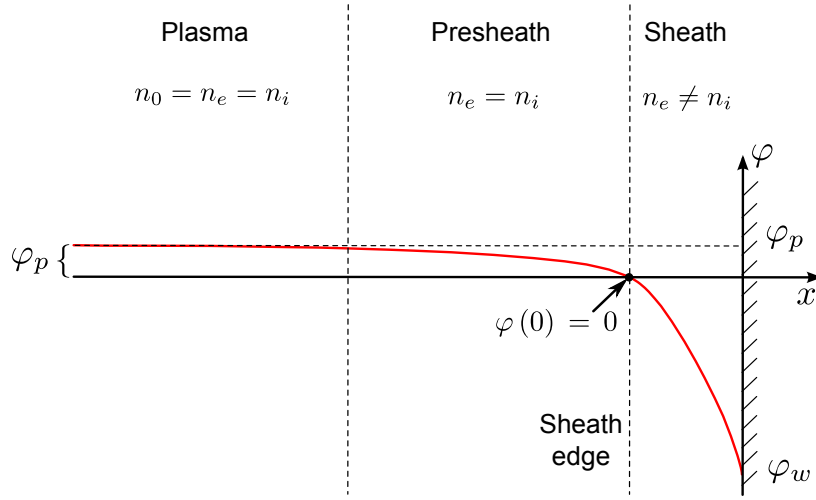


Figure 2.1: *Qualitative behaviour of sheath and presheath in contact with a plasma reactor wall. Red solid curve represents behaviour of the electric potential in the region between the plasma and reactor wall. φ_p – plasma potential, φ_w – potential at the reactor wall. After Lieberman and Lichtenberg [15].*

Using Eq. 2.14 [17] for substitution of $\langle v_e \rangle$ and $\langle v_i \rangle$, the floating potential is expressed as follows:

$$\varphi_f = -\frac{kT_e}{2e} \ln \frac{m_e T_i}{m_i T_e} = \frac{kT_e}{2e} \ln \frac{m_i T_e}{m_e T_i}. \quad (2.22)$$

However, the described approach does not take into account the acceleration of the ions towards the negative probe. This issue is addressed in the next section **2.4.2: Presheath and the Bohm criterion**.

2.4.2 Presheath and the Bohm criterion

Due to the quasi-neutrality of the plasma, the concentrations of the positive and negative charge carriers in the plasma bulk are equal ($n_e = n_i$). However, this is not true for the plasma sheath, where the charge neutrality breaks down ($n_e \neq n_i$). In fact, there is a quasi-neutral transient region of low electric field between the plasma and the sheath (see Fig. 2.1). In this region, which is called the *presheath*, the velocity of ions is increased before they enter the sheath. The phenomena was first demonstrated by Bohm (1949) and is known as the *Bohm sheath criterion* [15, 17].

Being an important parameter for the formation of the floating potential, the velocity of the ions entering the sheath will be shortly discussed here. For the derivation, the electric potential in the positive space charge sheath ($\frac{d^2\varphi}{dx^2} < 0$) is assumed to decrease monotonically as the ions move towards the probe. The point $x = 0$ (see Fig. 2.1) is selected to be on the presheath-sheath interface, such that $n_i(0) = n_e(0)$ and $\varphi(0) = 0V$. The sheath is considered to be collisionless (conservation of charge – no ionization or recombination of ions), implying the ion current $j_i(x) = j_i(0) = en_i(x) \frac{\langle v_i(x) \rangle}{4}$ is constant over the entire sheath region.

Taking conservation of energy of the ions into account, we obtain:

$$\frac{m_i v_{i,\text{rms}}^2(x)}{2} = \frac{m_i v_{i,\text{rms}}^2(0)}{2} - e\varphi_f. \quad (2.23)$$

The assumed conservation of charge yields for the ion density in the sheath:

$$n_i(x) = \frac{n_i(0) \langle v_i \rangle}{\langle v_i(x) \rangle}. \quad (2.24)$$

Using Eqs. 2.14 and 2.16 [17] together with substitution of Eq. 2.23 into Eq. 2.24 results in

$$n_i(x) = n_i(0) \sqrt{\frac{8}{3\pi}} \left(1 - \frac{2e\varphi_f(x)}{m_i v_{i,\text{rms}}^2} \right)^{-\frac{1}{2}}. \quad (2.25)$$

Using $\sqrt{\frac{8}{3\pi}} \approx 1$ and substituting the obtained ion density $n_i(x)$ and the electron density $n_e(x)$ (given by the Boltzmann relation) into Poisson's equation

$$\frac{d^2\varphi}{dx^2} = \frac{e}{\varepsilon_0} (n_e(x) - n_i(x)), \quad (2.26)$$

and recalling the quasi-neutrality ($n_e(0) = n_i(0)$) at the presheath-sheath interface, one obtains the following expression:

$$\frac{d^2\varphi}{dx^2} = \frac{en_e(0)}{\varepsilon_0} \left[\exp \left\{ \frac{e\varphi_f}{kT_e} \right\} - \left(1 - \frac{2e\varphi(x)}{m_i v_{i,\text{rms}}^2} \right)^{-\frac{1}{2}} \right], \quad (2.27)$$

which is the basic nonlinear equation governing the sheath potential and ion and electron densities [15].

Using the positive space charge sheath condition ($\frac{d^2\varphi}{dx^2} < 0$ for all $x > 0$) results in the inequality:

$$\left(1 - \frac{2e\varphi(x)}{m_i v_{i,\text{rms}}^2} \right)^{-\frac{1}{2}} > \exp \left\{ \frac{e\varphi_f}{kT_e} \right\}. \quad (2.28)$$

Now, we restrict our attention only to the beginning of the space charge sheath, where $e\varphi_f(x) \ll kT_e$. Using this condition, after squaring and inverting the expression in Eq. 2.28, one can expand and approximate the exponential, which yields:

$$1 - \frac{e\varphi_f}{kT_e} > 1 - \frac{2e\varphi(x)}{m_i v_{i,\text{rms}}^2}, \quad (2.29)$$

resulting in the *Bohm sheath criterion*:

$$v_{i,\text{rms}}(0) \geq v_B = \sqrt{\frac{kT_e}{m_i}}, \quad (2.30)$$

where v_B is the Bohm velocity – the minimal velocity of the ions entering the sheath.

The Bohm criterion can be also expressed in terms of the kinetic energy of the ions [7]:

$$\frac{m_i v_{i,\text{rms}}(0)}{2} > \frac{kT_e}{2}, \quad (2.31)$$

implying that the ions are accelerated in the presheath due to a low voltage $V = \frac{kT_e}{2e}$ leaking into the plasma. Then, the electron density on the presheath-sheath interface is as follows:

$$n_e(0) = n_e \exp\left\{\frac{-eV}{kT_e}\right\} = n_e \exp\left\{-\frac{1}{2}\right\} \approx 0.6n_e. \quad (2.32)$$

Recalling again the quasi-neutrality ($n_e = n_i$) between the sheath and presheath, one obtains for the ion current:

$$j_i \geq 0.6en_e \sqrt{\frac{kT_e}{m_i}}. \quad (2.33)$$

Due to the condition for equilibrium, $j_i + j_e = 0$. Using the electron current from Eq. 2.19, the floating potential is expressed as follows:

$$\varphi_f \leq \frac{kT_e}{2e} \ln \frac{m_i}{2.3m_e}, \quad (2.34)$$

which is equality for zero ion temperature [7].

Chapter 3

Plasma generation for material processing

Chemically reactive plasma discharges are widely utilized to modify the surface properties of materials [15]. Nowadays, it is impossible to imagine several of the largest manufacturing industries of the world without a plasma processing technology. In particular, this material processing technique plays a crucial role in the fabrication of modern (nanometer scale) semiconductor devices as well as for manufacturing the very large scale integrated circuits. Some technological steps (etching, deposition, doping) are repeated many times during the IC manufacturing. Since one third of the tens to hundreds fabrication steps in the IC manufacturing are plasma based [15], the plasma processing technology is unavoidable for the entire electronics industry.

Typical plasmas which are used to this end are low pressure discharges, being generated in vacuum within a plasma processing reactor. In common, the plasma sources for such technological operations like etching or deposition consist of a vacuum reactor chamber with grounded sidewalls, whereas the process gases are introduced into the chamber through a special inlet. Not only the plasma chemistry arising in the reactor, but also the kinetic energy of the ions bombarding the target surface plays a crucial role in the mentioned type of processing. For example, the threshold energy for ion-enhanced etching of silicon with Ar^+ ions is 40 eV [21]. Therefore in the reactor, the substrate to be processed is placed on the cathode, which has a negative floating potential with respect to the plasma, forcing acceleration of the positively charged ions towards the probe. Since in many cases, the floating potential at the cathode is not enough to provide sufficient ion energies for sputtering processes, the cathode is driven by a *rf* power source via a blocking capacitor, which suppresses the DC current. Hence, during each positive half cycle the electrons reach the sample and discharge it, allowing much larger potential drop between the plasma and the probe.

Due to the various physical phenomena inside the reactor (recombination, diffusion out of the plasma bulk, or adsorption and/or neutralization at the reactor sidewalls), the number of the charge carriers in a plasma decreases with time. In order to compensate the loss of the charge carriers and sustain the plasma, an additional energy should be constantly coupled into the discharge. This additional energy supply results in increasing the ion and electron temperatures and gives rise to

ionization processes within the plasma bulk. Depending on how the energy is coupled into the plasma, there are three main types of plasma sources used for the plasma processing [22]:

- capacitively coupled plasma (CCP)
- inductively coupled plasma (ICP)
- downstream-plasma (DSP)

The mentioned types of the plasma reactors have different capabilities, thus each of them has its own scope of applications. Therefore in the next two sections, we will shortly discuss two of the most commonly utilized plasma reactor types in the ICs manufacturing, revealing their merits and drawbacks.

3.1 Capacitively coupled plasma (CCP) sources

In CCP, the energy is transferred by means of a capacitive coupling. An idealized discharge in plane parallel geometry, consists of a vacuum chamber containing two planar electrodes. One electrode is driven by an *rf* power source. The second electrode are usually the grounded reactor chamber walls. Feedstock gases are admitted to flow through the discharge and effluent gases are removed by the vacuum pump [15]. Typical driving voltages of the *rf* power source are 100-1000 V, and the plate separation usually varies from 2 to 10 cm.

Reactive ion etchers (RIEs) – is a common name for CCP reactors which are operated at low pressures with the wafer placed on the powered electrode and used to remove the substrate material. Such etching systems are commonly of asymmetric type, namely the area of the electrically powered cathode is much less than that of the grounded chamber walls. This results in more negative floating potential at the cathode with respect to the reactor walls. The potential difference between the two electrodes is called *dc self-bias*, or shorter *dc bias*. Since the chamber walls potential is close to that of the plasma, one can use the self bias for approximate estimation of the potential difference between the plasma and the sample [7]. A schematic plot of the potential distribution in a capacitively coupled plasma discharge is shown in Fig. 3.1. Typical driving frequency for the CCP discharges is 13.56 MHz and typical plasma densities are relatively low, 10^9 – 10^{11} cm⁻³. The electron temperature is of order 3 eV [15]. For anisotropic etching, the pressure values are in the range of 10-100 mTorr¹, whereas the ion acceleration voltages are high, greater than 200 V.

Due to their mobility, the electrons respond to the instantaneous electric fields induced by the *rf* driving voltage. Thus, they oscillate back and forth between the plasma and the both electrodes. Unlike the electrons, the massive ions respond only to the time-averaged electric fields, forming net positive charge regions near each electrode when averaged over an oscillation period. The electrode is constantly bombarded by the positive ions. The electrons, on the contrary, can reach the cathode

¹The SI-unit for the pressure is Pascal (Pa). However in the microsystem technology, the pressure in plasma processes is often given in Millitorr (mTorr). 1 mTorr \approx 0.133 Pa

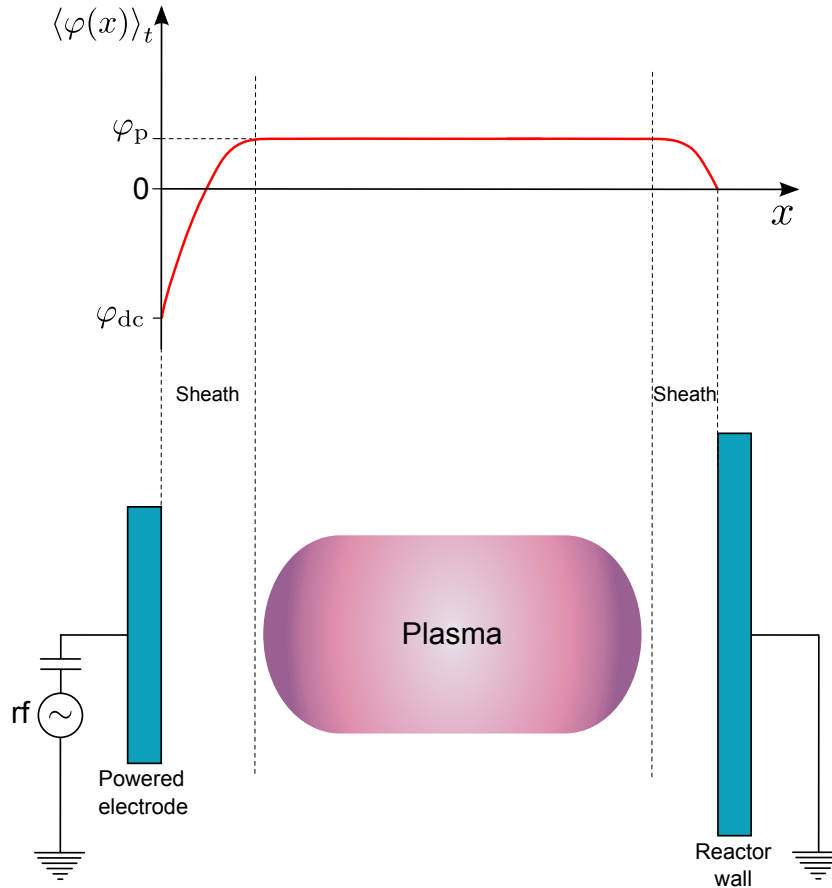


Figure 3.1: Approximate time-averaged potential versus distance plot for a capacitively coupled planar rf glow discharge system with wall area much greater than cathode electrode area (asymmetric system). The highest potential is that of the plasma. The cathode, connected with the rf generator via a blocking capacitor, has the lowest electric potential value. The right electrode represents the grounded reactor chamber walls. The time averaged potential between the plasma and the cathode causes acceleration of the ions towards the substrate. After John W. Coburn [23].

only when the oscillating cloud closely approaches the electrode. At that moment of time, the instantaneous sheath potential vanishes almost to zero, allowing sufficient electrons to leave the plasma and reach the cathode, thereby balancing the ion charge brought to the electrode (see also the time dependent potential at the cathode and in the plasma shown in Fig. 3.2). Positive net charge region in the plasma sheath results in a strong time-averaged electric field directed from the plasma to the cathode. The ions, once they have left the plasma and were accelerated in this sheath regions, can acquire high energy as they flow to the sample, leading to energetic-ion enhanced processes. Provided there are no particle collisions within the sheath, the dc bias value can serve as a good estimate in determination of this ion energies [7]. The ion energy distribution functions (IEDF) of SF₆ and Ar plasmas were measured respectively by Becker *et al.* [24] and Liu *et al.* [25].

In CCP discharges, if the power is increased in order to increase the plasma density, the self-bias will also increase, thus leading to increasing the ion energy. As a result, plasma density and ion energy are coupled and cannot be changed separately [22]. Hence, high ion energies, being often above 200 eV, is a severe issue for the profile and linewidth control at the sample

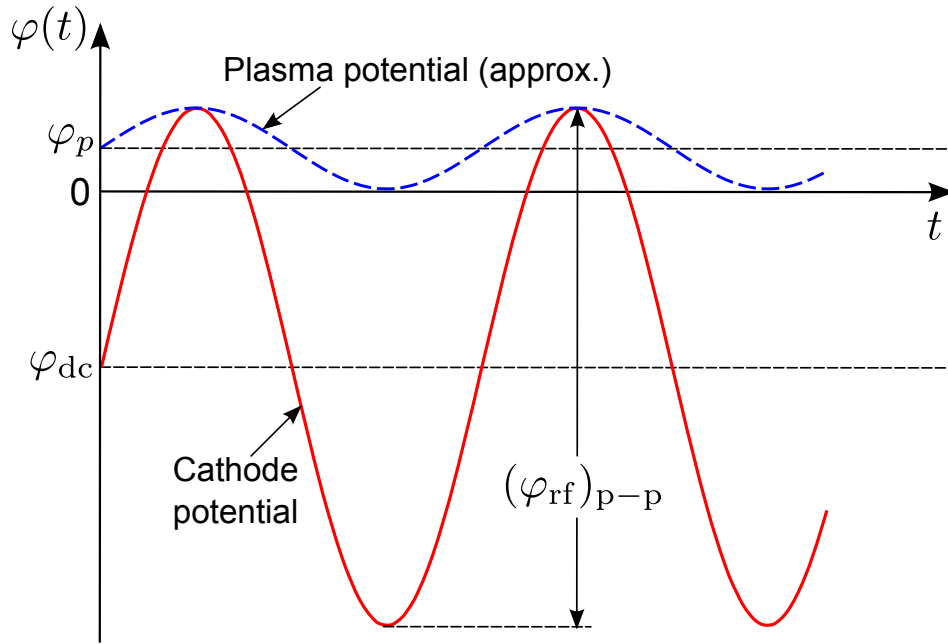


Figure 3.2: Approximate cathode and plasma potential waveforms for a capacitively coupled discharge. Plasma potential is represented by dashed blue curve with the average value of φ_p . Cathode potential waveform is presented by solid red curve, whereas φ_{dc} – self-bias voltage on cathode electrode. $(\varphi_{rf})_{p-p}$ – peak-to-peak rf voltage applied to cathode. After John W. Coburn [23].

microstructures when striving to obtain high aspect ratio features, in particular at the nanoscale. Another shortcoming of CCP discharges – low fractional ionization – results in low ion fluxes, which in combination with the high ion energy leads to a relatively narrow process window for many applications. Furthermore, the low fractional ionization can become a significant problem for processes, where the feedstock costs and disposal of effluents are issues [15]. Finally, it should be noted that utilization of very high frequency in reactors with large area electrodes (300 mm and larger) can result in plasma nonuniformities because of skin effects and standing waves [26].

3.2 Inductively coupled plasma (ICP) sources

In order to satisfy criteria of the damage, selectivity and linewidth control for the next-generation ICs fabrication in common, and for the nanoetching of silicon in particular, it should be possible to control the energy of the ion bombardment together with its energy distribution independently of the ion and neutral fluxes. The previously described drawbacks of CCP discharges forced development of a new generation of high-density, low pressure plasma sources. The need for large area, high-density plasma sources for plasma-aided manufacturing of integrated circuits has led to a renewed interest in inductively coupled plasmas (ICPs). Main merits of ICP sources are as follows [27]:

- high densities of ions, electrons and radicals
- excellent uniformity over diameters of at least 20 cm

- low and controllable ion energies
- negligible contamination from reactor sputtering or particulate generation

In an ICP, plasma is generated and sustained by application of *rf* power (typically 13.56 MHz) to a non-resonant inductive coil, which is usually located outside the reactor, around its chamber. As a result, a strong time-varying magnetic field appears inside the ICP reactor chamber, which in turn, by means of induction, gives rise to an electric field inside the chamber, that causes ionization of the process gases. Unlike in CCP discharges, the electric field lines in ICP reactors are closed, namely the created electric field is described by the Maxwell-Faraday equation:

$$\nabla \times \vec{E} = -\frac{\partial \vec{B}}{\partial t}. \quad (3.1)$$

The described non-capacitive power transfer is the key to achieving low voltages across all plasma sheaths: at the cathode as well as at the surfaces of the reactor walls. The dc plasma potential, and hence the ion acceleration energy, is then typically 20-40 V [15]. The electrode on which the substrate is placed (the cathode), is driven by a capacitively coupled rf source, thus enabling an independent control of the ion bombarding energy, whereas the ion/radical fluxes are controlled by means of the ICP source power.

Electron temperature in ICP plasmas was investigated by Fuller *et al.* [28] for an 18 mTorr Cl₂ – Ar discharge (the ICP power was in the range of 250...800 W). The measured average electron kinetic energy is reported to be in the range of 3...7 eV (corresponding to \approx 20000...50000 K of the ideal gas temperature). In contrast, the kinetic gas temperature of the plasma has comparatively lower values: it is in the range of 300 to \approx 1000 K for the larger Ar fractions and it is up to \approx 2500 K for the larger Cl fractions.

Being in the range of $10^{11} < n_0 < 10^{12} \text{ cm}^{-3}$, ICP density regime for efficient discharge operation is typically a factor of 10 higher than that of CCP [15]. Hence, ICP sources are of considerable interest for low-pressure processing.

Due to the all described characteristics, ICP etching systems are routinely employed in industry for fabrication of integrated circuits and microelectromechanical systems (MEMS) [29]. In the majority of cases, typical ICP processes have the pressure values in the range of 1...100 mTorr. Among the most common ICP-driven processes are the following:

- anisotropic dry silicon etching with high etching rates
- etching of III-V-semiconductors with a low damage to the crystal structure [30]
- etching of silicon dioxide SiO₂ with high etching rates
- gold and platinum sputter etching

Since the mid-1990s, the ICP-RIE configuration has come to dominate high aspect ratio etching of silicon [31]. Such systems are simple, relatively cheap, and provide good process stability

allowing straightforward process optimization. Following this considerations, the current existing implementation of the **ViPER** simulator also focuses on the ICP plasma processing equipment. Hence, other types of plasma generation sources are out of the scope of this work.

Chapter 4

Plasma etching of silicon

The plasma etching of silicon is governed by a combination of the ICP plasma equipment parameters which are in common as follows:

- ICP power
- rf power at the cathode
- frequency value of the rf power at the cathode
- pressure in the reactor chamber
- combination of processing gases
- input flow rate of each processing gas
- temperature of the sample
- duration of the experiment

In the context of plasma processing, each set of the plasma equipment parameters defines the plasma processing experiment in a unique way and is often called a *recipe*. In the presented work, this name will be used too.

Due to the definition of plasma given in Chapter 2: *Plasma*, the chemistry in the reactor chamber is usually dominated by atoms, molecular radicals and low-energetic positive ions. These discrete components of the plasma chemistry are usually called *plasma species*. In the chamber, the chemistry must be such that the reactive species generated in the plasma react with the surface being etched to form a *volatile* product [32], thus providing the *plasma etching process*. According to Coburn and Winters [33, 34], one cycle of the plasma etching reaction can be well-defined as a sequence of three steps: adsorption, reaction and desorption. This basic cycle occurs sequentially in plasma etching processing, when considering the surface at atomic scale [35].

At the beginning of the processing, the silicon sample is loaded into the reactor chamber of the ICP plasma equipment. After that, the plasma is ignited according to a given recipe and the

sample is exposed to the reactive glow discharge. Because of the negative potential at the cathode with respect to the plasma, the positive ions from the plasma are accelerated in the sheath region towards the probe, arriving there essentially at normal incidence. Hence, the sample is subjected to both energetic ions and reactive neutral species.

In contrast to the plasma-surface reactions providing the plasma etching, it exists also another principal type of the plasma-surface interaction, where some of the plasma species *do not form* a volatile product. On the contrary, they produce polymers which stick to the surface of the sample being processed. Provided these adsorbed products are not removed, with the lapse of time it will result in a film deposited on the sample material. This process is called a *plasma deposition process*. In terms of the plasma etching of silicon, the plasma deposition process is often used for formation of inhibitor films in order to provide profile control of the etched features [36]. The utilization of the inhibitor films in the silicon dry etching is a key to production of high aspect ratio structures.

Providing comparably rapid etch rates, F-based chemistries are most widely used in silicon etching, whereas carbon-containing chemistries are well-known to be a source of species for the inhibitor film formation. Among fluorine-containing gases, SF₆ is the most popular for HAR silicon etch [31]. Hence in this work, the considerations will be restricted to SF₆ gas for the etching of silicon, while C₄F₈ gas will be attributed to the plasma deposition. Additionally, SF₆/O₂ gas mixture will be considered for the cryogenic Si etching, where, in turn, oxygen atoms account for the protective film formation.

Considering plasma-surface reactions during the etching process, it is instructive to have a qualitative and quantitative statistics regarding the plasma species arriving at the sample. In addition to fluorine atoms and chemically reactive radicals generated in SF₆ plasma, also some of the ionized plasma species can reach the cathode. Due to the data obtained by Becker *et al.* for a SF₆ discharge [24], the ions able to reach the cathode are SF_x⁺ (where x = 1...5), F⁺, F₂⁺ and F⁻, where SF₅⁺ and F⁻ are the most abundant species. Rauf *et al.* investigated plasma species for inductively coupled SF₆ and C₄F₈ plasmas [37]. Regarding SF₆ plasma, they report that the primary ions produced directly from SF₆ molecule are SF₃⁺ and SF₅⁺ ions. The reported fluorine radicals' flux ($\approx 10^{19} \text{ cm}^{-2} \text{ s}^{-1}$) is of several orders of magnitude higher than that of the positive ions ($\approx 10^{15} \text{ cm}^{-2} \text{ s}^{-1}$).

In terms of the plasma etching process, there are three basic types of reactions occurring during plasma-surface interaction:

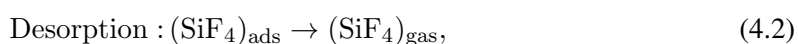
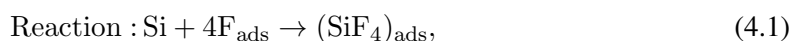
- Chemical etching
- Sputtering (physical etching)
- Ion-assisted etching

A deep understanding all of these etching mechanisms is critical not only for the further development of plasma etching hardware. It is also a key for adequate etching rate calculations in the

context of surface reaction modeling within a plasma processing simulation software. Therefore, the mentioned mechanisms will be separately discussed in the following sections.

4.1 Chemical etching

Fluorine atoms are known to spontaneously attack silicon and silicon compounds in the absence of ion bombardment [38]. Hence in the case of SF₆ plasma, the chemical etching is provided by the F-containing plasma species. Within the plasma, molecules of the introduced SF₆ processing gas are dissociated by electron impact collisions, thus generating F atoms. According to Flamm *et al.*[39], fluorine atoms form a stable chemisorbed layer on the surface of single crystal silicon. Provided such layer of adsorbed fluorine atoms already exists on the silicon surface, the etching of Si with fluorine due to Coburn and Winters[33] is expressed as follows:



where Eq. 4.1 expresses the formation of volatile products molecule and Eq. 4.2 represents the subsequent desorption of the products molecule into the gas phase.

According to Winters *et al.* [40], fluorine penetrates deeply into the silicon lattice during the etching reaction. They suggest that fluorine on the surface (top 10–20 Å) is probably SiF_x (x=1–3) and the fluorine in the silicon lattice exists primarily as negative F[−] ions. The ions adjust their concentration and depth distribution to fit the etch conditions, thus being able to influence the etching process.

There is still no agreed opinion between the researchers about the dominating etch product in the Si–F system. Donnelly *et al.*[41] and Flamm *et al.*[39] suggested SiF₂ as the primary etch product. However, later works of McFeely *et al.*[42] and Yarmoff *et al.*[43] indicate SiF₄ as the major reaction product in the Si–F system. Based on the results of these two works and some others, the most comprehensive conclusion to the issue seems to be that from Winters and Coburn in [44]. Due to their deep analysis of all previous works in this field, the primary etch product at room temperature is SiF₄(gas) together with minor quantities of Si₂F₆ and Si₃F₈, whereas it is suspected that the etch product distribution is controlled by the composition and structure of the outermost part of the SiF_x layer at the surface.

Investigation of reaction products for silicon etching in SF₆/O₂ plasma was conducted by D'Agostino and Flamm [45]. Due to their study of Si etch rate as a function of feed composition, the authors conclude that the etching species, namely fluorine atoms, compete with oxygen atoms for chemisorption on the Si surface. It is reported that SiF₄(gas) is the only stable silicon-containing etch product and SOF₂ is formed in oxygen-poor mixtures.

The reaction of silicon with fluorine atoms as a function of both pressure and temperature was a subject of the study conducted by Flamm *et al.*[39]. According to their data, the etching rate

is linear with gas phase F atom concentration up to about $1.6 \times 10^{22} \text{ cm}^{-2} \text{ s}^{-1}$. Most of other investigations confirmed the linear relation between the etch rate and fluorine flux in the low flux range (the pressure < 0.5 Torr) [44].

Regarding the temperature dependence, the fluorine atom data demonstrates an almost Arrhenius behaviour over the entire temperature range[39]. However, the interpretation of the etching rate in terms of the temperature variation should be done with a particular care: in Si-F system, the structure and thickness of the SiF_x layer are a function of temperature, thus influencing the etching rate[44].

Because of the chemical nature of the silicon spontaneous etching with fluorine, the etching occurs isotropically, that is the lateral and vertical etch rates are comparably equal. Such omnidirectional attack causes undercutting of a mask, producing profiles of a circular form (see Fig. 4.1).

Provided Φ_F stands for the fluorine flux (reactant) as average thermal flux. Then considering dependence on the flux Φ_F and on the temperature T , a simple model can be developed for the silicon etch rate [36] using the chemical etching component:

$$\text{ER}_{\text{chem}} = \eta_{(\text{F-Si})} \Phi_F, \quad (4.3)$$

where $\eta_{(\text{F-Si})}$ is the rate of thermal reaction [36], which is given by

$$\eta_{(\text{F-Si})} = k_0 \Phi_F \exp\left(-\frac{E_a}{k_B T}\right), \quad (4.4)$$

where k_0 is a constant and E_a is the activation energy (reported as 0.108 eV).

4.2 Sputtering

Sputtering or physical etching is the mechanism in which material is mechanically ejected from a surface by the energy and momentum transferred in energetic ion bombardment. In general, any material can be sputtered if the energy of ion bombardment is high and the pressure is low enough for ejected matter to be thrown across the reactor with few collisions [46].

The issue of sputtering was thoroughly addressed by Peter Sigmund [47]. His developed theory is a generally accepted description for the sputtering mechanism: impinging on the target surface, energetic ions cause collision cascade of target atoms, whereas some of them may obtain enough energy to leave the surface (see Fig. 4.1). Sputtering threshold energy E_{th} is the minimal energy of the impinging ion by which the sputtering process still can occur. Albeit sputtering enables anisotropic removal of the material providing high-quality pattern transfer, ion bombardment, in particular in plasma etching, may also result in compositional or structural damage to the processed surface [21].

The number of the removed target surface atoms per one impinging ion is called an *etching yield*. Etching yields for physical etching processes are strongly angle dependent [48, 49]. Hence,

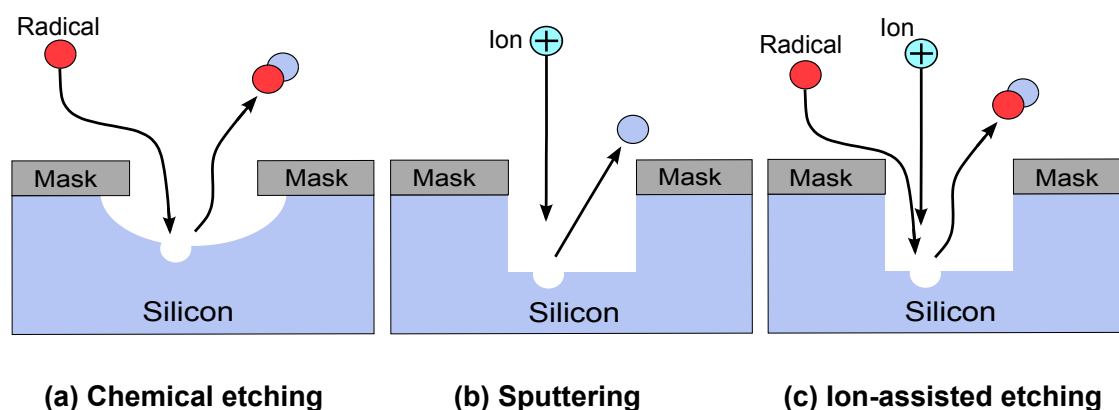


Figure 4.1: Three basic types of reaction mechanisms in terms of plasma etching of silicon. (a): spontaneous etching by chemically reactive radicals. (b): physical sputtering of atoms of the target material by energetic ions. (c): ion-assisted etching. Picture after Abe et al. [35].

sputtering process is often accompanied by a production of geometrical facets [46]. The dependence of the etch yield on the incidence angle of impinging ions was considered by Rangelow for different materials (Si, Au, Cr, PMMA and AZ1350 photoresists) in the context of profile simulations of ion milling processes [50]. These simulations demonstrated how the value of ion incidence angle, attributed to the maximum etch yields, influenced the final result for various shapes of initial profiles. The sputtering yield is also dependent on the energy of impinging ions. In the context of physical etching of silicon, a very important study on dependency of the etch yield on the incident ions' energy was conducted by Steinbrüchel [21]. Due to the reported data, the sputter yield Y_{sp} is proportional to the square root of the ion energy E :

$$Y_{sp}(E) \approx A \left(\sqrt{E} - \sqrt{E_{th}} \right), \quad (4.5)$$

where the constant A and the sputtering threshold energy E_{th} depend on the particular projectile-target combination.

In general, sputtering is a slow and unselective process, depending on the mean free path of the projectiles [46].

4.3 Ion-assisted etching

Unlike the surfaces subjected only to neutral species, the surfaces exposed to fluxes of both energetic ions and chemically active neutral species etch faster [51]. Using studies involving directed beams of species, Coburn and Winters confirmed and quantified this observation in their famous article [52], where they report about a 10-fold enhancement of the etch rate in comparison to that obtained without the influence of ions. This etching mechanism is often called *ion-assisted etching* (IAE) or *reactive ion etching* (RIE). Further in this work, the acronym *RIE* will be used.

One of the main attributes of the RIE mechanism is a large synergistic effect, in which the

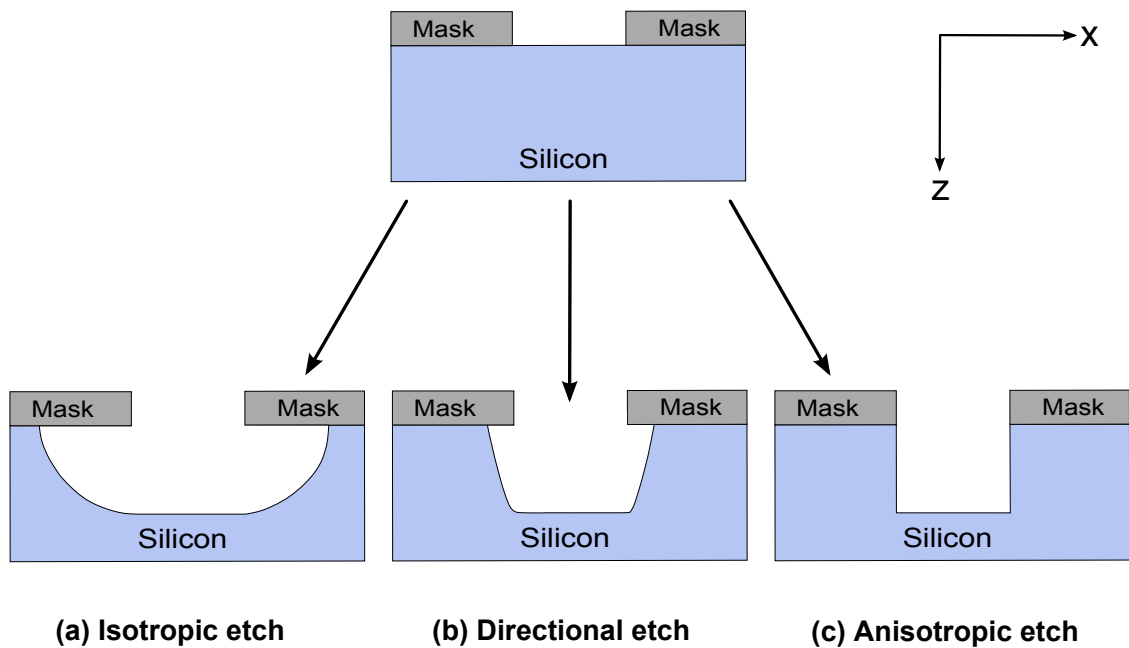


Figure 4.2: Directionality of etching processes. After John W. Coburn [51].

silicon etch rate observed with both energetic ion bombardment and active neutral species, simultaneously incident on the surface, greatly exceeds the sum of the etch rates obtained with each beam separately [32]. Hence, the etching probability of the incident reactive gas is greatly enhanced by the accompanying ion bombardment (see also Fig. 4.1(c)). In particular, this is true for Si etching in F-containing plasmas, where high etching rates can be usually achieved. The etching rate enhancement due to the ion bombardment is a great advantage of RIE. Despite numerous investigations, some details of the RIE etch mechanism are still not clear. However, the generic aspects can be formulated as follows. According to the work of Yarmoff and McFeely [43], the ion bombardment not only results in decreasing the fluorine concentration in the surface region but also changes the composition of the fluorinated target surface layer. The reduction of fluorine surface coverage results in turn in more exposure of the silicon surface to the attacks by F atoms. One of the crucial ion-assisted etching parameters is a relation between the ion flux and the flux of neutral species to the surface. The ion-enhancement factor is largest for small values of the neutral/ion flux ratio [44]. The utilization of RIE also results in much more etch products than that of the chemical etching. The etch products in the context of ion-assisted etching of silicon by SF_6 plasma was investigated by Oostra *et al.* [53, 54]. They report that clearly dissociation of SF_6 and breaking of Si-Si bonds by the ion bombardment leads to new chemical reaction products like SiF_x with $x \leq 4$, whereas sputtering of SiF_x species with $x < 4$ shows a collision cascade behaviour.

If during silicon etching, the etch rate of other materials of the sample is much smaller than that for the Si and can be neglected in terms of experiment, one speaks of a high etching *selectivity*. And *vice versa*, in the case of comparably similar etch rates for the materials, the selectivity will be low. One more very important advantage of RIE is a high silicon to mask selectivity for a large variety of organic and inorganic mask materials [3].

Provided a trench is etched in the silicon layer using a F-containing chemistry and a SiO₂ mask. At room temperature, F atoms will attack silicon even without any ion bombardment while SiO₂ will be etched much more slowly [51] without being exposed to energetic ions. Due to the spontaneous etching by fluorine atoms, the unmasked silicon will be etched isotropically, where lateral and vertical etch rates are relatively equal. This results in mask undercut (see Fig. 4.2(a)), which does not allow to create high aspect ratio features, especially for the small linewidths.

In terms of high aspect ratio deep silicon etching, the RIE is a critically important mechanism since it is able to provide *directional* etching. This effect is explained as follows. Being already accelerated in the plasma sheath, the positive ions are usually incident normally onto the sample surface. Thus in general, the sidewalls of the etched features are in shadow for the ions and are mainly subjected to the neutral species. In contrast, the bottom of the etched trench is exposed to both energetic ion bombardment and neutral radicals, thus much higher etch rate at the trench bottom is usually the case. Hence, the etch process becomes *directional*, in which vertical etch highly prevails in comparison to lateral etch (see Fig. 4.2(b)).

As a result of (HAR) deep silicon etching, it is very desirable to obtain pure vertical etch without a lateral component (see Fig. 4.2(c)). In this case, one speaks about *anisotropic etching*. For instance, anisotropic etch profiles in silicon can be achieved by RIE using HBr or Cl etch chemistries, where halogen atoms do not spontaneously attack silicon. However, the mentioned plasma chemistries can not provide etching rates comparable with those obtained by SF₆ plasma. On the contrary, the subject of this work – SF₆ plasma – allows much higher etching rates, but the certain mask undercut can become very problematic in the context of anisotropic silicon etching. Since RIE by SF₆ alone is not able to provide the desired profile control, some physical and chemical phenomena as well as auxiliary processing technologies are used to solve this issue, enabling highly anisotropic Si etching by SF₆ chemistry. These RIE techniques are critically important and will be shortly discussed in the following sections of this chapter.

4.4 The role of sidewall passivation

As already mentioned in previous section, utilization of SF₆ plasma chemistry for Si etching usually leads to a certain mask undercut, thereby not allowing to obtain purely anisotropic etch profiles. Thus, the employment of F-containing plasma requires special techniques (*Side-Wall Passivation* – SWP) in order to reduce the undercutting [55]. In terms of these techniques, the sidewalls of the trenches being etched should be protected against the chemically reactive neutral species, thereby diminishing the lateral etch rate. To this end, one uses *sidewall inhibitor films*. The creation of such films is based on the etching phenomenon in that some of the radicals ($-CF_2-$) generated in plasma can not react directly with the silicon substrate to produce volatile products; instead of that, they give rise to polymers covering the surface.

Such polymer films can be removed mainly by ion bombardment. As it was mentioned earlier, the ion flux close to the etched feature is strongly directional – thus the vast majority of ions bombards the trench bottom. In contrast, the vertical or steeply sloped sidewalls of the etched

features, are almost not exposed to the ion flux. Hence, the polymers will not be removed there and with the lapse of time, these surfaces will be covered with polymer-based films. These films are also known as *sidewall passivation layers* (SWPL). These layers slow down and can completely stop the lateral attack of the surrounding etchant species, thus reducing the undercutting of the mask [38].

The plasma deposition of polymer films on flat, unstructured samples was studied for many years [56]. Usually when plasma depositing polymer on structured samples, like long trenches, the film thickness decreases from top to bottom [57]. However, Volland *et al.* [58] report that under certain conditions during the polymer deposition in trenches of silicon samples, an initial sidewall texture is enhanced in the deposited polymer film. Furthermore, due to the data of this study, the polymer thickness is maximum at a certain depth at the sidewalls of the trench.

4.5 Gas chopping etching technique

The gas chopping etching technique (GChET) or the time-multiplexed alternating process for high aspect ratio silicon etching relies on alternating etching and polymerization steps. In 1986, this idea was introduced by Tsujimoto *et al.* [59] for tungsten or silicon etching in which SF_6 was the etching gas and NH_3 gas was used for the deposition. In 1991, the scallops at the sidewalls of the etched trenches, peculiar to the GChET, were first shown by Rangelow in which a gas chopping method was used for etching of polyimide nano dots utilizing oxygen as etching gas and a mixture of CHF_3 and CH_4 as deposition gases [60, 61]. The gas chopping etching technique was later applied for etching of silicon, where SF_6 was used as etching gas and CHF_3 as deposition gas [62].

The gas chopping method allows to obtain much higher aspect ratios of the etched features with a very high selectivity. For instance, Mukherjee *et al.* [63] used the gas chopping technique to create 100 nm half-pitch gratings in silicon with depths up to $6\ \mu\text{m}$ (aspect ratio 60:1). The technique is as follows. Each polymerization step is followed by an etch step in that the polymer film at the trench bottom is removed due to the ion bombardment, thus exposing the buried silicon surface and allowing the ion-assisted vertical etching at the trench bottom to occur. On the contrary, the passivation film at the trench sidewalls is not removed, hence further preventing lateral etch.

For GChET, SF_6 plasma is most commonly used for the etch step, whereas the sidewall passivation and mask protection is provided by octafluorocyclobutane C_4F_8 , a cyclic fluorocarbon that breaks open to produce CF_2 and longer chain radicals which readily deposit as fluorocarbon polymers on the processed surfaces during the passivation step [64]. The alternating etch and passivation steps give rise to a surface roughness of the sidewalls of the etched features, which is represented by so called *scallops* or *ripples*. Each scallop on the both sides of the etched trench is a result of one etch/deposition cycle.

In terms of the gas chopping technique, the balance of etch and passivation is very critical for deep anisotropic etch as well as for the process stability. Hence, the F/C ratio in the plasma reactor and inside the sample microstructure should be considered with a particular care.

A lot of works have been done towards the optimization of the gas chopping technique. For instance, Volland *et al.* have developed a novel gas chopping etching technique process in order to achieve a smooth sidewall surface without the scallops [62], however at the expense of some decreasing the selectivity. Another kind of optimization to the time multiplexed etching method was made by Blauw *et al.* In [65], they balanced the interactions during etching and passivation pulses for maximal profile control in terms of the gas chopping deep silicon dry etch process with $\text{SF}_6 - \text{C}_4\text{F}_8$. In their further work [66], Blauw *et al.* have introduced an advanced, time-multiplexed plasma etch process, which in comparison to the two pulse gas chopping process consisted of a sequence of three pulses. The conducted improvements to the process lead to better mask selectivity and substantial range for profile control from fully anisotropic to strongly negatively tapered.

Albeit the considered time-multiplexed etching technique is capable of producing anisotropic HAR features in silicon with acceptable levels of selectivity, its shortcomings are very problematic when striving to obtain high aspect ratio structures with widths of several nanometers. First, the already mentioned surface roughness (scallop) of the etched features sidewalls is a severe issue at the nanoscale. The second drawback of GChET is that it is not a clean process, namely during the processing procedure, there are a lot of contaminants in the reactor chamber significantly modifying the plasma parameters, which greatly complicates profile control, in particular for nanoscale etching. Moreover, frequent cleanings of the reactor are required for reproducibility of the process.

4.6 Cryogenic etching of silicon

The concept of cryogenic plasma etching of silicon was introduced by Tachi *et al.* in 1988 [12]. This technique is an alternative to the gas chopping method. During the cryoetch process the sample is kept at low temperature. Fluorine-based high-density plasmas are often used as the process chemistry. This work focuses on SF_6 / O_2 plasma chemistry in the context of deep silicon cryoetching. The sticking probability of F atoms and their compounds with silicon is directly influenced by the substrate temperature. Thus when keeping the substrate at low temperature, fluorine is much less penetrating into silicon lattice than at room temperature [3]. Thereby, the spontaneous reactions which form volatile products are reduced, but still can not be completely eliminated when using pure SF_6 plasma chemistry, resulting in a certain mask undercut. Addition of oxygen to F-containing plasmas for patterning of Si is useful to control lateral etch rates by sidewall passivation [67, 68]. Hence, the utilization of SF_6 / O_2 discharges is able to provide etch directionality. With increasing of O_2 fraction in the processing gas mixture, oxidation competes with halogenation and as a result, the silicon surfaces get oxidized to some extent – being covered with SiF_xO_y film. Thus, the fraction of oxygen in this siliconoxifluoride material is directly dependent on SF_6 / O_2 ratio in the processing discharge. The etching of SiF_xO_y passivation layer strongly depends on the incident flux of energetic ions, that is, at the bottom of the etched trench, the reaction of F atoms with the SiF_xO_y layer is enhanced by incident energetic ions. As a result, only a very thin ($\approx 1 - 2$ nm) SiF_xO_y layer exists on that ion-bombarded surface during steady-state etching [68]. In contrast, the SiF_xO_y film prevents silicon etching at the trench sidewalls, which are almost not subjected to

ion bombardment. Hence, as SF₆ is diluted with O₂, the mask undercut decreases and the etching process becomes more directional. In SF₆ / O₂ systems, the F/O ratio in the discharge is the main factor influencing the spontaneous etch rate and the amount of mask undercut.

The formation of the SiF_xO_y passivation layer in silicon cryoetching processes was thoroughly investigated in several works [69–71]. Due to the study conducted by Mellhaoui *et al.* [69], the formation of the SiF_xO_y strongly depends on the O₂ content, temperature and DC bias. It was also shown, that the passivation layer spontaneously desorbs when the silicon wafer temperature increases and mostly disappears when the wafer is warmed up to ambient temperature. Pereira *et al.* [70] investigated the desorption of a SiF_xO_y layer obtained in an overpassivating SF₆/O₂ regime during the wafer warm-up from the cryogenic temperature to room temperature. According to the data obtained by an *in situ* x-ray photoelectron spectroscopy (XPS), the authors proposed a mechanism for the formation of the SiF_xO_y passivation layer at cryogenic temperature and its desorption. Namely, the layer forms according to fluorine and oxygen incorporation within the silicon lattice, which results in the formation of nonvolatile SiF_xO_y structures. After the sample starts to warm up, SiF₄ volatile compounds are formed due to the diffusion of fluorine and oxygen. The formed SiF₄ compounds correlate with the desorption of the SiF_xO_y passivation layer. Also, Tillocher *et al.* [72] report about an oxidation threshold during the SiF_xO_y film growth. Beyond this threshold (which is reflected by either in temperature, oxygen concentration or ion bombardment power), silicon is no longer efficiently etched which results in decreasing the SiF₄ production, while the concentration of F radicals and F₂ on the contrary grows. According to the conducted study, the oxidation threshold occurs for lower O fraction in the discharge when the wafer is kept at low temperature.

With the combination of low temperature and low bias powers, remarkable selectivity can be achieved even at the nanoscale[14]. For instance, selectivity of 10:1 was reported for 40 nm dense lines with an electron beam resist mask, ZEP, with 40 nm features, very high for such feature sizes[13].

High selectivity is particularly important with nanoscale features, for instance, those derived from block copolymer lithography. Block copolymer lithography is being investigated as a means to pattern at resolutions beyond what electron beam or optical lithographies can achieve. With block copolymer lithography, the mask thickness is generally only less than ~ 1.5 times the periodicity of the features. Using the cryogenic silicon etching technique with a polystyrene mask derived from block copolymer lithography, selectivity of 10:1 was achieved at 50 nm pitch[73].

Nowadays, the silicon cryoetching process is not widely used. This is due to the practical difficulty of maintaining the cryogenic temperature of the processed wafer. Not only the reactor hardware is complex. Also the time, which is needed to cool the wafer down from ambient temperature for the processing and to warm it up back to ambient temperature after the processing, results in a very slow process with low manufacturability [31]. Despite the cryogenic etching process is not in widespread use in manufacturing[31], given these recent advantages shown for nanoscale silicon etching with soft mask[73] and other benefits in low-k dielectric etching[22] this may change. It is particularly well suited for nanoimprint template fabrication where any loss in throughput due

to cooling requirements can be compensated for by the throughput gains made by replicating the template many times over.

In comparison to the gas chopping technique, reactive ion etching of Si at cryogenic substrate temperatures has decisive advantages in context of deep anisotropic etching at the nanoscale. Since the SiF_xO_y passivation layer desorbs and mostly disappears during the wafer warms up to room temperature, the silicon cryoetching process is a more clean process, characterized by much less residual contamination from plasma passivants. Providing high selectivity, the cryogenic etching of Si, in contrast to the gas chopping method, do not produce surface scallops at the sidewalls of etched features. This results in a low sidewall surface roughness – a critical advantage when etching nanostructures. Finally, the cryogenic process using SF_6/O_2 gas mixture allows etching and passivation to occur simultaneously. In comparison to the constant switching between etch and deposition steps of the gas chopping technique, this reduction of processing time can provide a better throughput in future.

Accounting for the all mentioned advantages, the SF_6/O_2 cryoetching process shows a great promise for high aspect ratio silicon etching at the nanoscale.

4.7 Mixed mode technique

With respect to the silicon etching at the nanoscale, also a very interesting approach was developed by Mirza *et al.* [74]. The authors call it *mixed mode process* (simultaneous etch and passivation). The technique is based on a plasma chemistry obtained from the mixture $\text{SF}_6/\text{C}_4\text{F}_8$ ¹ in an ICP etching system at 20°C. By utilizing the developed etch method, Mirza *et al.* have created high aspect ratio (~ 50 : 1) sub-10 nm silicon nanowires (SiNWs) with smooth, uniform, and straight vertical sidewalls. Such etch results were obtained by the simultaneous balance between the etch and the passivation in the plasma process, which has been achieved through optimizing the platen and ICP powers, the SF_6 and C_4F_8 flow rates, as well as the chamber pressure.

Hydrogen silsesquioxane (HSQ), a high-resolution, negative-tone, inorganic resist for electron-beam lithography, was used by the investigators as the resist to define nanoscale patterns. Due to the mechanical strength of the HSQ resist, it was possible to repeatedly produce high resolution sub-10nm HSQ patterns with vertical profiles and aspect ratios up to 25:1.

The developed technique has demonstrated very good results for creating sub-10 nm silicon nanowires. However in this case, the lines and spaces are not equal, that is, the width of the space being etched between two nanowires is much larger than that of the nanowires. In contrast, accounting for the critical parameters of plasma etching processes (in particular, transport of plasma species inside the etched trench), a much more critical challenge of dry silicon nanopatterning is the etching of high aspect ratio trenches.

Concluding, despite the good results in creating silicon nanowires, the mixed mode technique

¹ SF_6 and C_4F_8 (correspondingly etching/deposition) are the most commonly used feed gases in gas chopping etching processes

should be examined by much more challenging tasks, such as for example the etching of high aspect ratio trenches in silicon.

4.8 Summary

The etch rate during plasma etching process is actually a combination of the *isotropic* component (due to the chemically reactive neutrals) and *anisotropic* component (due to the sputtering by energetic ion bombardment). Creation of inhibitor films on the feature surface, redeposition phenomena and presence of a big amount of contaminants in the gas-phase make the process even more complicated. Hence, the final feature profile shape is a result of sophisticated interaction between the all aforementioned components. That is why, plasma etch simulators are often the only way for a deep analysis of the process, revealing its dominant factors and giving insight into the details.

Chapter 5

Transport phenomena

In terms of plasma etching of silicon, the processed wafer (placed at the cathode) is exposed to the fluxes of various plasma species generated in the plasma. After reaching the sample, these particles, which are mainly positively charged ions and neutral radicals, cause different types of reactions with the materials of the considered microstructure thus providing the etching process. The etching reactions and their rates depend on different factors: fluxes of reactants and ions to the surfaces, concentration of species at the surface (surface coverage), angle of incidence and energy of impinging ions. Hence, a proper understanding of the transport of plasma species from the plasma bulk to the sample surface is very important in the context of plasma etching process in general and high aspect ratio silicon etching in particular.

The plasma species transport to the sample surface can be considered as consisting of two parts: i) particles' transport across the plasma sheath and ii) particles' transport close to the sample and inside the microstructure until the particles reach the surface or get reflected back towards the plasma bulk (*feature scale transport*).

5.1 Transport across the sheath and particle angular distribution at the sample

Due to the electric field, pointing from the plasma to the cathode, the positive ions with the velocity greater, than the Bohm velocity [15, 75], enter the sheath area and acquire strong acceleration while flying across the sheath, where they can collide with other particles. Number of collisions for the ion in the sheath on the way to the sample is a very important parameter which directly influences the ion energy and ion angle distribution functions (*IEDF* and *IADF*) at the surface of the processed wafer. Ions with a large deviation from normal incidence exhibit a lower kinetic energy [16], thus *IEDF* and *IADF* belong to the key parameters defining the etching process. Let d_s be the thickness of the sheath and λ_i the mean free path of ions in the sheath – the distance over which the uncollided ion flux decreases to $\frac{1}{\exp\{1\}}$ of its initial value at the initial position [15]. The ratio of the ionic mean free path over the sheath thickness λ_i/d_s can help to estimate

whether the sheath is collisional and how it influences the *IADF* [16]. This ratio depends on various conditions in the plasma reactor. One of the most important is the discharge pressure. Raising the pressure broadens both the functions *IEDF* and *IADF* [16]. Another one is the ion energy: for higher energies, the *IADF* becomes more sharply peaked [16]. For large values of λ_i/d_s , the *IEDF* and *IADF* are also significantly affected by the operating frequency, but for values of $\lambda_i/d_s \leq 5$, the influence is negligible. To summarize, to have most of the ions traversed without any collision across the sheath, the sheath thickness d_s should be small in comparison to the ionic mean free path λ_i . For an ICP plasma source, which is the subject of the current work, the typical sheath thickness is of order $100 \mu\text{m}$. Thus if the pressure in the reactor chamber is less than 100 mTorr, the ionic mean free path is significantly larger than the sheath thickness and the sheath can be considered collisionless. Otherwise, at more high values of the reactor pressure, it is considered, that collisions take place in the sheath, in which some extra factors should be taken into account when creating a sheath kinetics model.

Since in the presented work, the pressure value in all considered simulations was less than 100 mTorr, the plasma sheath was assumed to be collisionless. Therefore the ion angular distribution is almost unidirectional at the lower sheath boundary in the vicinity of the wafer surface. It can be well represented by a Gaussian distribution function. On the contrary, the electrons have to climb the potential barrier in order to leave the plasma bulk and reach the sample surface. Thus, they have almost isotropic angular distribution at the sheath lower boundary. The neutral radicals make their way across the sheath by diffusion and hence have an isotropic angular distribution when arriving at the cathode.

There are works[75–79], that addressed the problem of a sheath model creation.

5.2 Feature scale transport

Etch rates as well as resulting feature profiles depend on microstructure and in fact their dependence is linked[5]. The origin of this issue is the ion and neutral transport in the intra-feature area.

5.2.1 Transport of neutral reactants

It is generally assumed that the transport of neutral reactive species during reactive ion etching process occurs by one of two mechanisms[80].

The first mechanism is surface diffusion, in which neutrals, after they arrive from the plasma at the sample surface, adsorb on the upper sidewalls and subsequently diffuse along the walls to the bottom. The described mechanism has been proposed as a reason for microtrenching during trench etching with chlorine. However, recent experiments suggest that surface diffusion is insufficient to sustain etching in deep trenches[80]. Therefore, also the **ViPER** software does not consider the effect of surface diffusion during the plasma etch simulations.

The dominant neutral transport mechanism seems to be the other one, which is Knudsen dif-

fusion within the feature[80]. It can be described as follows. The neutral species arriving from the plasma at the sample surface either adsorb or strike and diffusely scatter upon exposed surfaces (including the upper sidewalls). A portion of the adsorbed species and the scattered species are reemitted and move across the feature to the other sidewall. Since under typical conditions the gas pressure is low enough to assume that the mean free path of neutral species is much larger than the feature dimensions, the neutral transport within the feature is collisionless. The cycle of reflection and/or adsorption/desorption is repeated until the particle either reacts with the wall of the feature or returns back into the plasma.

5.2.2 Ion transport

The transport of energetic ions in the intra-feature area involves several phenomena, which are as follows:

- ion shadowing
- ion reflections
- charging effect

The *ion shadowing* effect can be described as follows. Let an open area of the sample be the surfaces at the top of the sample where the incoming ion flux is equal to that coming from the plasma. In other words, the open area is exposed to all ions arriving from the plasma and is independent on the ion angular distribution at the lower sheath boundary. In comparison to the ion flux at the open area, the ion flux at the bottom of a deep trench is limited due to shadowing. Namely only a fraction of the ion flux reaches the trench bottom, while the rest of the ion flux (with the larger deviation to the normal incidence) is shadowed by the feature sidewalls.

The *ion reflection* phenomena stands for the ion scattering at the sidewalls. In particular, the ions with the most glancing angles of incidence have the highest probability to get reflected when impinging on the feature sidewall surface. Due to the ion reflection phenomena, the ions, which originally were not in a direct line-of-sight with respect to the trench bottom (the ion shadowing), obtain a possibility to move further into the depth of the trench. Thus, the ion reflection can result in larger ion flux at the trench bottom in comparison to the cases when the ion reflection at the sidewalls is negligible.

The influence of the ion shadowing and ion reflection phenomena was theoretically investigated by Abachev *et al.*[81], in which a cosine angular distribution was used for the reflected ions. The ion scattering was also considered in the work of Arnold *et al.*[80], where they have assumed specular reflection of ions – the reflection probability depends on the ion incident angle. Another important assumption made in the work was that only direct and single reflected ions were considered. The ions that got reflected more than 1 time were considered to have not enough energy to contribute to etching anymore.

The build-up of a surface charge on insulating materials of the sample induces local electric fields in the microstructure area which can become strong enough to alter the trajectories of impinging ions. This phenomenon which is often called *charging effect* can significantly complicate the profile control of etched features. Therefore, the charging effect is discussed in the next section **5.2.2.1: Charging effect** in more details.

5.2.2.1 Charging effect

The directionality difference between the positively charged ions, accelerated in the plasma sheath region, and negatively charged electrons builds charge on insulating materials of the sample (for instance, the resist mask or buried oxides). The resulting electric fields can distort the ion trajectories reflecting them to the trench sidewalls allowing lateral etching to occur. This is often a serious problem for the profile control, especially in the case of silicon etching at SOI (silicon-on-insulator) wafers. To overcome the RIE lag (see the definition in section **5.2.3: Pattern shape effects**), usually an overetch is employed, resulting for the SOI wafers in positive charge buildup on the exposed oxide layer due to the bombardment with positively charged ions. Fig. 5.1 illustrates how surface charge arises during plasma etching of silicon layer on a SOI wafer. Electrons do not reach the trench bottom, only charging negatively the mask. This causes the local electric field, which with the lapse of time becomes strong enough to influence the trajectories of the low energetic ions, coming from the plasma. Charging effect accounts for different profile distortions such as notching, bowing and trenching effects, which are particularly problematic for the profile anisotropy when etching high aspect ratio features [2].

Thus, it is very important to have a good understanding of the charging effect especially when etching high aspect ratio features. One of the main tasks of the current work was to develop a simulation model, that could address the charging effect during the entire course of the high aspect ratio etch process simulations. The model developed in the context of the work is described in details in chapter **7: Charging effect simulation**.

5.2.3 Pattern shape effects

Plasma etching of high aspect ratio features in silicon and other materials is becoming more and more important for micro- and nano-engineering. The *aspect ratio* (AR) is defined as the depth of the trench divided by its width. *Aspect-ratio-dependent etching* (ARDE) is a serious limitation in deep silicon etching: at high aspect ratios, excessive etch rate reduction for longer etching times occurs [82]. For example, local electric fields in the microstructure area, induced by differential surface charging, can account for the etch rate reduction by altering the ion trajectories and thus influencing the ion transport (the impact of charging effect can increase with the etch time). Moreover, ARDE depends on ion and neutral shadowing as well as on angle and energy distribution of ions at the lower boundary of the plasma sheath [5].

One of the most important techniques commonly used to obtain high aspect ratio features is

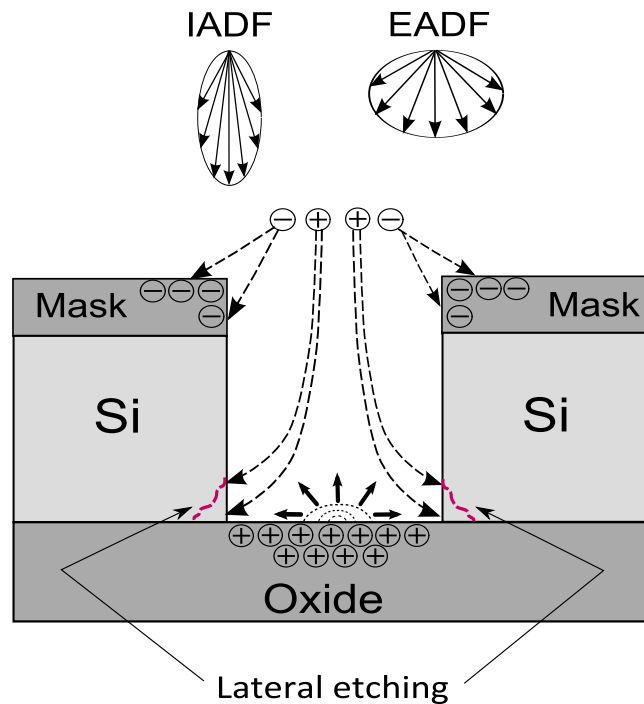


Figure 5.1: *Charging effect at plasma etching of SOI wafer. Local electric field in the trench is the reason for the deflection of the low-energetic ions to the sidewalls, leading to a lateral etching. IADF and EADF - angle distribution functions of the positive ions and electrons in the vicinity of the etched trench. Picture taken from [1]*

dry reactive ion etching (RIE). During etching of high aspect ratio features with RIE, the etch rate depends on time and the mask opening. In general, smaller trench openings are etched slower than those which are wider. This effect is often called *RIE lag* and seems to depend on the aspect ratio of the trench (that is, AR scaling) rather than on the depth or width of the trench (that is, feature size scaling) [83]. In addition to the conventional plasma reactors, also the hardware equipped with high density sources and cryogenic cooling are facing the same issues.

RIE lag effect should not be confused with ARDE effect. In the context of RIE lag, one etch time and many linewidths are compared, while in ARDE studies, many etch times are compared for the same linewidth value [82]. Due to the study done by Kiihamäki and Franssila [82], RIE lag phenomenon is not only high aspect ratio dependent. The researchers report that long narrow features are etched faster than wide short features, indicating the three-dimensional nature of the reactive ion etching lag. In his next work [84], Kiihamäki points out that higher aspect ratios can be achieved with increased ion directionality, and that amount of lateral etching can be decreased at the same time.

Aspect ratio *independent* etching was theoretically investigated by Lukichev [85]. Due to the conducted study, etch rates are aspect ratio independent at definite temperatures and flux ratios: ion/(passivating neutrals) and (active neutrals)/(passivating neutrals) ratios which influence the process. In summary, the author concludes that lowering of the temperature may be necessary for obtaining aspect ratio independent etching with a small decrease of the etch rate. In the subsequent work [86], Lukichev and Yunkin conducted a theoretical and experimental study of plasma etching

of silicon trenches in a wide range of aspect ratios. In their work, the authors have shown that under certain conditions etched trenches with different widths can be geometrically similar.

The term *Microloading* describes an etching rate dependency on pattern density. Usually, features in low pattern density areas etch faster than features of the same size in high pattern density areas [5]. Microloading can arise as a result of reactants depletion under conditions where the etching rate is reactant transport-rate-limited as opposed to surface-reaction-rate-limited. The influence of different processing parameters like, pressure, gas flow, and flow direction on the microloading effect in RIE was investigated by Hedlund *et al.* [87]. Due to the conducted study, the microloading effect is very dependent on pressure in the reactor chamber. Moreover, the microloading phenomenon is amplified if the available amount of etchants is reduced by, e.g., decreasing the gas flow rate. In contrast, the gas flow direction is reported to have no influence on the microloading because there is a stagnant gas layer close to the substrate surface [87].

Chapter 6

ViPER simulation software

6.1 Motivation

Due to the great complexity of physical and chemical phenomena inside the reactor chamber, the conducting large number of time and cost consuming plasma etching experiments is often insufficient to determine the process window allowing desired profile control. Moreover, even two equal plasma processing hardware can yield different results using the same recipe for the experiment. Accounting for these factors, the utilization of simulation software is unavoidable for optimization and further development of the silicon dry etching processes. Indeed, addressing each critical aspect of plasma etching by a corresponding model and including/excluding it from the simulation, one can assess their importance and interaction in terms of the considered experiment.

The simulation gives also an ability to address the problem on the macro level (processes occurring within the scope of the entire plasma reactor) and the micro level (processes occurring close to and within the etched microstructure). Furthermore, the problem allows to be considered at different levels of abstraction (generation of species in the plasma, transport of charged and neutral particles, gas-surface kinetics, time evolution of the surface profile, etc.). Since a feasible simulation of plasma processes, occurring in the reactor chamber of the etch hardware (macro level or also called *reactor scale level*), is mostly an extremely complicated and time-consuming task, it is often instructive to conduct the simulations exclusively at the micro level (also called *feature scale level*). Despite the task reduction, such approach is usually still very beneficial. This is explained as follows. Provided the simulation software is calibrated for a given plasma etch hardware. Then by utilizing the simulator for a considered plasma etch recipe, one obtains not only better insight into the considered etch process, but also by comparing the resulting experimental and simulated profiles, it is possible to recover approximate flux values for incident ions and neutral radicals at the sample surface, without using expensive special equipment or conducting time-consuming plasma simulations at the reactor scale.

The utilization of processing gas mixtures (such as SF_6/O_2) gives rise to a large number of plasma species in the reactor. However, the real plasma chemistry is indeed even more compli-

cated due to the contaminants arising from reactions of the generated plasma species with different materials inside the chamber (reactor walls, cathode, mask material, redeposition of the etch products). For instance, the sputtering of the electrostatic chuck holding the sample can significantly increase the fraction of oxygen in the gas phase, thus leading to different and often unexpected experimental results. Despite assumptions and simplifications made in the models, the simulations are able to quickly deliver a general impression about the feature profile evolution as well as about the importance of each of the secondary effects in terms of any considered plasma etching recipe.

Plasma etch simulators can be also used to teach the operating personnel working with plasma etch hardware. The acquired knowledge can help in designing of experiments, where the desired result could be achieved much faster, thus also economizing costs and time.

6.2 Existing plasma etch simulators

During last 30 years, a big amount of profile simulators of reactive ion etching processes have been developed by many research groups across the globe. Pursuing various research objectives, the developed program codes became more and more sophisticated due to including more realistic and complex models and improving simulation approaches as well. Because of the big number of developed plasma etch simulators, only several of them will be mentioned here in order to give a general impression about the progress done in this research area. A more detailed information can be found in specially dedicated review works (for example in the review done by Guo and Sawin [88]).

In 1979, first profile simulations for RIE processes were done by Viswanathan [89] and Reynolds *et al.* [90]. The group of Reynolds used string algorithm for modeling of the feature profile evolution. Both works allowed for the isotropic and directional etch rates while, because of low aspect ratio of the considered features, such transport effects like shadowing or reflection of ions were neglected.

In 1983, the etch yield dependence on the incidence angle of impinging ions of different materials (Si, Au, Cr, PMMA and AZ1350 photoresists) was considered by Rangelow in the context of profile simulations of ion milling processes [50]. The employed model neglected reflection of ions and redeposition of sputtered material. However in a subsequent work [91], the model by Rangelow *et al.* already considered these two phenomena as well as other secondary effects like shadowing and trenching for simulation of ion milling processes (1985). Along with the sputtering yield dependence on the ion angle of incidence, the mentioned computer program also considered ion angular (IADF) and energy distribution functions (IEDF).

In 1989, Ulacia and McVittie [92] have presented a two-dimensional plasma etching simulator allowing for the species transport across the plasma sheath. Like in the model first introduced by Kushner [93], Ulacia and McVittie used a Monte Carlo method for simulation of ion transport across the sheath, yielding ion angle and energy distributions as well as species' fluxes arriving at the sample surface. The developed model also considered shadowing and reflection of ions, while

shadowing or reflection of neutral radicals was neglected.

Also in 1989, Thoren *et al.* [94] developed a semi-three-dimensional model which benefited from the symmetry of considered mask opening shapes. In addition to shadowing, the model also took the effects of faceting, deposition, redeposition as well as the phenomenon of surface diffusion into account.

Plasma sheath dynamics along with surface reaction kinetics and feature profile evolution were considered in the simulations done by Fichelscher *et al.* [76].

In 1994, Arnold *et al.* [95] have demonstrated the application of the method of characteristics for simulation of surface topography evolution during plasma etching.

Profile simulations of gas chopping etching processes were addressed by Volland *et al.* [8, 96] (2002, 2003) and later by Shumilov *et al.* [97] (2009).

The simulation software developed in 2002 by Cooperberg *et al.* [98] for semiempirical profile simulation of aluminum etching in a Cl_2/BCl_3 plasma was later used by Belen *et al.* [99–101] (2005, 2006) in their feature scale simulations of low-temperature dry silicon etching.

Despite the big amount of already existing scientific works and some commercially available plasma etch simulation software, the simulators which are able to simultaneously address the big variety of physical and chemical phenomena during plasma etching, and which by yielding plausible results would give a possibility of deep analysis of the most significant effects like RIE lag, charging, notching, bowing, microtrenching, profile shape dependence, etc., are still lacking.

To this end, last few years, the MNES (Micro- and Nanoelectronic systems department) research group at Ilmenau University of Technology has been developing under the direction of Prof. Ivo W. Rangelow a new plasma processing simulation software named **ViPER** (Virtual Plasma Etch Reactor). The developed computer simulation program is shortly described in the following section.

6.3 ViPER simulator overview

A plasma etching simulation software, containing corresponding physical models, can be used to establish a link between etch process parameters such as pressure, rf power, etching gas chemistry, temperature, and the physical and chemical process parameters like energy and angular distribution of ions and neutrals, radical sticking, and surface charging, etc.

Using previous works [7, 8, 57, 96], the research group under the direction of Prof. Ivo W. Rangelow at Ilmenau University of Technology (Department of Microelectronic and Nanoelectronic Systems (MNES)) has been developing a new plasma etch simulator named **ViPER** (Virtual Plasma Etch Reactor). The developed computer program [9] is a full featured plasma processing simulation software which was partly developed in frame of the European research project NanoPlasma funded by the European Commission Sixth Framework Programme (Contract No.016424). In the simulator, an inductively coupled plasma (ICP) reactor simulation environment is combined with a 2D feature scale etch simulation [11]. In other words, for a big variety of tasks,

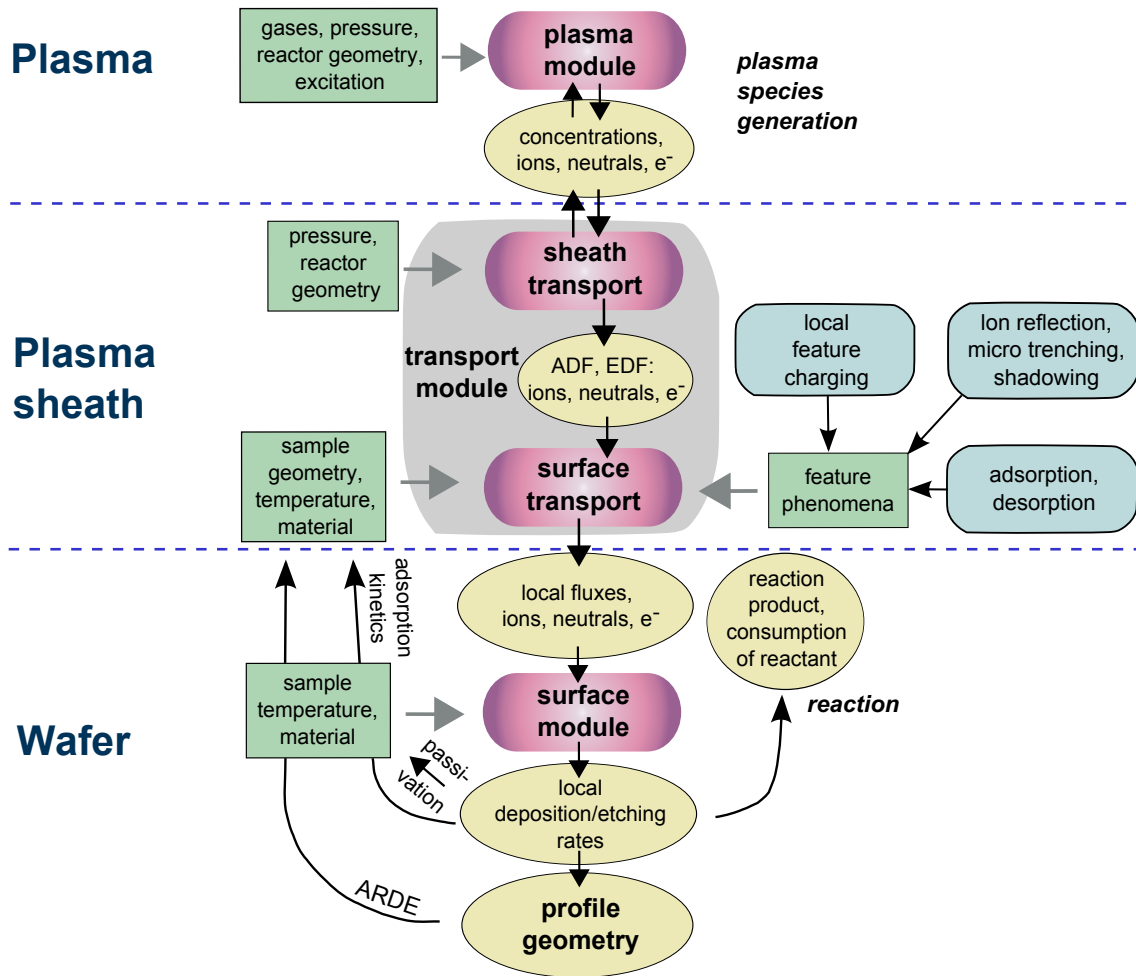


Figure 6.1: Common architecture of the ViPER simulator. Picture taken from [1] and modified.

the ViPER software can incorporate tool scale plasma chemistry and feature scale trench evolution.

The common structure of the program is shown in Fig.6.1. General simulation loop is a sequence of steps, where each step represents a certain period of time of the etching process. At the end of each time step the geometry of the simulated feature profile changes according to the calculated distribution of the plasma species fluxes along the feature surface.

6.3.1 Plasma bulk model

Using initial process parameters, peculiar to a convenient ICP plasma processing equipment (e.g. ICP power, pressure etc.), the implemented plasma simulation reactor scale module yields as an output the sorts of the ions and neutral radicals and calculates their densities in the gas phase. At the moment the program can deal with SF₆, C₄F₈ and O₂ plasmas. However due to the plug-in structure of the software, the list of available plasma models can be extended. Detailed description

of the implemented gas phase model can be found in [11, 102, 103].

6.3.2 Plasma sheath model

The transport of the plasma species from the plasma to the sample is simulated by means of a plasma sheath model. Using the plasma species density values as an input, the model yields the energy and angle distributions on the lower sheath boundary for each given species. In the case of charging effect simulation, the charging simulation module, using these calculated distributions as an input data for the charged particles, should provide further transport of electrons and positively charged ions in the vicinity of the sample surface. One of the sheath models, which is currently used in the ViPER simulator, was described by Hauguth *et. al.* [11]. This simple model yields a constant energy value for each species. There are works [75–79], that addressed the problem of more precise sheath model creation. In order to provide high-quality calculations of angle and energy distributions of charged species, necessary for the desired precision of the charging effect simulations, the ViPER software employs the sheath model developed by Lieberman [75].

6.3.3 Feature scale transport models

The feature scale transport effects are usually presented by such phenomena like species shadowing, local surface charging, ion reflections and microloading. All program modules, responsible for the transport of species in the vicinity of the sample, yield distributions of the species' fluxes on the sample surface as a result. The feature scale transport models for neutral species flux calculations on the sample surface, used in the software, were described by Hauguth *et. al.* [104]. The approaches, used by the ViPER software for simulation of feature scale ion transport in the absence of local electric fields, were described by Volland [7] and Hauguth [10].

6.3.4 Surface reaction models and surface profile evolution

At the moment for simplicity, the simulator considers two-dimensional cases of plasma processing. The surface profile evolution employs a string algorithm, where the feature cross-section profile is represented by a sequence of nodes. Due to the implemented simulation algorithm, the whole plasma processing simulation time is divided into a number of time steps. At each regular time step the flux of each plasma species is calculated for all points of the surface. Obtained values are used by the corresponding surface reaction models for the computation of etching/deposition rate in each surface profile node. Calculated etching rate values are then used to provide the surface profile evolution. At the moment, the developed surface reaction models can operate only with species, generated by SF₆, C₄F₈ and O₂ plasmas, but the list of the models can be extended due to the plug-in mechanism used in the software. The surface reaction model, used for simulations of etching of silicon by SF₆ plasma species, was described by Hauguth *et. al.* [11].

Chapter 7

Charging effect simulation

7.1 Motivation and state of the art

The issue of surface charging plays a very significant role in high aspect ratio deep silicon etching. The charging effect is attributed to the formation of local electric fields in the etched microstructure area, which steers positively charged ions to the sidewalls allowing lateral etching to occur. Continuing progress in very large scale integration (VLSI) requires further miniaturization of semiconductor devices, thus in modern fabrication of integrated circuits the etching process must be controlled at the nanometer scale. Understanding the effects of surface charging on the evolving feature profile is a key to achieving this level of control. Utilization of SOI (silicon-on-insulator) wafers in the modern chip and MEMS (micro-electro-mechanical systems) fabrication enables continuous performance increase of the microelectronic devices, described by the Moore's law. The charging effect is most pronounced while etching high aspect ratio features in polysilicon layers of SOI-wafers [2] and is often accounted for a so called *notching* phenomenon. The notching effect describes the opening of a long narrow groove (*the notch*) in silicon material layer at the interface with an underlying insulator[105]. One of the most often used plasma processing technologies, utilized in the MEMS fabrication to obtain high aspect ratio anisotropic features, is the gas chopping technique. Fig. 7.1 demonstrates the notching effect during a typical SOI-wafer etching experiment using a $\text{SF}_6/\text{C}_4\text{F}_8$ gas chopping approach. Such effects can be very harmful for the anisotropy of the etched trench profile.

It is very important for modern chip and MEMS fabrication to obtain a better understanding of charging effect and to be able to predict it. Obviously, the utilization of charging effect simulation model can help in investigation of physical processes, leading to the profile distortion, as well as to adjust the plasma processing parameters in order to avoid charging effect for each given process recipe, without carrying out numerous time and cost consuming plasma etching experiments.

Models taking into account the charging effect and related difficulties of creating such models have been already discussed by other groups [105–111]. Economou and Alkire [106] modeled the periodic charging of the surface taking into account the temporally modulated electron flux

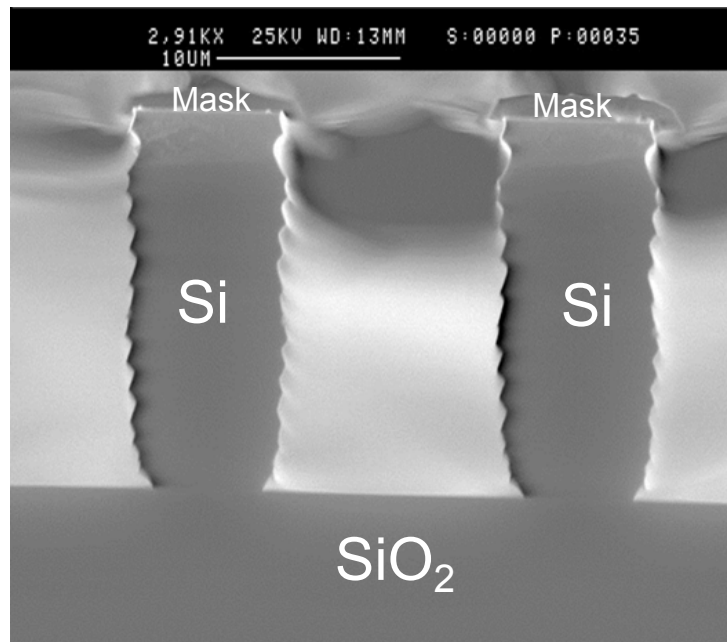


Figure 7.1: Notching effect during plasma etching of silicon on SOI wafer using an SF₆/C₄F₈ gas chopping approach. Experiment by the courtesy of Oxford Instruments Plasma Technology. Picture taken from [1].

and constant ion flux. Arnold and Sawin [107] were the first, who have considered localized surface charging, caused by the directionality difference (see also the description in section 5.2.2.1: *Charging effect*) of the isotropic electron and the anisotropic ion fluxes. As a simplification, they assumed the ion flux to be monodirectional and used a constant value for the initial energy of both, ions and electrons, without taking into account the influence of the alternating voltages in the sheath. In further works, Ootera *et al.* [108] considered the electron velocity distribution, but without taking into account the ion velocity distribution. A great advancement to the charging effect modeling was made by Kinoshita *et al.* [109] who started considering the effects of a polysilicon conductivity as well as effects of sheath oscillations, yielding more plausible angle and energy distributions of the charged particles. Later, Hwang and Giapis [105] have made a significant research of the notching effect by means of further enhancement of the model. They considered both, ion forward deflection and scattering mechanisms for the precise calculation of the notch evolution. They have also improved the algorithm for the potential redistribution in the conducting materials, in which they redistributed electric charges on the surface in such a way that the conducting surface became equipotential. Matsui *et al.* [111] have numerically investigated the influence of the charging effect on the oxide etching. However, in these works, a simulation of the charging effect was usually considered separately, using the profiles of already etched trenches, for the determination of the appearing electric fields and their impact on particle flux distribution along the sample surface. Models, giving a possibility to consider the charging effect during all the plasma etching simulation process and simultaneously yielding plausible results, are still lacking.

Considering the above mentioned conditions, the main requirement to the new charging effect simulation model developed in this work, was an ability to consider the local surface charging continuously, namely it should be used in the surface profile evolution over the entire course of the

etching process. Using such an approach would give a possibility to observe, how the local surface charge evolves with the feature profile and affects the final shape of the etched feature. It should make the application of the charging effect simulations much more universal, allowing to utilize the new model in etch simulations not only for the SOI-wafers but also for the conventional silicon wafers, taking into account the local surface charging of the hard masks, like SiO_2 . Simulation of the gas chopping etching experiments is one of the most significant features of the **ViPER** software. Surface scallops, characteristic of the etched features obtained by the gas chopping process (see 7.1), can make the geometry of the simulation area very complicated in terms of the electric field calculations. Therefore, the second requirement to the model was as follows. The model should be able to effectively handle such geometry irregularities, keeping the acceptable precision of calculations and still with a desirable speed of the whole simulation process. The insulating mask materials used for the wafer patterning, often have different dielectric permittivity values, which can also have a certain impact on the local electric fields in the microstructure area. That is why, the third requirement to the new model was the ability to consider the electric field not only in the gas phase area between the features but also in the insulating materials of the sample. This would give an additional possibility, to estimate and compare the impact of either different mask configurations or oxide layer thickness on the surface charging, thus, on the shape evolution of the feature profile.

7.2 Position of the charging simulation model in the ViPER software architecture

The processed wafer is permanently bombarded by the charged particles, and this, in turn, changes the local charge distribution on the insulating surfaces, thus, the local electric fields. With the lapse of time such system reaches steady state, where the fluxes of charged species for any point on the surface do not change any more. In reality, this takes usually much less time (milliseconds), than the feature profile evolution itself, considering that typical plasma processing simulation time steps are in seconds. The fluxes, found at the charging steady state, should be considered in the etching/deposition rate calculations. These particle fluxes should be computed by the implemented charging effect simulation model. Undoubtedly, the charging steady state species fluxes distribution depends on the system geometry, thus, it will be different for each plasma processing step. Since the charging effect model should take into account all changes of the surface profile shape, it should be utilized at each step of the general simulation loop (see also section **6.3: ViPER simulator overview** for more details). Fig. 7.2 shows the position in the architecture of the **ViPER** simulation software, where the developed charging model should be employed, in order to provide the transport of charged particles in the area close to the microstructure surface.

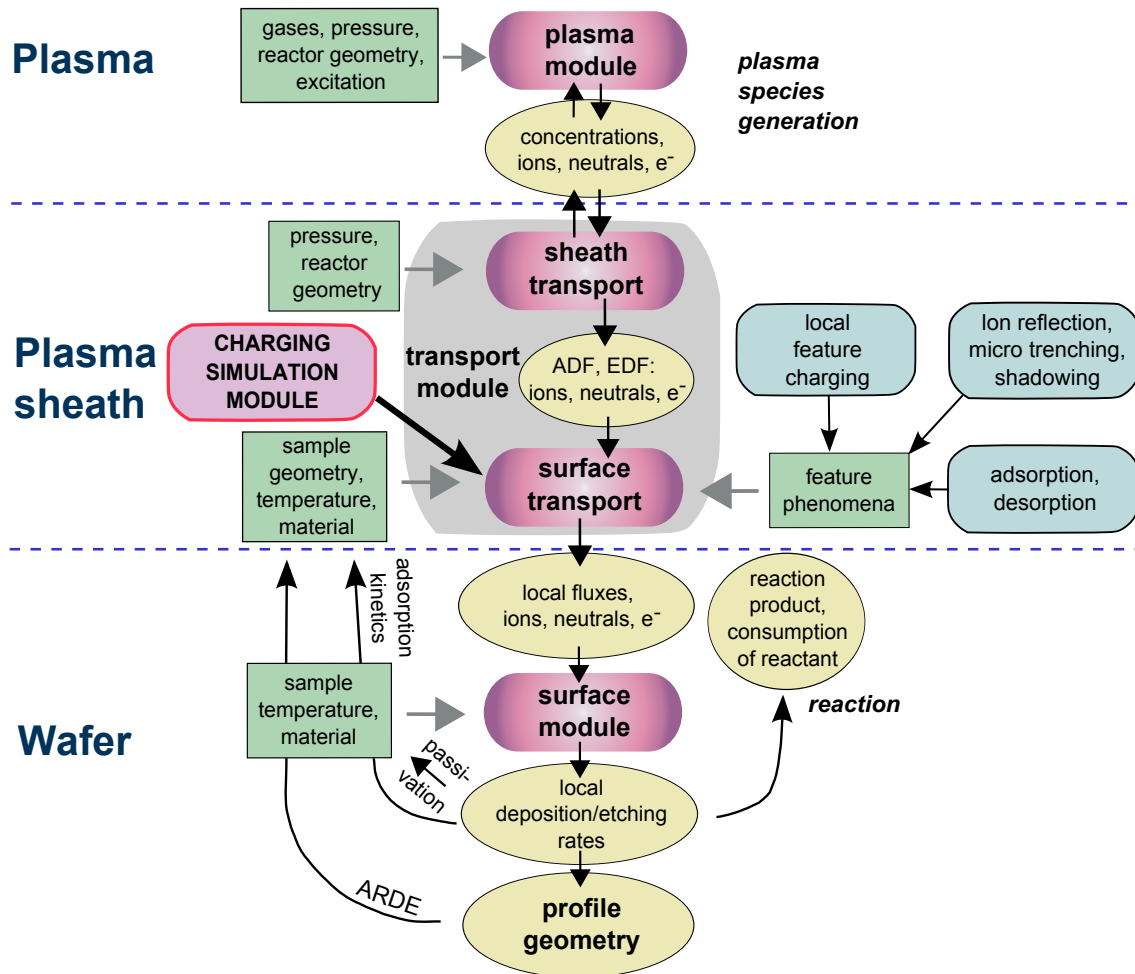


Figure 7.2: Position of the developed charging effect simulation model in the architecture of the ViPER simulator. The model should use output data of the sheath simulation module and provide the transport of charged particles through the microstructure area, yielding the distribution of the charged species fluxes along the feature surface. Picture taken from [1] and modified.

7.3 General structure of the developed charging model

The flow chart in Fig. 7.3 represents the structure of the implemented charging model, used for determination of the steady state data, whereas the geometry of the charging simulation area does not change. As initial data, the model takes both, the geometry of the feature profile as well as the charge density distribution along the profile. Each step of the charging model common loop represents a charging simulation iteration, or, in other words, a modeling of the regular attempt of the system to achieve the steady state. A charging simulation step begins with the calculation of electric field in the simulation area, taking into account current surface charge distribution. After that, the transport of the charged species through the area of interest is calculated using as an input the angle and energy distribution functions (ADF and EDF correspondingly) as well as the current

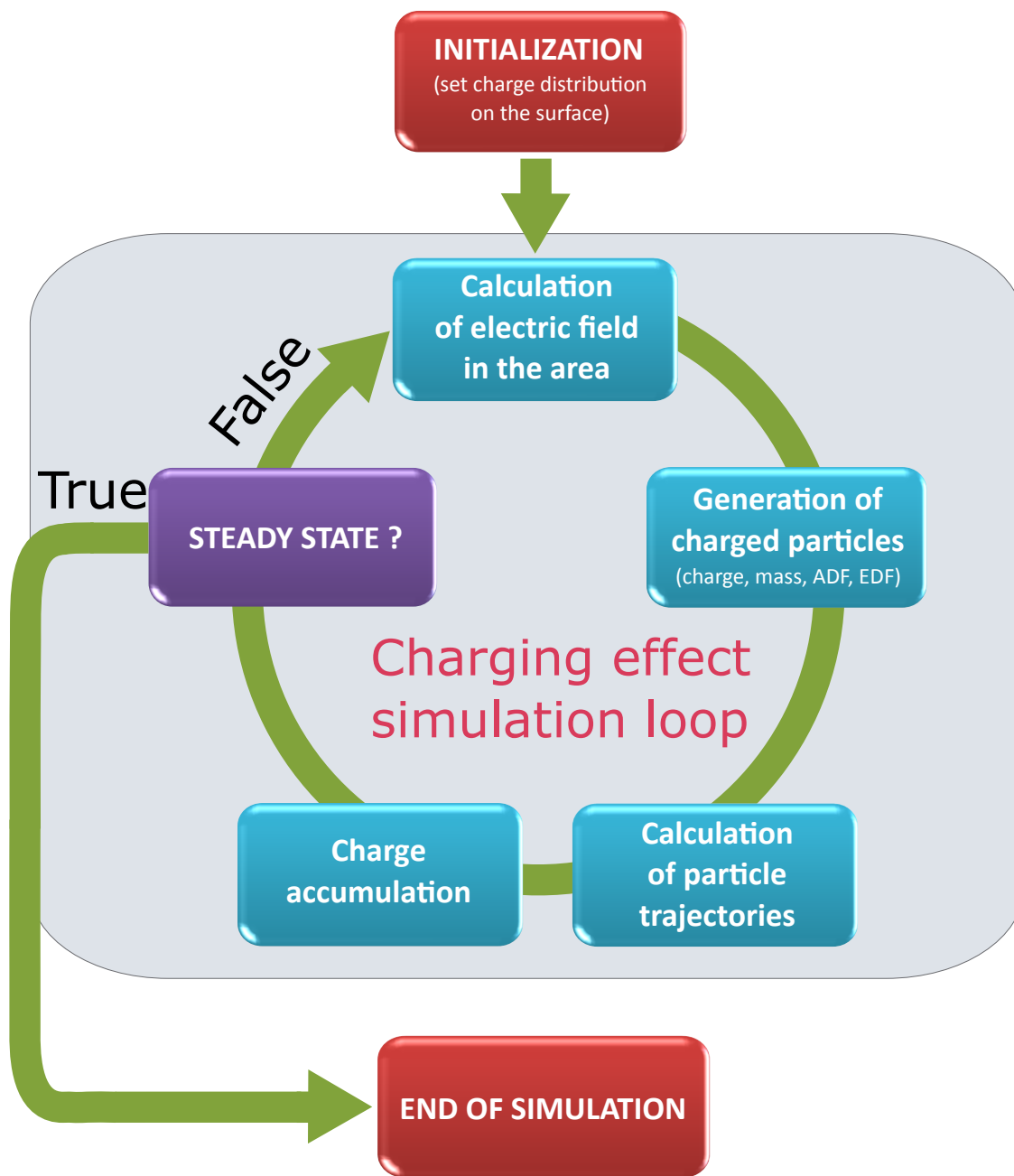


Figure 7.3: Schematic representation of the implemented charging effect simulation model. As soon as a charging simulation is finished, the calculated positive ion flux distribution along the feature profile is passed to the general plasma etch simulation module for the computation of etching rates and further profile evolution

density values, already determined by the plasma sheath model. Particle trajectories are modeled for a certain period of time with a consideration of the newly calculated electric field values. As soon as the charge transport is completed, resulting charge density values in each point of the surface profile are calculated, yielding a new charge density distribution along the surface, whereas the dissipation of charge differences through the wafer is considered: for the silicon surface, it is assumed that the passivation film is either very thin or removed completely, and the surface charges become neutralized by simple conduction. At the end of each charging simulation step,

it is determined whether the system has already reached the steady state. In the case of steady state, the charging model calculates the positive ion flux distribution along the feature profile. The found values are used by the general plasma processing simulation module for the etching rates computation and further profile shape evolution. Within the context of a plasma etching simulation, the charging model should solve two main problems: (i) calculation of the local electric field in the area of interest, and (ii) simulation of the charged particles transport through this field.

7.4 Definition of charging simulation area

The problem was reduced from a three-dimensional to a two-dimensional case, as it was assumed that the considered cross section of the feature is far from both ends. Then, the electric field has a negligible longitudinal component (along the trench length), since the surface charging does not change along that axis in this case [107]. Apparently, the longitudinal momentum of the charged particles will not undergo certain impact and it is sufficient, to consider a two-dimensional case for getting plausible results. In Fig. 7.4, it is shown how the developed charging model defines the simulation area in 2D plasma processing simulations in the **ViPER** simulator. In order to make the modeling realistic, the adjacent trenches are also considered, since their surface charging also makes a significant contribution directly to the electric fields in the area of interest [105]. That is why the actual charging simulation area is mirrored to the left and to the right side regarding the mirror lines (see Fig. 7.4). The local surface charging of the microstructure induces a dipole electric field, which vanishes very fast with increasing of distance [105]. Thus, the charged particle trajectories are influenced only in the vicinity of the feature profile. In the present model implementation, the term *plasma sheath lower boundary* is defined as a straight horizontal line close to the sample surface. The plasma sheath lower boundary is simultaneously the upper boundary of the considered charging simulation area (see Fig. 7.4).

7.5 Electric field calculation module

The electric field in the area of interest is a superposition of the plasma sheath electric field and of that induced by the local surface charging. In order to make the model less sophisticated but still feasible, several assumptions were made.

Like in previous works [105, 107], the net charge flux at the sheath lower boundary is assumed to have a time-averaged value of zero, forcing the macroscopic surface potential to be constant over the entire time of charging simulation. Thus on each charging step, the model needs to address equal fluxes of the positive ions and electrons. In reality, the flux of electrons to the sample surface is modulated by the radio frequency (*rf*) sheath field and reaches the sample only over a small fraction of the *rf* cycle. In the context of the developed model, it was assumed that the ion and electron fluxes do not change during the entire progress of charging simulation. The variation of the periodic surface potential was estimated to be less than 0.1 V for typical processing conditions [106]. In comparison to the time-averaged electric potential caused by the local charging of the

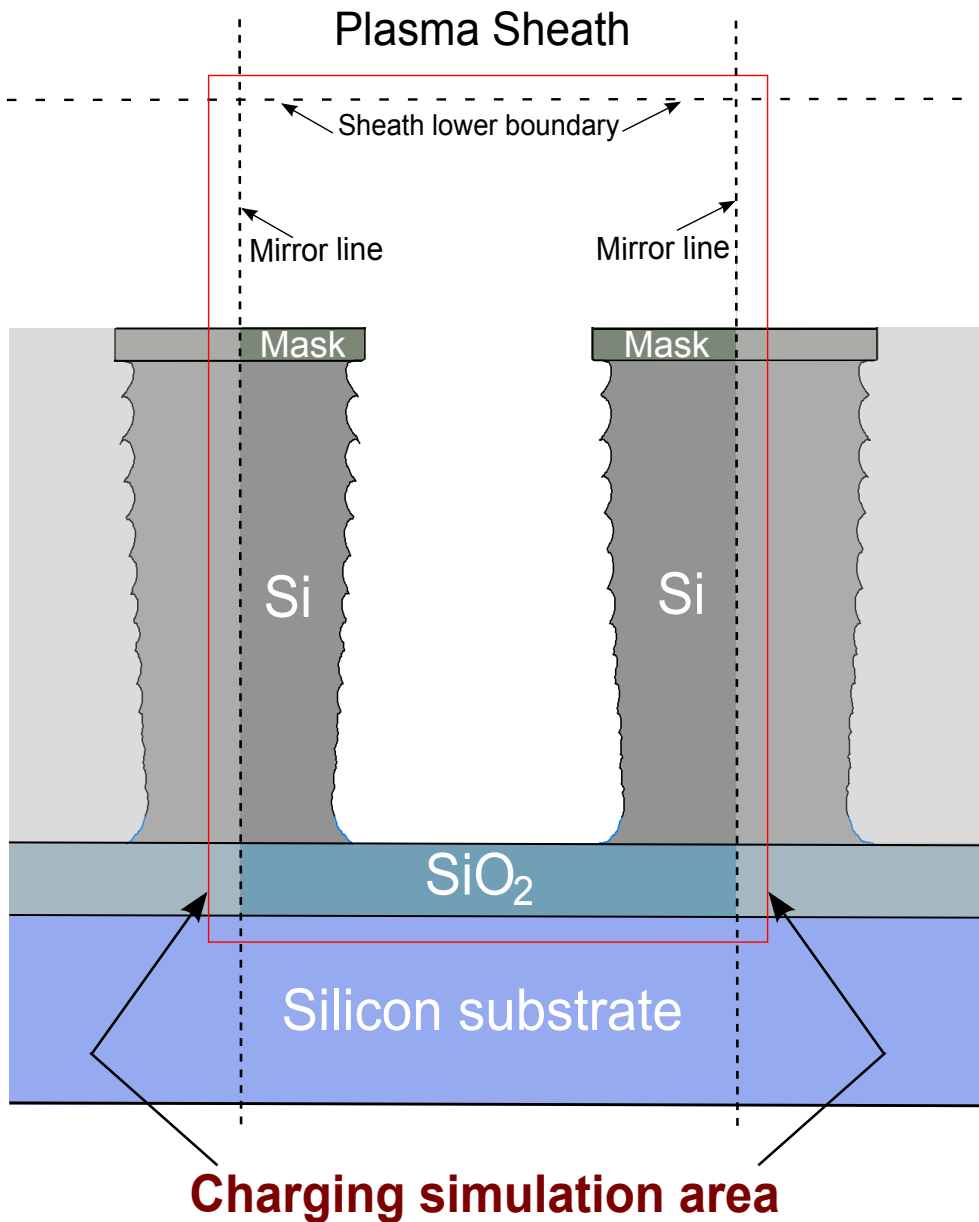


Figure 7.4: Definition of the charging effect simulation area according to the developed model. Picture taken from [1].

feature surface, this periodic potential variation is two orders of magnitude less [107], and will be ignored in the developed model. Hence, it can be assumed, that the energies of electrons and ions do not depend on time [107]. Typical gradients of electric potential in the plasma sheath are on the order of 1 kV/cm [107]. This would mean potential differences over the length scale of a 0.1 μm . In other words, the electric field of the plasma sheath does not have any significant effect on the acceleration and trajectory of the charged particle in the vicinity of the sample. Therefore, the sheath potential gradient will be neglected by the model in the calculations of electric field close to the microstructure and inside the etched trenches.

It is also assumed that during the charging step, the profile surface charge distribution remains

constant, that is, the charge diffusion along the profile surface is neglected. Thus, the problem of electric field calculation is restricted to the electrostatics problem, whereas the appropriate Maxwell equations will have the following form

$$\operatorname{div} \vec{D} = \rho \quad (7.1)$$

and

$$\nabla \times \vec{E} = 0, \quad (7.2)$$

where \vec{D} is the electric displacement vector, \vec{E} is the electric intensity vector and ρ is the charge density in a given volume.

Since the curl of a gradient is zero (Eq. 7.2), this implies that the electric field can be derived from the gradient of a scalar potential [15]:

$$\vec{E} = -\operatorname{grad} \varphi, \quad (7.3)$$

where φ is the scalar electric potential.

This gives a possibility to restrict our considerations with the calculation of a scalar electric potential distribution in the simulation area. The electric displacement \vec{D} and electric intensity \vec{E} vectors are connected by means of the following Maxwell material equation

$$\vec{D} = \varepsilon \cdot \vec{E}, \quad (7.4)$$

where ε is the dielectric permittivity of the given material.

Using Eq. 7.4 and Eq. 7.3 in Eq. 7.1 results in

$$\operatorname{div}(\operatorname{grad} \varphi) = -\frac{\rho}{\varepsilon} \quad (7.5)$$

or

$$\Delta \varphi = -\frac{\rho}{\varepsilon}, \quad (7.6)$$

which is the Poisson differential equation for the electric potential distribution, where $\varphi(x, y)$ is the scalar electric potential, $\rho(x, y)$ is the charge density distribution in the simulation area and ε – the dielectric permittivity value for the medium.

Since the area of interest has significantly smaller dimensions than the mean-free path of the considered charged particles, it is assumed, that the spatial charge density in the simulation area equals zero. This leads to a reduction of the problem to solving the Laplace differential equation

$$\Delta \varphi = 0, \quad (7.7)$$

or for the two-dimensional case

$$\frac{\partial^2 \varphi}{\partial x^2} + \frac{\partial^2 \varphi}{\partial y^2} = 0. \quad (7.8)$$

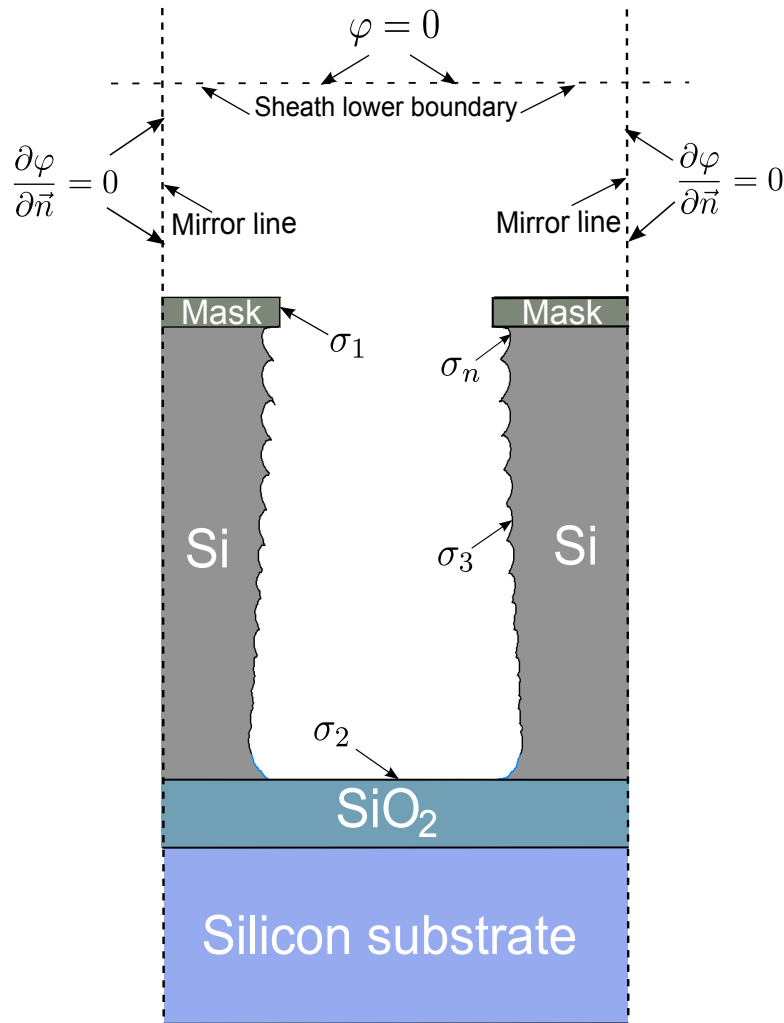


Figure 7.5: Representation of the boundary conditions used for the electric field calculation in the simulation area. \vec{n} - the outer normal vector. φ - the electric potential. $\sigma_1, \sigma_2, \sigma_3, \dots, \sigma_n$ - the charge density values in each point of the surface. A Dirichlet boundary condition is applied for the sheath lower boundary. For the mirror lines, a Neumann boundary condition is used. The surface charge density values are employed in the boundary condition development for a considered feature surface profile. Picture taken from [1].

7.5.1 Definition of the boundary conditions

In the context of the outlined boundary value problem, some assumptions for definition of the boundary conditions should be made (see Fig. 7.5). First, as already mentioned above, the model neglects the effect of the electric field of the plasma sheath in the particle trajectories calculations. The local electric dipole field in the microstructure area vanishes within a short range. Using a Dirichlet boundary condition, this is considered for the plasma sheath lower boundary by setting there the electric potential value to zero (see Fig. 7.5):

$$\varphi = 0. \quad (7.9)$$

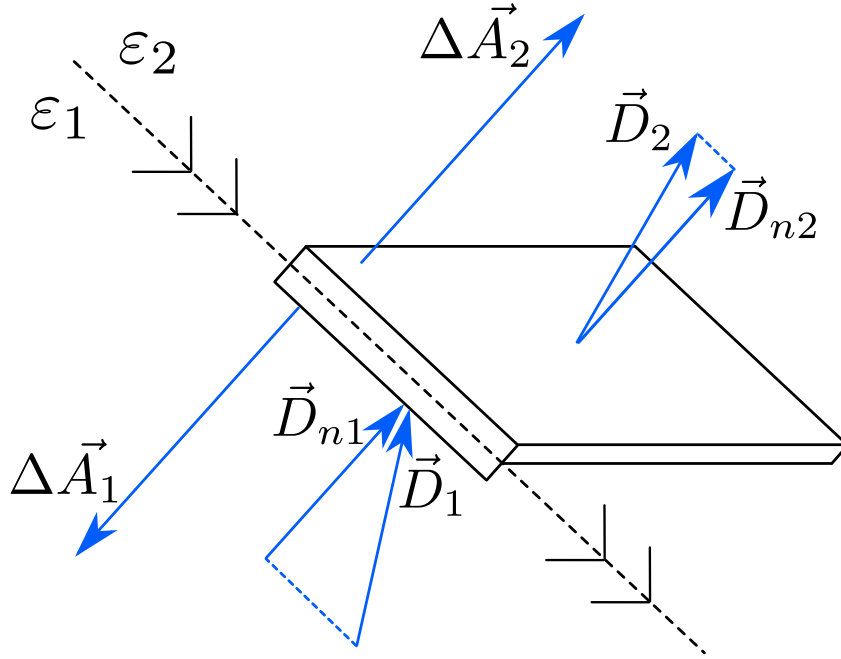


Figure 7.6: *Interface conditions for electric displacement field. The infinitesimal part of the boundary area between two media with permittivities ϵ_1 and ϵ_2 , containing homogeneously distributed charge density σ .*

Second, in order to implement the mirroring of the simulation area, a Neumann boundary condition is used, in which the value of the normal derivative of the electric potential should be zero for both, left and right mirroring lines (see Fig. 7.5):

$$\frac{\partial \varphi}{\partial \vec{n}} = 0, \quad (7.10)$$

where \vec{n} is the outer normal to the mirroring line.

The boundary conditions for the surface of the microstructure are determined with the help of the charge density values in each point of the feature profile surface. In order to develop the finite formula, establishing the desired relation between the charge density and electric potential unities, Gauss's law of electrostatics is employed:

$$\oiint_A \vec{D} \, d\vec{A} = Q, \quad (7.11)$$

which states, that for a hollow object, the flux of the electric displacement vector \vec{D} through the closed surface A , enveloping this object, is equal to the sum charge Q , located inside this object[15].

Each point of the quantized surface profile is considered as infinitesimal volume having some charge inside, or in other words, some charge density σ for the given surface profile area. For further considerations, interface conditions between two media are taken into account, where the media have dielectric permittivity values appropriately equal to ϵ_1 and ϵ_2 (see Fig. 7.6). The electric displacement vectors \vec{D}_1 and \vec{D}_2 are defined correspondingly in the first and in the second medium.

The thickness of the considered boundary part is assumed to be thin enough, that it can be neglected, while the both remaining interface faces have the same area: $\Delta A_1 = \Delta A_2$.

Then the total flux of the electric displacement vector can be represented as the sum of the separate fluxes through the faces

$$\iint_{\Delta A_1} \vec{D}_1 \cdot d\vec{A}_1 + \iint_{\Delta A_2} \vec{D}_2 \cdot d\vec{A}_2 = Q. \quad (7.12)$$

Since here only normal components of the vectors play a role, we get

$$\iint_{\Delta A_1} \vec{D}_{n1} \cdot d\vec{A}_1 + \iint_{\Delta A_2} \vec{D}_{n2} \cdot d\vec{A}_2 = Q. \quad (7.13)$$

As the considered interface faces have an infinitesimal area, it is assumed, that the electric displacement vectors are constant on the appropriate faces.

Using

$$Q = \sigma \cdot \Delta A_2$$

and taking into account directions of the vectors, we obtain

$$-D_{n1}\Delta A_1 + D_{n2}\Delta A_2 = \sigma \cdot \Delta A_2. \quad (7.14)$$

Since $\Delta A_1 = \Delta A_2$, Eq. 7.14 can be transformed into the following expression:

$$D_{n2} - D_{n1} = \sigma, \quad (7.15)$$

which is the interface condition for electric displacement field.

Recalling the appropriate Maxwell material equation (Eq. 7.4), the developed interface condition can be also formulated in the context of electric intensity vector:

$$\varepsilon_2 E_{n2} - \varepsilon_1 E_{n1} = \sigma. \quad (7.16)$$

In terms of the charging effect simulations, the first medium is always vacuum, hence, $\varepsilon_1 = 1$. If the electric field in the second medium is not considered, then $E_{n2} = 0$, and therefore

$$E_{n1} = -\frac{\sigma}{\varepsilon_0}, \quad (7.17)$$

where ε_0 is the vacuum permittivity.

Or, using Eq. 7.3, the inhomogeneous Neumann boundary condition for the conducting surface of the feature profile looks as follows

$$\frac{\partial \varphi}{\partial \vec{n}} = \frac{\sigma}{\varepsilon_0}. \quad (7.18)$$

However, if the second medium should be also taken into account ($E_{n2} \neq 0$), then Eq. 7.16 with respect to E_{n1} looks like

$$E_{n1} = \varepsilon_2 E_{n2} - \frac{\sigma}{\varepsilon_0} \quad (7.19)$$

That is, two unknown variables E_{n1} and E_{n2} are present in one equation. This issue was addressed and solved while implementing the numerical solver for the calculations of electric potential distribution, and will be discussed later in section **7.5.2.4: Consideration of the boundary integral** and in Appendix **A: Neumann boundary condition between two insulators**.

7.5.2 The finite element method (FEM) solver

An analytical solution of Laplace's equation is usually possible only for systems with simple geometry, possessing certain symmetry. Otherwise, if striving to find the solution for more general tasks with sophisticated geometries, the utilization of numerical techniques is unavoidable.

The most commonly used numerical methods for determination of electric fields belong to one of the following categories:

- Finite difference methods (FDM)
- Finite element methods (FEM)
- Spectral methods
- Boundary element method (BEM)

The finite differences method was used by most of the groups, that addressed the issue of localized surface charging [105, 107, 109]. In that cases it was reasonable, since they all considered trench profiles with straight sidewalls. In terms of finite differences method, the area of interest is represented with a discrete grid of points. In most cases, this grid is rectangular or at least regular [112]. In each grid point, the considered differential equation is converted into a difference equation using the neighbour points and thus, for the entire calculation domain, a system of algebraic equations is created. Taking into account the imposed boundary conditions, the sought approximate solution is obtained by solving the system. Because of the inflexible discretization, FDM can be often inefficient, when handling complicated curvilinear geometries.

The finite element methods (FEM) and spectral methods use same approaches and are closely related [113]. Due to the main approach, the solution of a considered differential equation is written as a sum of certain *basis functions* [112]. After that, the coefficients in that sum are chosen in such a way, that the differential equation is satisfied as well as possible. The group of FEM use basis

functions that are nonzero only on small subdomains [112, 114], while spectral methods utilize basis functions that do not vanish over the whole domain [113]. This is the main difference between these groups of methods, the *local approach* used by FEM [112] and the *global approach* used by spectral methods [113]. While spectral methods are most useful when the geometry of the problem is fairly smooth and regular [113], these methods can face problems when handling complex geometries.

The boundary element method (BEM) can be less consuming regarding computational resources than other methods, including FEM, if there is a small surface/volume ratio in the considered problems [115]. However, for many problems boundary element methods are significantly less efficient than volume-discretisation methods (finite element method, finite difference method, finite volume method). The formulations of BEM usually lead to fully populated matrices [115]. On the contrary, the matrices in finite element methods are typically banded. Therefore, the storage requirements for the system matrices typically grow quite linearly with the problem size. A success-rate in BEM depends heavily on the nature of the problem being solved and the geometry involved.

Each mentioned category of numerical methods has its merits and drawbacks. Surface profiles appearing during the plasma etching simulations by the **VIPER** software often have complicated geometries, especially that arising from simulations of the gas chopping etching process. The simulations can give rise to the variety of forms of the area of interest. Hence for the considered charging simulation model, it was decided to take the finite element method and adjust it according to requirements of the model. FEM is very good in handling of complex geometry, is much versatile in comparison to other discussed methods and demonstrates sufficient numerical stability.

7.5.2.1 The general FEM formulation

Since finite element method has lots of variations, this section will focus on the FEM formulation, required by the model for solving Laplace's differential equation.

Despite the variety of modifications, general principles of finite element method remain unchanged. The main idea of FEM is to approximate the unknown exact function by means of sum of approximation functions.

As a first step, the whole calculation area is divided into subareas (elements), forming a computational mesh. Having a finite size and being described with a finite number of parameters, the subareas have obtained the name *finite elements* [116]. Vertices of the elements are called *nodes*. The choice of element's kind is problem dependent and it often occurs, that for one task several kinds of elements are used. For the developed charging simulation model, it was decided to use triangular elements, since they would provide good fitting of the computational FEM mesh to the curvilinear boundaries in the context of two-dimensional calculations of electric potential distribution.

In our considerations, we will use *the Galerkin's method*, also called *the weighted residual*

method. Except for extremely simple tasks, the FEM yields as a result only an approximated solution, and not the exact one. Let us denote the exact solution with φ_0 , and with φ – the approximated solution ($\varphi \approx \varphi_0$). Recalling Eq. 7.5 and Eq. 7.7, and assuming that the approximated function φ satisfies the initial equation with a certain residual, we obtain for the Laplace's equation:

$$\operatorname{div}(\operatorname{grad} \varphi) = R, \quad (7.20)$$

where R is the residual in comparison to the initial equation.

Due to the mentioned FEM main idea, the exact solution φ_0 should be represented by means of the approximated solution, having the following form [112]:

$$\varphi(x, y, z) = \sum_{k=1}^p N_k(x, y, z) \varphi_k, \quad (7.21)$$

where: p - the total number of nodes, N_k - the chosen and therefore known shape function for the k th node, φ_k - the unknown electric potential value in the k th node.

The form of the shape function can be different (linear, quadratic, etc.) and should be selected before the application of the method. Hence, the value of shape function is known for each node. Substituting Eq. 7.21 into Eq. 7.20 yields

$$\operatorname{div}(\operatorname{grad} \sum_{k=1}^p N_k(x, y, z) \varphi_k) = R \quad (7.22)$$

Assuming the selected shape functions satisfy the boundary conditions for the differential equation, one can determine the p unknown variables φ_k by means of *the method of weighted residuals* [112] using the approach described in Eq. 7.21. The main idea is to minimize the residual in terms of a weighted averaging [112]. Let V be the considered volume where the solution is sought. Obviously, in order to obtain the best approximation, the residual should be reduced to a minimum in each point of the considered volume V . The integral of the residual, weighted with some selected weight functions w , is then required to vanish in V . Using Eq. 7.20, this leads to the following expression:

$$\iiint_V R w \, dV = \iiint_V [\operatorname{div}(\operatorname{grad} \varphi)] w \, dV = 0. \quad (7.23)$$

As already mentioned, it is necessary to select the appropriate kind of shape function to be used in Eq. 7.21. In the majority of cases, linear shape functions (shown in Fig. 7.7) allow to obtain sufficiently good precision of the solution. Unlike the shape functions of greater orders, the linear ones are not so complicated from the viewpoint of implementation in the program code. Therefore, it was decided to use them in the developed charging model and thus in the following discussion, our further considerations will be restricted exclusively to FEM utilizing linear shape functions.

The selected kind of shape functions impose only C_0 continuity and not a slope continuity

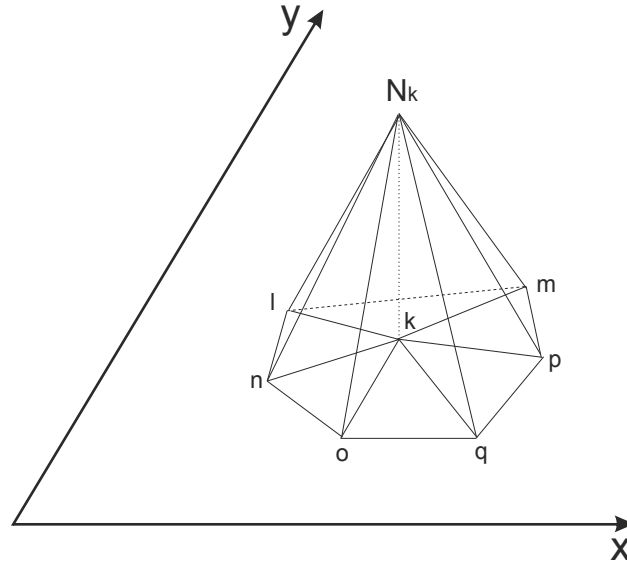


Figure 7.7: Linear shape function $N_k(x, y)$, assigned to k th node of 2D calculation area, defined only on the area of few elements. Picture was taken from [112] and modified.

between elements. Hence, one should get rid of second derivatives in Eq. 7.23. To do that, the *Green's first identity* is used:

$$\iiint_V U_1 \Delta U_2 dV = - \iiint_V \text{grad } U_1 \text{ grad } U_2 dV + \iint_{\partial V} U_1 \text{ grad } U_2 \vec{n} dA, \quad (7.24)$$

where: U_1 and U_2 are any scalar functions, defined on some region V in \mathbb{R}^3 , ∂V is the boundary of region V , and \vec{n} is the outward pointing unit normal of surface element dA . The function U_2 is supposed to be twice continuously differentiable and the function U_1 is once continuously differentiable.

Using the substitution $w = U_1$ and $\varphi = U_2$ and applying the Green's first identity to Eq. 7.23 results in

$$\iiint_V \text{grad } w \text{ grad } \varphi dV = \iint_{\partial V} w \text{ grad } \varphi \vec{n} dA. \quad (7.25)$$

Due to the current concept of the **ViPER** software, the considered charging effect simulation model should allow for only two-dimensional electric field calculations, excluding 3D. Hence, a two-dimensional case of Eq. 7.25 should be used, which yields

$$\iint_A \text{grad } w \text{ grad } \varphi dA = \int_{\Gamma} w \frac{\partial \varphi}{\partial \vec{n}} d\Gamma, \quad (7.26)$$

where A is the considered two-dimensional area, and Γ is the boundary of the area A .

Eq. 7.26 represents a so called *weak formulation* of the considered Laplace's differential equation.

In the Galerkin's method, the weight functions are selected to be equal to the shape functions

[112] used for expanding φ . In the majority of cases, these functions are selected in such a way, that they are defined in a small, including only several finite elements, area of the whole calculation domain A and vanish in the rest area (see example for linear shape functions in Fig. 7.7). Such approach is very useful, if the calculation domain contains subareas with a significant degree of variation of the electric field – a typical case for the calculation domains with complex geometry [112].

The integration over a single i th finite element in Eq. 7.26 yields

$$E^i = \iint_{A_i} \text{grad } w \text{ grad } \varphi \, dA, \quad (7.27)$$

where A_i is the area of the considered i th finite element of the computation domain.

Following the outlined assignment of the weight function $w = N_l(x, y)$ (weight function is set to be equal to the appropriate shape function defined on the l th element), and using the approach from Eq. 7.21, it results for the considered i th finite element:

$$E_l^i = \sum_{k=1}^p \left[\iint_{A_i} \text{grad } N_k \text{ grad } N_l \, dA \right] \varphi_k. \quad (7.28)$$

Using Eq. 7.26, the integration over the entire calculation domain writes as

$$I = \sum_{i=1}^n \sum_{k=1}^p \left[\iint_{A_i} \text{grad } N_k \text{ grad } N_l \, dA \right] \varphi_k = \int_{\Gamma} w \frac{\partial \varphi}{\partial \vec{n}} \, d\Gamma, \quad (7.29)$$

where n is the total number of finite elements in the computation domain and $l = 1 \dots p$.

Due to the FEM approach, Eq. 7.29 is then rewritten in a matrix form, representing a system of p linear equations. To this end, the p weight functions N_l should be used one after another (with $l = 1 \dots p$) in Eq. 7.29 [112]. The resulting system of p linear equations looks as follows:

$$\mathbf{S}\Phi = \mathbf{B}, \quad (7.30)$$

where \mathbf{S} is the coefficient matrix (also often called *stiffness matrix*), and $\Phi = (\varphi_1, \varphi_2, \dots, \varphi_p)$ is the vector of the electric potential node variables, $\mathbf{B} = (b_1, b_2, \dots, b_p)$ is the vector of right hand side values.

Obviously, the product of shape function gradients in Eq. 7.29 will deliver not zero contribution to the stiffness matrix only as long as corresponding shape functions N_k and N_l overlap. Since each shape function is defined only on a very small area, including several finite elements, this leads to a sparsity and diagonal dominance of the coefficient matrix \mathbf{S} , which is useful for effective application of iterative solvers for obtaining solution of the equation system 7.30.

In the considered FEM formulation for the Laplace's differential equation, the right-hand-side

vector \mathbf{B} appears after taking into account the boundary conditions. which are partially represented by the boundary integral in equation 7.26 in its right hand side:

$$I_B = \int_{\Gamma} w \frac{\partial \varphi}{\partial \vec{n}} d\Gamma \quad (7.31)$$

In the developed charging model, one needs to address two types of boundary conditions. The first one, a Dirichlet boundary condition, if imposed on a partial differential equation, specifies the values that the solution should take on the boundary of the calculation domain. The Dirichlet boundary condition, used by the model, is expressed in Eq. 7.9. A Neumann boundary condition is the second considered one. It specifies the values that the derivative of the solution must have on the boundary of the computation domain (the developed model uses expressions in Eq. 7.10 and in Eq. 7.18). Assuming Γ is the whole boundary of the calculation domain, we denote here with Γ_1 and Γ_2 the boundary parts, where correspondingly Dirichlet and Neumann boundary conditions are specified.

Imposing a Dirichlet boundary condition on Γ_1 ($\varphi|_{\Gamma_1} = \bar{\varphi}$) means, that the specified values of electric potential are assigned to appropriate φ_k node values on Γ_1 . The assigned values are then considered in corresponding equations of the equation system (Eq. 7.30), where they are represented as the components of the right-hand-side vector \mathbf{B} . In order to apply the changes to the equation system, the stiffness matrix should be also appropriately modified [114]. In the case of Dirichlet boundary condition, the normal derivative is unknown. Therefore, to avoid the influence of the derivative, the weight function w in Eq. 7.31 is set to 0, forcing the integral I_B to vanish on boundary Γ_1 .

The situation is opposite on boundary part Γ_2 . While there a Neumann boundary condition for the normal derivative of electric potential is imposed ($\frac{\partial \varphi}{\partial \vec{n}}|_{\Gamma_2} = \chi \neq 0$), the electric potential values on Γ_2 are unknown. In that case, the boundary integral I_B (Eq. 7.31) should be taken into account. To do this, the weight function in Eq. 7.31 should be again substituted by the appropriate shape function: $w = N_B(x, y)$. Let us consider a line segment Γ_{2m} between two adjacent nodes of boundary Γ_2 . Assuming N_{B_m} stands for the shape function on the segment and χ_m is the normal derivative value, the fraction of the boundary integral I_B corresponding to this segment can be written as:

$$I_{B_m} = \int_{\Gamma_{2m}} N_{B_m} \chi_m d\Gamma_{2m}. \quad (7.32)$$

Assuming q points from the total number of p points of the calculation area lie on Γ_2 boundary, the following representation for the boundary integral is obtained:

$$I_B = \sum_{m=1}^{q-1} \left[\int_{\Gamma_{2m}} N_{B_m} \chi_m d\Gamma_{2m} \right] \quad (7.33)$$

Each of q boundary points of Γ_2 boundary has an appropriate index in the general set of p

points of the calculation area, which is simultaneously the number of corresponding equation in the equation system 7.30. Hence, taking the boundary integral I_B into account forces changes in equations with appropriate numbers. If the normal derivative is not dependent from other node values, then only the component of the right-hand-side vector is modified. Otherwise, also some coefficients in the stiffness matrix should be corrected.

After solving the equation system 7.30, the approximated value of the unknown function φ_0 can be obtained in any point of the calculation area. This is done by means of interpolation of all node values of the finite element, to which the given point belongs.

Another FEM formulation for the considered task can be developed by means of the Dirichlet principle for Laplace's equation. Due to this principle, any classical solution φ of this problem minimizes the Dirichlet integral:

$$I_v = \iiint_V |\text{grad } \varphi|^2 dV \quad (7.34)$$

In other words, in order to solve the problem, one tries to find a minimizer of the functional I_v , which satisfies the boundary conditions for the Laplace's equation.

In [112, 114], it is shown that this FEM formulation is equivalent to that described in the current section, also resulting in expression represented in Eq. 7.29.

7.5.2.2 The FEM element-related formulation

After we have outlined the general FEM formulation principles for Laplace's equation, we now need to address the formation of the global FEM linear equation system (Eq. 7.30) in more details. Due to the finite element approach, the entire area of interest is divided into sub-domains (finite elements). In the considered electric field calculation model, the node-based finite elements will be utilized, which implies that the sought φ_0 function (exact solution) is expressed by the calculated values of the approximating function φ at finite element nodes. Once the node values of the approximating function φ on a particular finite element are obtained, a value of the φ function can be computed at any point of the element as a linear combination of shape functions weighted by the nodal coefficients. The approximating function for a two-dimensional triangular element e (has 3 nodes) will have the following form:

$$\varphi^e(x, y) = \sum_{i=1}^3 \varphi_i^e N_i^e(x, y), \quad (7.35)$$

where φ_i^e are the approximating function values at the finite element nodes, $N_i^e(x, y)$ are the element shape functions.

Based on the results obtained for each particular finite element, the approximating φ function can be then established for the entire region. During the FEM solution process, the global stiffness matrix \mathbf{S} (Eq. 7.30) is compiled using contributions from each particular finite element. The FEM

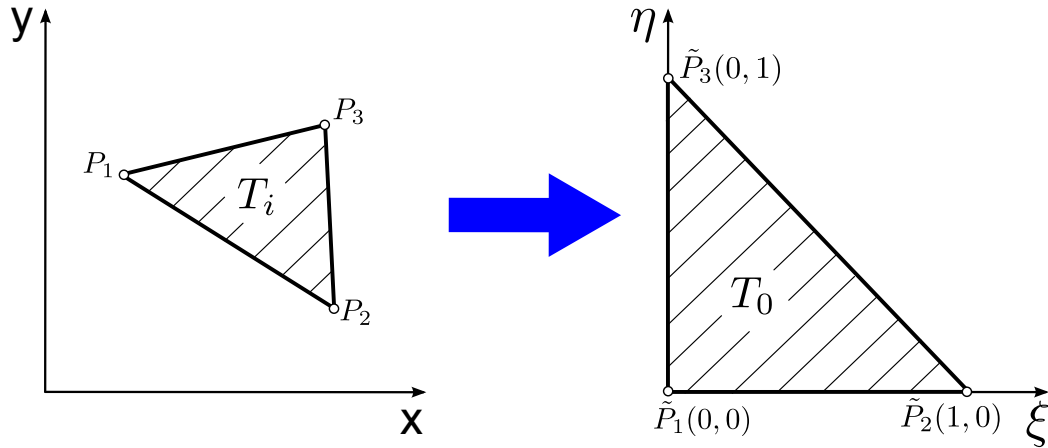


Figure 7.8: Mapping between the considered element T_i and the reference element T_0 by means of linear transformation. Picture taken from [114] and modified.

element-related formulations, used in this work to determine this contributions, will be discussed in the following section.

As a first step, the element shape functions N_i^e should be derived. The shape function $N_i^e(x, y)$ needs to be unity for the i th node and vanish at the two other nodes of the element. This will make Eq. 7.35 valid for any nodal variable φ_i^e . Let T_i be any triangular element of the calculation domain A , and A_{T_i} – the area of T_i . In our considerations, we will allow for the general FEM formulation, based on the minimization of the Dirichlet integral, represented in Eq. 7.34. This implies that to determine the approximating function φ in the entire domain, the following surface integral should be computed over the area of each element T_i [114]:

$$I_{T_i} = \iint_{A_{T_i}} (\varphi_x^2 + \varphi_y^2) dx dy, \quad (7.36)$$

where φ_x and φ_y are the corresponding partial derivatives of the sought approximating function φ with respect to x and y .

Let $P_1(x_1, y_1)$, $P_2(x_2, y_2)$ and $P_3(x_3, y_3)$ be the vertices of the element T_i . They are counter-clockwise consecutive numbered in the element and define its global position in the calculation domain. In order to simplify the calculation of the surface integral I_{T_i} in Eq. 7.36, we introduce a reference triangular finite element, which is an isosceles right triangle T_0 with the cathetus length equal to unity. The mapping of the common element T_i into the reference element T_0 , shown in Fig. 7.8, is realized by means of the linear transformation:

$$\begin{aligned} x &= x_1 + (x_2 - x_1)\xi + (x_3 - x_1)\eta \\ y &= y_1 + (y_2 - y_1)\xi + (y_3 - y_1)\eta. \end{aligned} \quad (7.37)$$

The substitution of variables (Eq. 7.37) helps to convert the surface integral I_{T_i} into a more

simple form [114]. With the help of the so called *Jacobian determinant*

$$J = \begin{vmatrix} \frac{\partial x}{\partial \xi} & \frac{\partial y}{\partial \xi} \\ \frac{\partial x}{\partial \eta} & \frac{\partial y}{\partial \eta} \end{vmatrix} = \begin{vmatrix} (x_2 - x_1) & (y_2 - y_1) \\ (x_3 - x_1) & (y_3 - y_1) \end{vmatrix} = \\ = (x_2 - x_1)(y_3 - y_1) - (x_3 - x_1)(y_2 - y_1), \quad (7.38)$$

one can replace the surface element $dx dy$ [114]:

$$dx dy = J d\xi d\eta. \quad (7.39)$$

According to the chain rule of differentiation, the partial derivatives in the surface integral I_{T_i} (Eq. 7.36) will be represented with the following expressions:

$$\begin{aligned} \varphi_x &= \varphi_\xi \xi_x + \varphi_\eta \eta_x, \\ \varphi_y &= \varphi_\xi \xi_y + \varphi_\eta \eta_y. \end{aligned} \quad (7.40)$$

In order to determine the ξ_x and η_x , both expressions of the linear transformation (Eq. 7.37) are differentiated with respect to x , resulting in

$$\begin{aligned} 1 &= (x_2 - x_1) \xi_x + (x_3 - x_1) \eta_x \\ 0 &= (y_2 - y_1) \xi_x + (y_3 - y_1) \eta_x. \end{aligned} \quad (7.41)$$

Solving this linear equation system with respect to ξ_x and η_x yields the following expressions for the sought variables:

$$\xi_x = \frac{y_3 - y_1}{J}, \quad \eta_x = -\frac{y_2 - y_1}{J}. \quad (7.42)$$

Doing the same, but now differentiating expressions in Eq. 7.37 with respect to y , one determines ξ_y and η_y :

$$\xi_y = -\frac{x_3 - x_1}{J}, \quad \eta_y = \frac{x_2 - x_1}{J}. \quad (7.43)$$

Now using the data of Eq. 7.38, Eq. 7.39, Eq. 7.42, Eq. 7.43 as well as that of Eq. 7.40, the transformation of the surface integral I_{T_i} (Eq. 7.36) into the surface integral over the surface of the reference element T_0 writes as[114]:

$$\begin{aligned} \iint_{A_{T_i}} (\varphi_x^2 + \varphi_y^2) dx dy &= \iint_{A_{T_0}} [(\varphi_\xi \xi_x + \varphi_\eta \eta_x)^2 + (\varphi_\xi \xi_y + \varphi_\eta \eta_y)^2] J d\xi d\eta \\ &= a \iint_{A_{T_0}} \varphi_\xi^2 d\xi d\eta + 2b \iint_{A_{T_0}} \varphi_\xi \varphi_\eta d\xi d\eta + c \iint_{A_{T_0}} \varphi_\eta^2 d\xi d\eta. \end{aligned} \quad (7.44)$$

where the coefficients a , b and c represent the connection to the considered finite element T_i ,

depending exclusively on its geometry:

$$\begin{aligned} a &= [(x_3 - x_1)^2 + (y_3 - y_1)^2] / J \\ b &= -[(x_3 - x_1)(x_2 - x_1) + (y_3 - y_1)(y_2 - y_1)] / J \\ c &= [(x_2 - x_1)^2 + (y_2 - y_1)^2] / J \end{aligned} \quad (7.45)$$

According to Eq. 7.44, the computation of the surface integral over the reference element surface is splitted into the calculation of the three simpler ones:

$$I_{T_0(1)} = \iint_{A_{T_0}} \varphi_\xi^2 \, d\xi \, d\eta \quad (7.46)$$

$$I_{T_0(2)} = 2 \iint_{A_{T_0}} \varphi_\xi \varphi_\eta \, d\xi \, d\eta \quad (7.47)$$

$$I_{T_0(3)} = \iint_{A_{T_0}} \varphi_\eta^2 \, d\xi \, d\eta. \quad (7.48)$$

Being independent of the element geometry, these integrals depend only on the selected type of shape functions, and thus should be calculated only once. In [114], the calculation of these integrals is discussed in details, yielding the following expression as a general form of the evaluation:

$$I_{pq} = \iint_{A_{T_0}} \xi^p \eta^q \, d\xi \, d\eta = \frac{p!q!}{(p+q+2)!} \quad (7.49)$$

As it was defined in section **7.5.2.1: The general FEM formulation**, we use exclusively linear shape functions in our approach. This implies, that for any common element T_i , the approximating function $\varphi(x, y)$ is expressed by means of the expression:

$$\varphi(x, y) = t_1 + t_2x + t_3y. \quad (7.50)$$

Recalling the linear transformation from Eq. 7.37, the approximating function $\varphi(\xi, \eta)$ for the reference element T_0 writes as

$$\varphi(\xi, \eta) = \alpha_1 + \alpha_2\xi + \alpha_3\eta, \quad (7.51)$$

whereas the also needed partial derivatives are as follows:

$$\varphi_\xi = \alpha_2, \quad \varphi_\eta = \alpha_3. \quad (7.52)$$

Using the formula from Eq. 7.49, the computation of the integrals $I_{T_0(1)}$, $I_{T_0(2)}$ and $I_{T_0(3)}$

yields appropriately

$$I_{T_0(1)} = \iint_{A_{T_0}} \varphi_\xi^2 d\xi d\eta = \iint_{A_{T_0}} \alpha_2^2 d\xi d\eta = \frac{1}{2}\alpha_2^2 \quad (7.53)$$

$$I_{T_0(2)} = 2 \iint_{A_{T_0}} \varphi_\xi \varphi_\eta d\xi d\eta = 2 \iint_{A_{T_0}} \alpha_2 \alpha_3 d\xi d\eta = \alpha_2 \alpha_3 \quad (7.54)$$

$$I_{T_0(3)} = \iint_{A_{T_0}} \varphi_\eta^2 d\xi d\eta = \iint_{A_{T_0}} \alpha_3^2 d\xi d\eta = \frac{1}{2}\alpha_3^2. \quad (7.55)$$

Introducing the coefficients vector $\boldsymbol{\alpha} = (\alpha_1, \alpha_2, \alpha_3)^T$, the considered integrals can be rewritten in a matrix form:

$$I_{T_0(i)} = \boldsymbol{\alpha}^T \tilde{\mathbf{S}}_i \boldsymbol{\alpha} \quad i = 1, 2, 3 \quad (7.56)$$

whereas the matrixes $\tilde{\mathbf{S}}_i$ are defined as follows [114]:

$$\tilde{\mathbf{S}}_1 = \frac{1}{2} \begin{bmatrix} 0 & 0 & 0 \\ 0 & 1 & 0 \\ 0 & 0 & 0 \end{bmatrix}, \quad \tilde{\mathbf{S}}_2 = \frac{1}{2} \begin{bmatrix} 0 & 0 & 0 \\ 0 & 0 & 1 \\ 0 & 1 & 0 \end{bmatrix}, \quad \tilde{\mathbf{S}}_3 = \frac{1}{2} \begin{bmatrix} 0 & 0 & 0 \\ 0 & 0 & 0 \\ 0 & 0 & 1 \end{bmatrix}.$$

Using the interpolation condition of the linear approach in the reference triangular unit element, the coefficients α_i can be expressed by the approximating function values at the element vertices, or in other words, by the element node variables represented with the vector $\boldsymbol{\varphi}_e = (\varphi_1, \varphi_2, \varphi_3)^T$:

$$\begin{aligned} \varphi_1 &= \alpha_1 & \alpha_1 &= \varphi_1 \\ \varphi_2 &= \alpha_1 + \alpha_2 & \Rightarrow & \alpha_2 = -\varphi_1 + \varphi_2 \\ \varphi_3 &= \alpha_1 + \alpha_3 & & \alpha_3 = -\varphi_1 + \varphi_3, \end{aligned} \quad (7.57)$$

whereas the matrix \mathbf{A} , governing the transformation, writes as

$$\mathbf{A} = \begin{bmatrix} 1 & 0 & 0 \\ -1 & 1 & 0 \\ -1 & 0 & 1 \end{bmatrix}. \quad (7.58)$$

Taking into account the transformation represented in Eq. 7.57, the shape functions for the reference element can be now formulated as follows:

$$\begin{aligned} N_1(\xi, \eta) &= 1 - \xi - \eta \\ N_2(\xi, \eta) &= \xi \\ N_3(\xi, \eta) &= \eta. \end{aligned} \quad (7.59)$$

The derivation of the shape functions is discussed in details in [114].

After writing the considered relation in a matrix form

$$\alpha = \mathbf{A}\varphi_e, \quad (7.60)$$

and using it as a substitution, we can express the considered integrals $I_{T_0(i)}$ employing the element node variables:

$$I_{T_0(i)} = \varphi_e^T \mathbf{A}^T \tilde{\mathbf{S}}_i \mathbf{A} \varphi_e = \varphi_e^T \mathbf{S}_i \varphi_e \quad i = 1, 2, 3. \quad (7.61)$$

whereas the \mathbf{S}_i matrixes in Eq. 7.61 are defined as follows:

$$\mathbf{S}_1 = \frac{1}{2} \begin{bmatrix} 1 & -1 & 0 \\ -1 & 1 & 0 \\ 0 & 0 & 0 \end{bmatrix}, \quad \mathbf{S}_2 = \frac{1}{2} \begin{bmatrix} 2 & -1 & -1 \\ -1 & 0 & 1 \\ -1 & 1 & 0 \end{bmatrix}, \quad \mathbf{S}_3 = \frac{1}{2} \begin{bmatrix} 1 & 0 & -1 \\ 0 & 0 & 0 \\ -1 & 0 & 1 \end{bmatrix}. \quad (7.62)$$

Let \mathbf{S}_e be the element stiffness matrix for the considered triangular element T_i . Taking into account coefficients a , b and c from Eq. 7.45, matrix \mathbf{S}_e writes as a linear combination of matrixes \mathbf{S}_1 , \mathbf{S}_2 and \mathbf{S}_3 :

$$\mathbf{S}_e = a\mathbf{S}_1 + b\mathbf{S}_2 + c\mathbf{S}_3. \quad (7.63)$$

The final goal of our considerations – the contribution of the integral $\iint_{A_{T_i}} (\varphi_x^2 + \varphi_y^2) dx dy$ for the considered finite element T_i – can be now expressed using Eq. 7.61 and Eq. 7.63:

$$I_{T_i} = \iint_{A_{T_i}} (\varphi_x^2 + \varphi_y^2) dx dy = \varphi_e^T \mathbf{S}_e \varphi_e \quad (7.64)$$

7.5.2.3 Compilation of the FEM equation system

In previous section, the element stiffness matrix \mathbf{S}_e has been derived, which expresses the contribution of a particular finite element T_i to the approximating function $\varphi(x, y)$ in the entire region of interest. Due to the utilization of triangular elements and piecewise linear polynomials, each finite element consists of three nodes. Therefore, each local stiffness matrix \mathbf{S}_e is a 3×3 matrix (is obtained by the combination of Eq. 7.62 and Eq. 7.63). After the element stiffness matrices are computed for each single finite element, their contributions are added to the global stiffness matrix \mathbf{S} . Each node of the global computation domain is represented by a particular equation in the FEM linear equation system, shown in Eq. 7.30. Thus, each row of the global stiffness matrix \mathbf{S} contains the information about the appropriate node, to which it is related. A particular node of the FEM computation domain belongs simultaneously to several adjacent finite elements, being taken into account in the appropriate element stiffness matrices of these elements. Hence during the global stiffness matrix \mathbf{S} assembly process, the \mathbf{S} matrix row corresponding to the considered node is created by a superposition of the appropriate local stiffness matrices \mathbf{S}_e contributions from the elements, the considered node belongs to. The same is done for the rest of the nodes, thus implementing the global stiffness matrix compilation process. More detailed, the process of the

global stiffness matrix assembly is described in [114].

As already mentioned in section **7.5.2.1: The general FEM formulation**, the right-hand-side vector \mathbf{B} (FEM linear equation system in Eq. 7.30) is formed due to consideration of the boundary conditions. The developed model utilizes Dirichlet and Neumann boundary conditions.

If a Dirichlet boundary condition is imposed for a particular node (i.e. having the global index k) of the calculation domain boundary part Γ_1 ($\varphi|_{\Gamma_1} = \bar{\varphi}$), some changes should be made to the corresponding k th equation of the FEM linear equation system. Namely, appropriate k th component of the right-hand-side vector is assigned the value $\bar{\varphi}$ followed by a subsequent modification of the global stiffness matrix (also described in [114]). In the case, the assigned value is zero ($\bar{\varphi} = 0$), the only change to be made is setting all global stiffness matrix components of the k th row and column to zero, except of the diagonal component s_{kk} , which is set to unity. Otherwise if $\bar{\varphi} \neq 0$, and assuming i is the index of any of the rest equations, before doing the outlined operations, the value $s_{ik} \cdot \bar{\varphi}$ should be subtracted from the corresponding right-hand-side b_i th component in each of the rest equations[114].

In the developed model, a Neumann boundary condition implements the influence of the surface charging on the entire system, thus playing a very important role. When this type of boundary conditions is imposed for a particular node lying on the Γ_2 boundary part of the calculation domain, the boundary integral shown in Eq. 7.31 should be taken into account. The given normal derivative value $\frac{\partial \varphi}{\partial n}$ is used to define the right-hand-side in the equation corresponding to the given node. Interpretation of this integral in the context of the considered charging simulation model is not a trivial task. Therefore, it will be addressed separately in more details.

7.5.2.4 Consideration of the boundary integral

The evaluation of the boundary integral from Eq. 7.31 was already shortly discussed in section **7.5.2.1: The general FEM formulation**. The current section continues the discussion, addressing particular details of the model implementation regarding the FEM linear equation system assembly with the consideration of Neumann boundary conditions.

Like in previous sections, Γ_2 stands for the part of the entire domain boundary Γ with an imposed Neumann boundary condition. Due to the FEM discretisation, Γ_2 is the set of boundary segments, connecting the Γ_2 boundary nodes. After selecting linear shape functions, the boundary integral from Eq. 7.31 can be represented as a sum (Eq. 7.33), where each summand is an integral over the appropriate boundary segment. In the following discussion, considerations will be restricted to the boundary integral over a single segment of Γ_2 boundary. Once one such integral is evaluated, the same is valid for the rest of the sum. Let S_b be the considered boundary segment of Γ_2 , having the length of L_s . The boundary nodes B_1 and B_2 are the endpoints of S_b . Due to the concept selected for the charging model implementation, the orientation of boundary segments is unambiguously defined. Furthermore, charge density value for the surface segment is kept constant along its entire length, being saved in the beginning point, which for S_b is the boundary node B_1 . Hence, the final goal of the considered integral evaluation is to modify the FEM equation

system according to Neumann boundary condition imposed in the boundary node B_1 . The normal derivative value $\frac{\partial\varphi}{\partial\vec{n}}|_{B_1} = \chi$ at the boundary node B_1 is valid for the entire segment:

$$\frac{\partial\varphi}{\partial\vec{n}}|_{S_b} = \chi \quad (7.65)$$

N_{B_m} stands for the shape function on the m th boundary segment. Then the boundary integral for the segment S_b is expressed as follows:

$$I_{S_b} = \int_{S_b} N_{B_m} \chi \, dS_b. \quad (7.66)$$

The normal derivative is constant over the entire segment. Hence, it can be taken out of the integral, yielding

$$I_{S_b} = \chi \int_{S_b} N_{B_m} \, dS_b. \quad (7.67)$$

Now in order to evaluate the resulting integral, the shape function on the boundary segment should be considered in more details. Let T_i be the finite element with the vertices B_1 , B_2 and B_3 , where the triangle edge between B_1 and B_2 represents the considered boundary line segment S_b . Due to the selected FEM concept, each finite element has 3 vertices and there are also three different linear shape functions defined on the element. Such linear shape function is unity at the element node, to which it belongs. Decreasing linearly over the element area, it vanishes in the rest two nodes. For further considerations, let us define shape functions N_1 , N_2 and N_3 , which appropriately belong to B_1 , B_2 and B_3 nodes of the element T_i . The sought shape function N_{B_m} will be a superposition of the N_1 , N_2 and N_3 functions on the boundary segment S_b . The behaviour of the considered shape functions on segment S_b is shown in Fig. 7.9. N_3 shape function belongs to B_3 node, which lies outside the boundary segment. Hence, N_3 is equal to zero along the entire S_b length. Being unity in the opposite nodes of the boundary segment, N_1 and N_2 are linearly decreasing along its length and vanish correspondingly in B_2 and B_1 element nodes. Both shape functions demonstrate the same behaviour along S_b , thus both boundary nodes yield equal contributions to boundary integral I_{S_b} , allowing to express it as a sum of two more simple summands:

$$I_{S_b} = \chi \left[\int_{S_b} N_1 \, dS_b + \int_{S_b} N_2 \, dS_b \right]. \quad (7.68)$$

Integral I_{S_b} is in a direct proportion to boundary segment length L_s . Considering the case when $L_s = 1.0$, evaluation of the partly contributions to boundary integral I_{S_b} from boundary nodes B_1 and B_2 is evident, resulting in

$$I_{S_{b1}} = \chi \int_{S_b} N_1 \, dS_b = 0.5\chi, \quad I_{S_{b2}} = \chi \int_{S_b} N_2 \, dS_b = 0.5\chi. \quad (7.69)$$

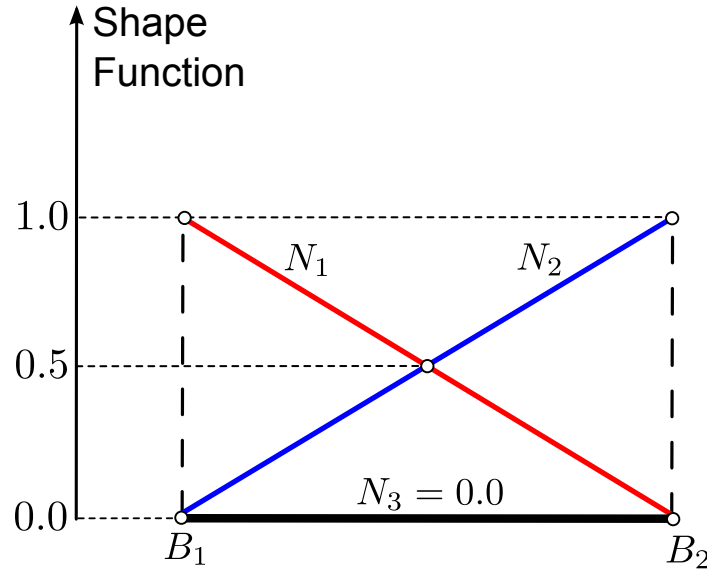


Figure 7.9: Behaviour of linear shape functions on the boundary of the considered triangular finite element T_i with vertices B_1 , B_2 and B_3 . The considered boundary segment has element nodes B_1 and B_2 as endpoints.

Finally, we generalize the derived approach. Let B_m be any particular boundary node, and S_{bm} is one of the boundary segments, having B_m as the considered endpoint. L_{sm} stands for the segment length. Now, the contribution of B_m to the Neumann boundary condition formulation with respect to S_{bm} can be written as follows:

$$\boxed{I_{S_{bm}} = 0.5\chi L_{sm}}. \quad (7.70)$$

In the developed charging model, normal derivative value χ is obtained either from Eq. 7.18 or from Eq. 7.19. If electric fields in insulating materials of the sample should be also taken into account, the normal component E_{n2} of the electric intensity vector in the second media does not vanish (Eq. 7.19), yielding two unknown variables in one equation. The solution for this issue was derived in terms of development of the considered charging simulation model, and is discussed separately in Appendix A: *Neumann boundary condition between two insulators*.

7.5.2.5 Meshing

According to the generic FEM process, the calculation domain must be divided into elements. In the context of the developed charging simulation model, the most straightforward example of the area of interest is the space near the sample and between the etched features (see Fig. 7.4). In this case, the calculation domain represents only one medium. The possibility to take electric field into account also in the insulating materials of the sample, sets additional requirement for an FEM meshing module. Namely, subareas of the domain of interest, representing different materials, should be quantized into elements in such a way that they fit together as parts of the entire calculation mesh – adjacent subareas must have coinciding nodes along the whole mutual boundary. Therefore, the

electric field calculation module requires a high quality FEM mesh generator which is capable of creating such kind of meshes.

In terms of the model development, it was decided to employ the program code of **Triangle** – a two-dimensional quality mesh generator and Delaunay triangulator [117]. The **Triangle** mesh generator is very time efficient while producing high quality meshes. Hence, it was included into the **ViPER** simulator as a part of the charging simulation model. One of the advantages of the **Triangle** mesh generator is an adaptive meshing algorithm – which produces smaller and more finite elements in the vicinity of the curved parts of the sample surface, whereas the larger elements, on the contrary, are generated on a certain distance from the sample surface. This reduces significantly the computation time.

Depending on whether the insulating materials of the sample are considered in the electric field calculations, the model can use two possible ways of computational area meshing, shown in Fig. 7.10.

Electric field calculation in the insulating materials can often require setting additional boundary conditions for the computation domain. In some cases, this can lead to significant changes of the electric potential distribution in the area of interest. One of such examples is shown in Fig. 7.11. It demonstrates resulting electric potential distribution calculated by the developed model for typical surface charging of the etched features – positively charged surface at the bottom of the trench and negatively charged surface of the mask. During the calculations, both approaches were used. Result in Fig. 7.11(a) was obtained by considering electric field only in the gas-phase at the microstructure area, yielding strong positive potential in the etched trench due to the positive charging at the trench bottom. In Fig. 7.11(b), insulators (mask and underlying oxide) were also taken into account, where an additional Dirichlet boundary condition was set at the bottom of the underlying oxide layer ($\varphi = 0$). Because of the relatively small thickness of the oxide layer, this resulted in a significant reduction of the positive electric potential at the trench bottom.

Therefore, the additional boundary conditions should be selected with a particular care, taking into account all peculiarities of each considered case. On the one hand, this can sometimes make the formulation of the charging simulation task much more complicated, thus limiting versatility of the model. Hence, while using the developed charging effect simulation model, the consideration of electric field in insulating materials of the sample should be utilized only in cases when it really makes sense. On the other hand, utilization of the approach can be very helpful while addressing directly the problem regarding the influence of insulating materials of the sample on the arising local electric fields. Thereby, the developed charging model can be used to estimate the influence of either different mask configurations or oxide layer thickness on the surface profile evolution.

7.6 Particle trajectories calculation

As mentioned in section 7.3: *General structure of the developed charging model*, the transport of charged particles from the lower sheath boundary to the sample, considering the local electric

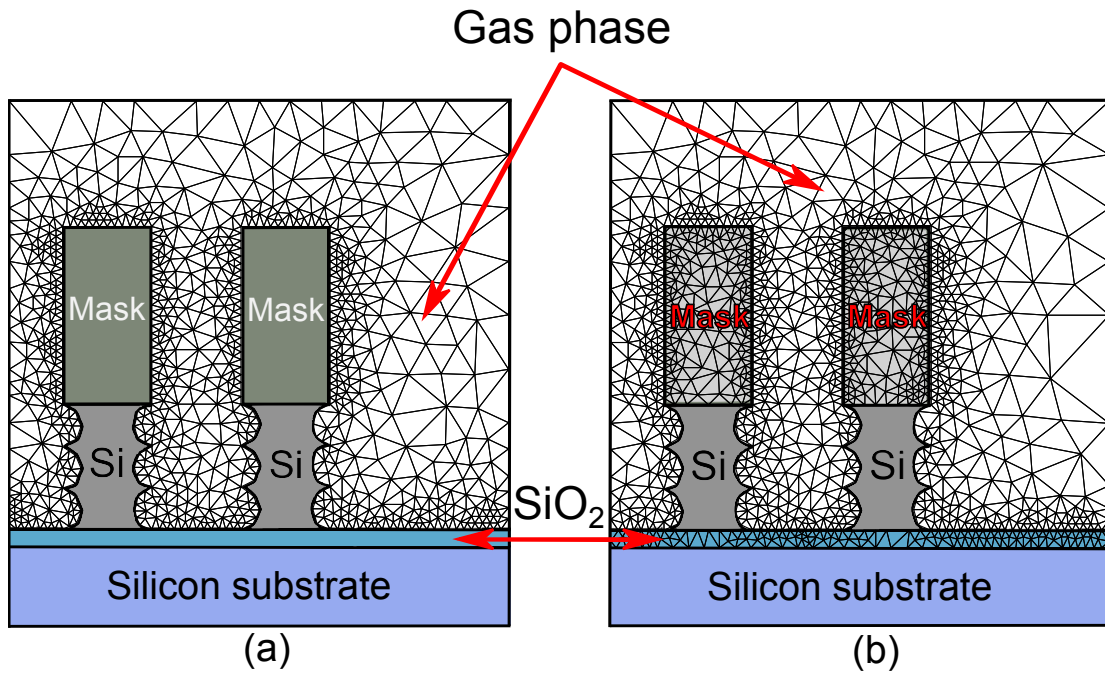


Figure 7.10: Two ways of meshing of the charging simulation area. (a): Computational mesh covers only the gas-phase area (other media are not considered in the electric field calculations). (b): Computational mesh is built with a consideration of the insulating materials of the sample (photo-resist mask, underlying oxide layer). Picture taken from [1] and modified.

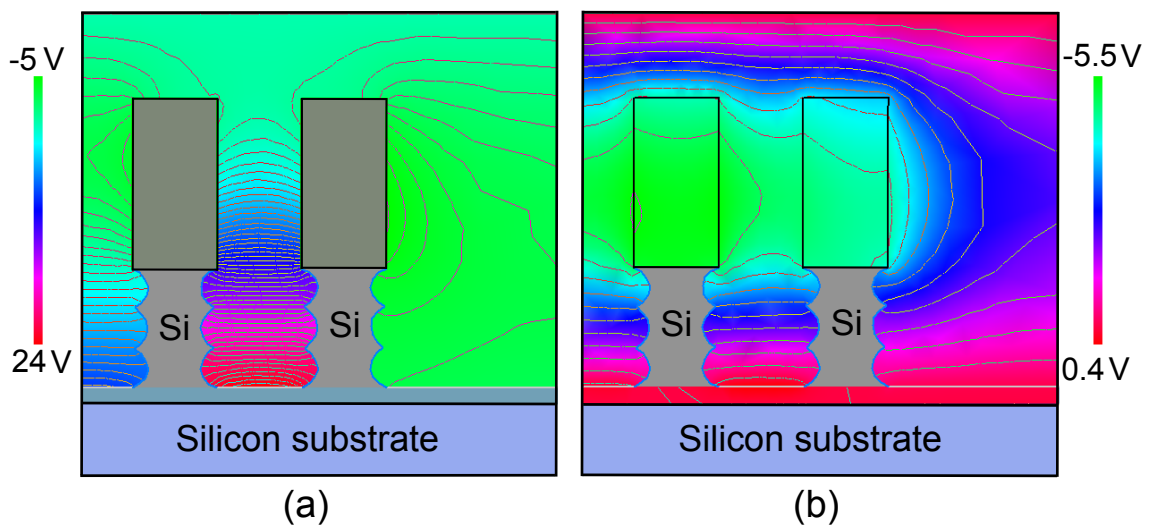


Figure 7.11: Electric potential distribution calculated by the developed model for typical surface charge distribution during dry silicon etching for SOI wafers. (a): Calculation without taking insulating materials of the sample into account. (b): Insulating materials of the sample are also considered in the calculation (additional Dirichlet boundary condition – the value of electric potential was set to 0 at the bottom of the underlying oxide layer – has significantly reduced the positive potential at the bottom of the etched trenches).

fields, is the second of the two main parts of the developed charging model.

For the particle motion calculations, it was decided to use a Monte Carlo (MC) method. The method implies generation of a given number of virtual particles ¹ (here and in further considerations – *a MC particle*) for positive ions and electrons on the lower sheath boundary with a subsequent tracking of their trajectories through the simulation area until they reach the surface of the sample.

During the generation, the initial velocity vector for each MC particle is obtained by randomly sampling the appropriate angle and energy distribution functions, that were earlier calculated for each species by the sheath transport model. The simulated transport expresses one step (*a charging step*) of the charging simulation loop (see general structure of the model in Fig. 7.3), which corresponds to the total current of positive ions and electrons during one-half *rf* cycle in the plasma sheath (the approach was also used by Hwang and Giapis [105]). Due to the assumptions to the model, made in section 7.5: *Electric field calculation module*, the electrons and the positive ions are considered to have equal and temporarily invariant fluxes on the lower sheath boundary. Usually, the model uses 600 MC particles for the positively charged ions as well as for the electrons, in order to simulate their currents during one single charging step. For the tasks, where the number of MC particles is not enough to obtain sufficient calculation precision, it can be increased by user in order to enhance quality of the simulation.

Trajectory of each MC particle should be simulated in the area of interest. To do this, the model employs the second Newton law and considers the equation of motion for each simulation particle:

$$m\vec{a} = \vec{F}, \quad (7.71)$$

where m is the particle mass, \vec{a} is the particle acceleration and \vec{F} is the sum of all forces, acting on the particle. In our case, the particle, that was already accelerated in the sheath area, is near the sample only affected by the electric force field, induced by the local surface charging.

Hence, Eq. 7.71 can be rewritten as

$$m\vec{a} = q\vec{E}(x, y), \quad (7.72)$$

where q is the charge of the particle, and $\vec{E}(x, y)$ is the electric intensity vector value in the current location (x, y) of the particle.

With respect to the particle coordinates for the current given moment of time the particle equation of motion is

$$m \frac{\partial^2 x}{\partial t^2} = qE_x, \quad (7.73)$$

$$m \frac{\partial^2 y}{\partial t^2} = qE_y. \quad (7.74)$$

In order to calculate the MC particle trajectory, Eq. 7.73 and 7.74 should be two times integrated

¹one simulated particle can represent more than one real ion or electron

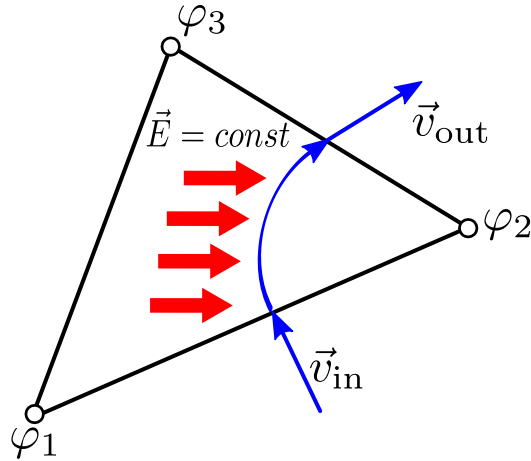


Figure 7.12: Particle moves over the area of a triangular finite element and is affected by the homogeneous electric field. φ_1 , φ_2 and φ_3 – the calculated node values of electric potential, \vec{E} is the homogeneous electric field for the current finite element, \vec{v}_{in} – the particle velocity as it flies into the finite element area, \vec{v}_{out} – the particle velocity after it leaves the area of the finite element.

over the time of the entire particle flight. The integration is mostly implemented numerically, using in the majority of cases Euler method, leapfrog integration or one of the Runge-Kutta methods. For instance, Arnold et al. [107] used fourth-order Runge-Kutta integration in their charging model. In general, the utilization of such methods would imply, that on each integration step, one should know the electric intensity value in the corresponding point of the calculation domain. To do this, the appropriate finite element containing the considered point should be also determined on each integration step. The constant search for the needed finite element can be very time consuming, in particular in the case of a fine mesh.

Therefore in the context of the model, it was decided to use the mesh created by the FEM electric field calculation module, and to determine the particle trajectory over each finite element analytically. The implemented FEM uses *linear* shape functions. As follows from the linear approach, the electric intensity vector is constant on each triangular element (see Fig. 7.12). Of course, in this case, in order to keep the needed accuracy of the electric field calculation, the generated mesh should be fine enough.

The components of the particle acceleration vector are

$$\vec{a}_x = \frac{qE_x}{m} \quad (7.75)$$

$$\vec{a}_y = \frac{qE_y}{m} \quad (7.76)$$

After the integration of both, Eq. 7.75 and Eq. 7.76 over the time, one obtains the particle's velocity on the current finite element

$$v_x = \frac{qE_x}{m}t + v_{0x}, \quad (7.77)$$

$$v_y = \frac{qE_y}{m}t + v_{0y}, \quad (7.78)$$

where v_{0x} and v_{0y} are the components of the initial particle velocity on the current element, which is denoted as \vec{v}_{in} in Fig 7.12.

Integrating the obtained equations Eq. 7.77 and Eq. 7.78 over the time, one gets the expression of the particle trajectory:

$$x = \frac{qE_x}{m}t^2 + v_{0x}t + x_0, \quad (7.79)$$

$$y = \frac{qE_y}{m}t^2 + v_{0y}t + y_0, \quad (7.80)$$

where (x_0, y_0) is the initial position of the particle.

This represents particle's trajectory with the charge q and mass m , in the homogeneous field \vec{E} . For each next finite element, the simulated particle flies in, the data about the particle initial position (x_0, y_0) and the particle initial velocity (v_{x0}, v_{y0}) are already known. In this case, only the intersection point of the described trajectory with one of the finite element sides needs to be found. This determines the place, where the simulated particle leaves the current finite element. For this purpose, each triangular element side with endpoints (x_1, y_1) and (x_2, y_2) is represented in a parametric form:

$$x = x_1 + \alpha(x_2 - x_1) \quad (7.81)$$

$$y = y_1 + \alpha(y_2 - y_1) \quad (7.82)$$

After the searched intersection point is calculated, it is determined, to which adjacent finite element it belongs and the calculation continues using the initial position and the velocity information from the previous element. In such a way the simulated particle is traced through the whole area of interest, until it leaves the simulation area, or impacts the sample surface. Since it was decided to use the mirror simulation images, the trajectories of the particles, that leave the simulation area and cross the leftmost or the rightmost vertical boundaries, are mirrored with respect to the Y axis. That is, the tracking of the simulated particle continues, but the sign of the v_x velocity component is changed to the opposite.

Each simulation particle carries some amount of physical electric charge. In the model, it is considered that such particle, impinging on the feature profile surface, leaves its charge there with 100 % probability. Hence, each such impact changes the local surface charging and makes contribution to the electric field of the entire simulation area.

7.7 Results. Application of the implemented charging model

For the validation of the developed charging simulation model, it was necessary to test the model with a real plasma etching experiment showing evident influence of the surface charging, and to compare the both resulting profiles. The experiment, provided by Oxford Instruments Plasma Technology, is a good demonstration of the notching effect (see Fig.7.13). In the context of the

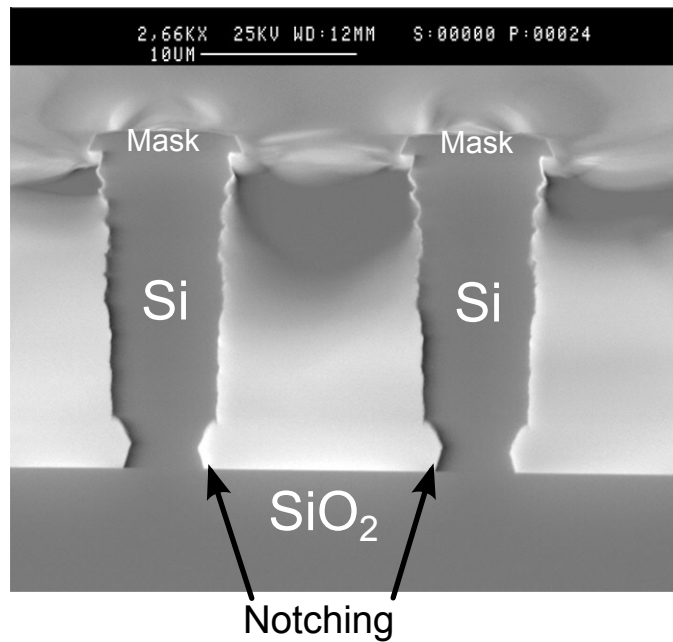


Figure 7.13: Experimental results from Oxford Instruments Plasma Technology. Etching of silicon layer on a SOI wafer using gas chopping process. The significant positive potential at the trench bottom, induced by the positive charge buildup on the underlying oxide layer during the overetching step, accounts for the pronounced notching effect. Picture taken from [1] and modified.

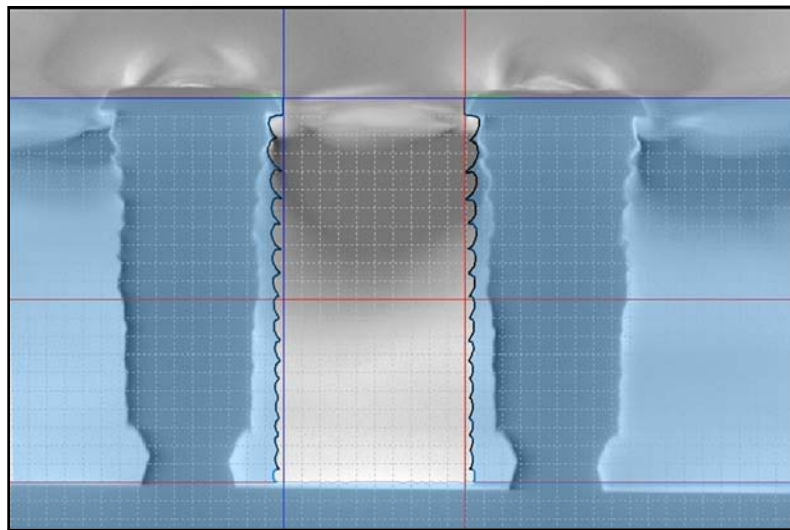


Figure 7.14: Simulated surface profile without utilization of the implemented charging effect simulation model. Sidewalls are vertical, without any tilt. No notching effect considered. Picture taken from [1].

experiment, 10 μm trenches were etched in SOI wafer by means of a gas chopping process in an inductively coupled plasma (ICP) system, using SF_6 and C_4F_8 plasmas. The mask thickness was 1.5 μm . In order to demonstrate the importance of the implemented model, the experiment was first simulated without including the developed charging effect simulation model.

The resulting surface profile shown in Fig. 7.14 presents vertical sidewalls with ripples, peculiar to the gas chopping etching process. The simulated profile does not demonstrate any notching effect

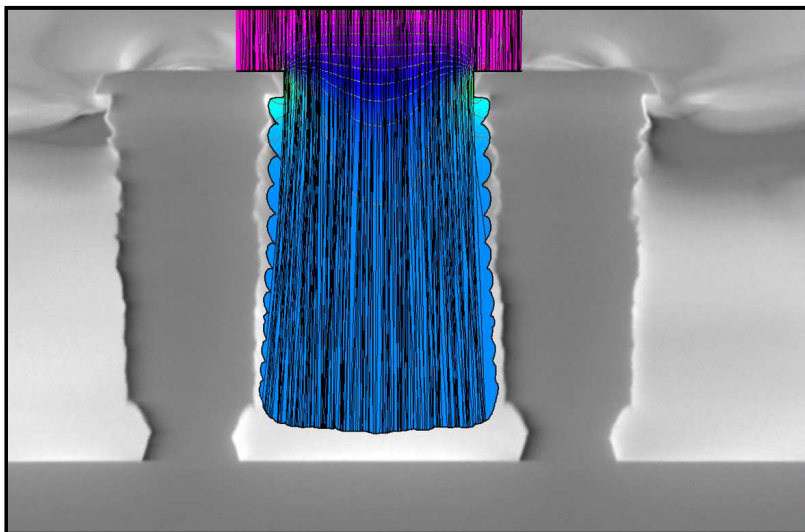


Figure 7.15: *Simulated intermediate surface profile with utilization of the implemented charging effect simulation model. Sidewalls are tilted due to the bending of the positive ion trajectories. Picture taken from [1].*

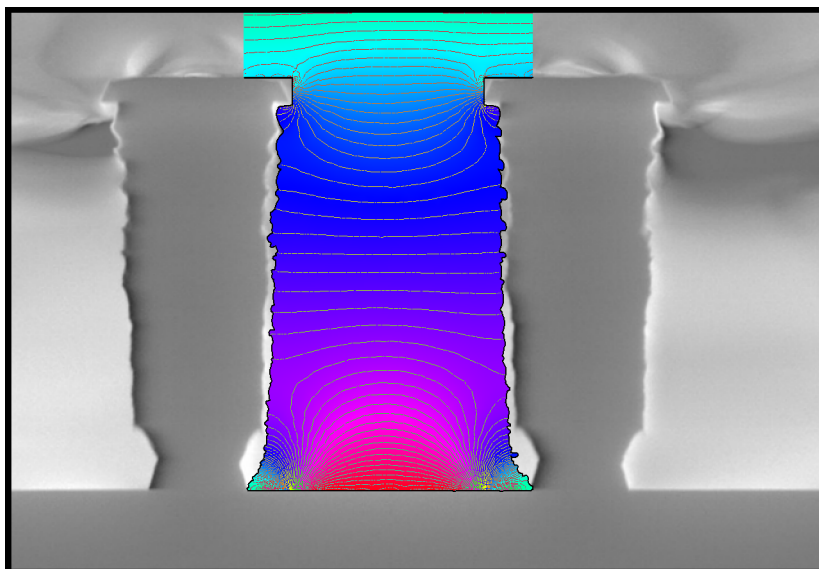


Figure 7.16: *Electric potential distribution in the area of interest at the final stage of the profile simulation. Maximal value of positive electric potential in the middle of the trench bottom is around 25 V. Picture taken from [1].*

at all.

For the charging simulation model, it was decided to do a general validation, neglecting electric fields in the insulating materials of the sample, thus using only the boundary conditions derived in section **7.5.1: Definition of the boundary conditions**. After the charging effect model was included into the simulation, a different result was obtained. One of the differences was a buildup of a negative electric potential in the upper part of the trench due to the negative mask surface

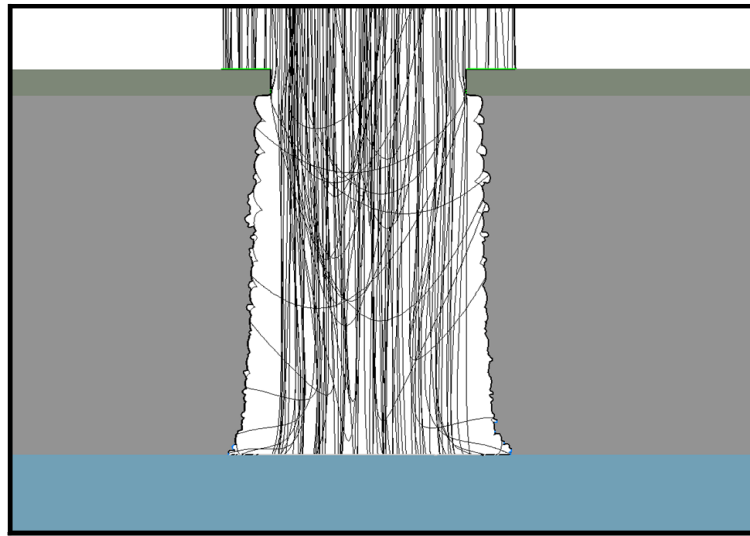


Figure 7.17: Trajectories of positive ions during the simulation. Strong positive potential at the bottom of the trench causes deflection of the low energetic ions to the sidewalls leading to the lateral etching and appearance of notching. Picture taken from [1].

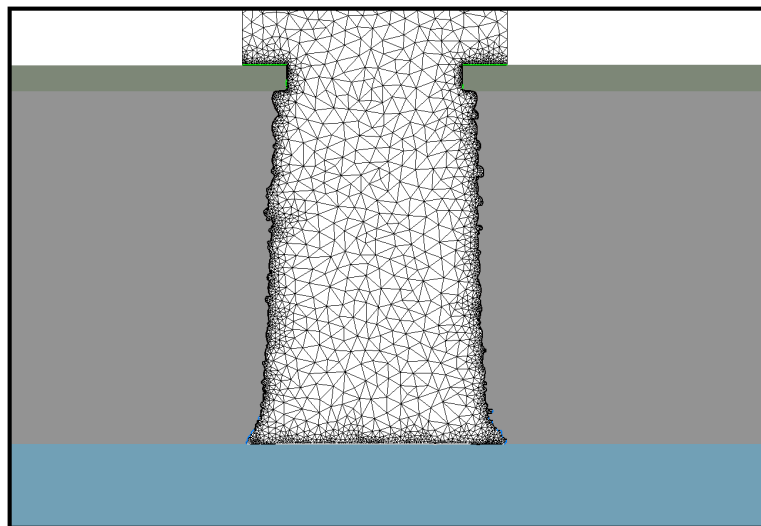


Figure 7.18: Meshing by the FEM solver.

charging. As the insulating material in the upper part of the trench starts to charge up negatively, with the progress of the etching simulation this negative potential becomes high enough (around -4 V) to cause a slight trajectory bending of the positively charged ions, and they are attracted more and more away from the initial direction. This leads to the etching also in a lateral direction, that is, the profile loses its anisotropy and the sidewalls obtain a certain slope (see Fig. 7.15). In the considered case of SOI wafer, the etch floor is probably clear of insulator until reaching the buried oxide. Charge reaching the floor probably can flow away to wafer regions where there are open unpatterned areas (normally scribe lines). After silicon layer was etched down to the underlying oxide, the exposed insulating surface in the bottom of the trench started charging up positively. As more and more silicon is etched away, more oxide surface is being exposed and becomes available for charging, which significantly increases positive potential value in the entire

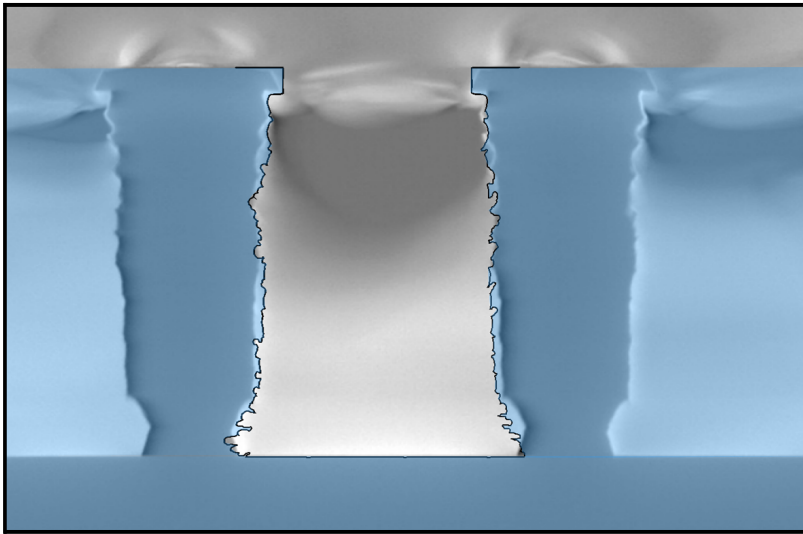


Figure 7.19: *Resulting surface profile after utilization of the implemented charging effect simulation model. Ripples on the sidewalls surface, peculiar to the gas chopping process, were eroded because of the deflection of the low-energetic positively charged ions away from the trench bottom. Picture taken from [1].*

simulation area. At some point of profile evolution, the positive electric potential at the trench bottom becomes strong enough, to reflect the low energetic positively charged ions to the sidewalls (see Fig. 7.17), which leads to further lateral etching there, whereas the rippled form of the sidewalls is destroyed. Simultaneously, further exposition of the oxide surface leads to a growing positive surface charging of the trench bottom, causing strong lateral etching at the silicon-oxide interface, and, thus, the notching evolution. At the final stage of the simulation, the FEM mesh, generated by the electric field calculation module, is already very complicated in order to address all peculiarities of the surface profile and yield desired quality of the simulation (see Fig. 7.18). Electric potential distribution shown in the Fig. 7.16 clearly illustrates the dipole electric field in the area of interest. Final result of the simulation (shown in Fig. 7.19) is in a good agreement with the experimental data.

7.8 Conclusions to the developed charging model

In the context of this work, a new charging effect simulation model was developed and implemented within the **ViPER** plasma processing simulation software. It should be noted, that the implemented simulation model is able to capture the phenomena caused by the local surface charging effect. By comparing obtained simulation to experimental profiles provided by Oxford Instruments Plasma Technology, it was shown that the model can capture well the notching and bowing effects and yield plausible results. Furthermore, in contrast to the previously published results, here the model demonstrates the impact of the charging effect over the entire course of the etching process and therefore, it gives much more insight into the surface profile evolution dynamics. Regarding the considered validation experiment, the model has shown how the resulting profile appeared, namely by the etching of the profile ripples on the sidewalls during the overetching. In addition, the

implemented charging effect model is able to consider electric field in the insulating materials of the sample and can be used to estimate the influence of either different mask configurations or oxide layer thickness on the surface profile evolution. The author of this work believes, that further utilization of the model in the **ViPER** simulator gives great possibility to understand large number of secondary effects and learn how to prevent them, concerning not only plasma etching, but also plasma deposition processes.

Chapter 8

Simulations of cryogenic silicon etching

As follows from the discussion in section 4.6: *Cryogenic etching of silicon*, a cryogenic SF₆/O₂ etch process shows great promise in terms of silicon nanopatterning. For a high quality profile control at the nanoscale, one needs a deeper insight into the physical and chemical phenomena occurring during the processing. Therefore, a lot of workgroups across the globe have been investigating the process by conducting numerous experiments. For instance, Boufnichel *et al.* studied mechanisms responsible for local bowing effect [118, 119] and also did research on origin, control and elimination of undercut in silicon deep plasma etching in the cryogenic process [120]. The group of Craciun *et al.* investigated experimentally the temperature influence on etching deep holes with SF₆/O₂ cryogenic plasma [121], identifying the aspect ratio dependent etching as a serious limitation for the required homogeneity in etched depth. Bakhtazad *et al.* investigated how various process parameters influence Si etching on SOI platform [122], reporting different results with respect to that of bulk silicon cryogenic etching. Inductively coupled plasma (ICP) cryogenic dry etching was examined by Sökmen *et al.* in the fabrication of different microstructures: pores, nano contact lines, submicron diameter pillars, deep anisotropic structures, membrane structures, thin and thick cantilevers [123]. A thorough study conducted by Gomez *et al.* [124] indicates the F-to-ion flux ratio and F-to-O flux ratio as important plasma parameters, determining the etch rate and anisotropy.

The research group of the Nanofabrication facility at Molecular Foundry, Lawrence Berkeley National Laboratory (LBNL) does research on super-selective cryogenic etching for sub-10 nm features in silicon. Their recent works [13, 14] showed the feasibility of the cryoetch process for silicon nanopatterning with linewidths down to 10 nm. Despite the utilization of soft masks, the selectivity of 10:1 was still achieved, implying that traditionally used hard masks could be replaced, thus avoiding additional costly steps. However, in addition to already known and partly investigated critical phenomena of plasma etching, some new significant challenges arise with further shrinking feature sizes. With critical dimensions of several nanometers, the surface roughness becomes a crucial issue for profile control while striving to obtain high aspect ratio anisotropic structures. In cryogenic etching, the dependence of the etch rate on feature aspect ratio can be quite significant. With small features, higher aspect ratios are reached very quickly into the etch and thus must be

considered. Furthermore, at the nanoscale, profile angles are found to change dramatically with feature size, even in the early stages of etching[13].

Thus, a much more deep understanding of the process is required to allow sub-10 nm features etching and the mentioned issues make simulation invaluable in understanding how to control profile. This has become a reason for the cooperation between the *Nanofabrication facility* at Lawrence Berkeley National Laboratory and the *Department of Micro- and Nanoelectronic Systems* at Ilmenau University of Technology. The aim of the cooperation was to employ the **ViPER** simulator in terms of the silicon cryoetching experiments conducted at LBNL. In the context of the current work, it was necessary to develop a cryoetching simulation model within the **ViPER** software and to calibrate it with respect to the plasma etch hardware installed at LBNL, for better understanding of already conducted experiments as well as for further development of the process. To this end, the author of the work has spent 6 months at the Lawrence Berkeley National Laboratory, conducting appropriate experiments on the considered cryogenic plasma processing equipment as well as having fruitful discussions in terms of the model development.

8.1 Experiments

A hardware configuration used for cryogenic processing is similar to that of the time-multiplexed etch process except that helium or liquid nitrogen is used to cool the wafer below -100°C . The etch chamber usually consists of ICP coils for plasma generation and a cathode for bombardment control [31].

At the Nanofab facility, LBNL, the cryo etching was carried out in an Oxford Instruments Plasmalab System 100 with a Cobra inductively coupled plasma (ICP) source and liquid nitrogen cryogenically cooled stage [14]. The ICP source is powered by a solenoidal coil at a frequency of 2 MHz with powers of 700–1000 W to generate a high density plasma. The whole chamber is pumped by a turbo molecular pump backed by a mechanical pump and the etch products are removed. The lower electrode was cooled with liquid nitrogen and helium gas was used as the thermal conducting medium between the wafer and electrode. The bottom electrode was powered by a RF frequency of 13.56 MHz for generation of a self DC bias. The process used for the etch was with a pressure of 6 mTorr, the processed substrate was always cooled to temperature of -120°C . The common plasma etch recipe parameters which were used in the conducted experiments are shown in Table 8.1.

8.2 Simulations

8.2.1 State of the art

While the **ViPER** simulator supports reactor scale simulations for plasma generation using pure SF_6 processing gas (described in Refs. 11, 103), the more complex SF_6/O_2 plasma gas mixture

Table 8.1: Common plasma etch recipe parameters used in the experiments

Recipe parameter	Base value	Range of change
Total gas flow rate	50 sccm	38 and 50 sccm
O ₂ fraction in the gas feed	24%	0–32%
Pressure	6 mTorr	Kept constant
ICP Power	700 W	700 and 1000 W
DC bias	–83 V	0 to –90 V
Wafer temperature	–120°C	Kept constant

has not yet been implemented. Hence only the feature scale module is used here. The inputs for the species above the sample are calibrated using a semi-empirical approach which will be described in significant detail within the following sections of this chapter.

Feature scale simulations of SF₆/O₂ cryogenic silicon etching have been previously addressed by several groups[99–101, 125–131] for etching of features predominantly in the micron scale. The model developed by Marcos *et al.* [125] was based on Monte Carlo techniques and considered the effects of species distributions, chemical etching, preferential sputtering, etched species redeposition and the passivation mechanisms. By conducting profile simulations for different adsorption probabilities, the role of oxygen regarding the passivation layer and the sidewalls protection was shown. In their further work[126], Marcos *et al.* investigated a dynamic of the aspect ratio dependent etching phenomenon, at the same time in relation to the transport of the reactive species inside the trench and the surface state at the trench bottom. The simulations revealed a very high oxygen sticking probability when the sample temperature was about –100°C. Furthermore, simulation models based on a Monte Carlo method and a Knudsen transport model were employed by Blauw *et al.* [128] and Maruyama *et al.* [129]. In these works, both groups investigated the role of depletion of the fluorine radical flux in narrow HAR structures during cryogenic Si etching. Maruyama *et al.* [129, 130] investigated ARDE phenomenon using Monte Carlo simulations based on a Knudsen transport model [132]. In the simulations described in [129], the reaction probabilities of F atoms with silicon surface at the sidewalls and at the trench bottom were varied as parameters. According to that study, the vertical etch rate is independent on the ion behavior and, in fact, is governed by the flux of F atoms, that is, the HAR cryogenic silicon etch process is in a neutral-flux-limited regime. In their next study [130], Maruyama *et al.* report that ions, scattered from the mask facets, are mainly responsible for lateral etching close to the mask. The authors conclude that an increase in the number of ions, scattered through reflection from the mask facets, leads to the time dependence of lateral etching. Moreover, a very comprehensive simulation model for silicon etching in SF₆/O₂ plasma was developed by Belen *et al.*[99, 100]. This semi-empirical feature-scale model included such mechanisms as chemical etching, ion-assisted etching, and sidewall passivation by oxygen atoms. Plasma diagnostics and previously published data were used to determine the ion flux, the ion angle and energy distributions, as well as the relative fluorine and oxygen fluxes at the surface of the sample. At the same time, experimentally inaccessible parameters were obtained by matching simulated feature profiles with appropriate etching experiments. The sample temperature was kept constant at 5°C. Finally, two works[101, 131] discussed the etching / sputtering yield

dependency on the ion angle of incidence for both, the silicon and the SiO_xF_y passivation layer.

The aim of the work presented here was to extend previous studies so that one can understand the more recent experimental work at the sub-100 nm nanoscale[13]. The form of angular yield dependence is considered separately for the passivant and silicon to determine how the O_2 content in the SF_6/O_2 feed gas influences the strength of the SiO_xF_y passivant as a function of feature size. After full calibration, simulations are applied at the nanoscale with very good results.

8.2.2 The implemented model

8.2.2.1 Plasma species and plasma sheath transport

As already mentioned (see section 6.3: *ViPER simulator overview*), the up to date version of the **ViPER** simulation software supports reactor scale simulations for plasma generation using pure SF_6 processing gas. Since the plasma generation using SF_6/O_2 gas mixture is not supported by the software at the moment due to its much higher complexity, it was decided in the context of the current work to restrict considerations to the feature scale simulations with utilization of a semiempirical approach. Namely, after implementation of the model, all its parameters are calibrated to the considered plasma etch hardware by matching simulated feature profiles with that obtained in corresponding etching experiments (using the same plasma etch recipe parameters).

Ignition of an SF_6/O_2 plasma results in a complicated chemistry consisting of a big variety of plasma species[133–135]. The situation is yet more complicated due to the interaction of the generated plasma species with each other[136]. Here we consider the dominant chemistries as identified in previous work.

In terms of the SF_6/O_2 silicon cryoetching process, reactive neutrals and ions must be considered. The two main reactive neutrals are fluorine and oxygen atoms[128]. The effective flux of fluorine atoms to the surface, Φ_F , will stand for the total flux of F atoms arriving at the surface either in atomic form or as part of a more complicated neutral radical. The same assumption is made for the effective oxygen flux, Φ_O . The fluxes Φ_F and Φ_O are assumed to be isotropic above the mask (no angular dependence), and the energy of such species is assumed to be equal to thermal energy. In terms of the ionic fluxes, Belen *et al.*[100] found via mass spectrometry measurements that SOF_3^+ is the dominant positive ion in the discharge. In the current model, the data of SOF_3^+ ion stands for the all positively ionized species delivered to the surface, and is denoted as Φ_i . All these fluxes, Φ_F , Φ_O and Φ_i , are input parameters to the profile simulations and their values are estimated during the calibration process.

Next the ion and energy angular distributions above the mask must be determined. Since the all considered experiments are conducted at low pressure in the reactor chamber (6 mTorr), a simplified sheath model[9, 11] was used to estimate the influence of plasma sheath on the ion angle and energy distributions. The average value for the incident ions' energy is calculated using the DC bias value V_{DC} measured during the plasma etching experiment being simulated. In addition

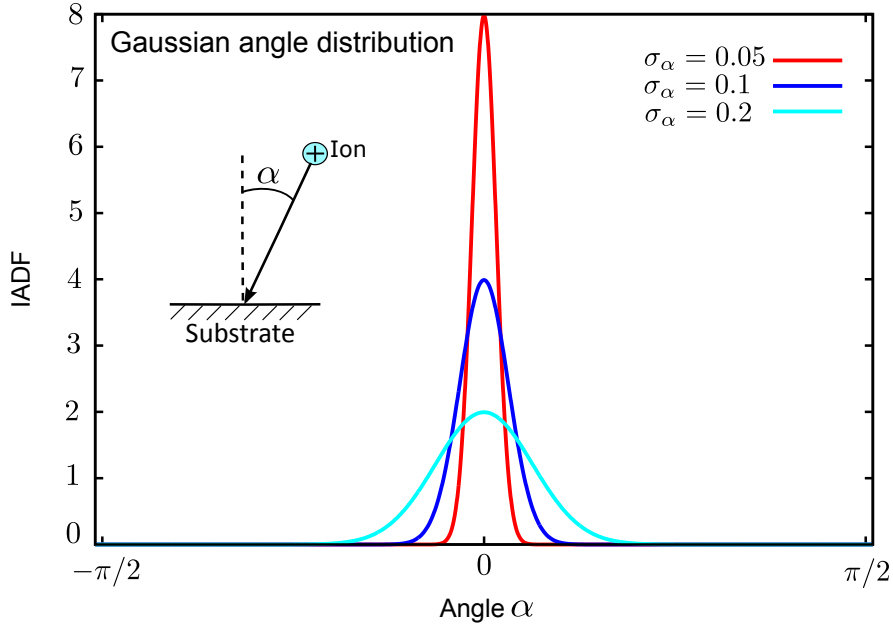


Figure 8.1: Examples of ion angular distribution functions (IADFs) using Gaussian distribution with different values of standard deviation σ_α .

and the time-averaged plasma potential V_p such that

$$E_{\text{ion}} = e(V_{\text{DC}} + V_p), \quad (8.1)$$

where e is the elementary charge.

This approach does not consider interactions of ions within the plasma sheath and averages the effects of the alternating rf field. This is a reasonable assumption for the simulated low-pressure regime experiments because the mean free path of ions is long in comparison to the thickness of the plasma sheath[137] and the ions remain in the sheath for several periods of the rf field (in the considered experiments the frequency is high enough — 13.56 MHz).

In this collisionless plasma sheath model, the positive ions have a very directional angle distribution function with a weak angular dispersion. In the model considered here, it is assumed that positive ions above the sample have a Gaussian angular distribution. Assuming α is the angle of incidence of the ion approaching the sample surface from the plasma sheath, the ion angle distribution function (IADF) close to the surface looks as follows (see also Fig. 8.1):

$$IADF(\alpha) = \frac{1}{\sigma_\alpha \sqrt{2\pi}} \exp \left\{ -\frac{\alpha^2}{2\sigma_\alpha^2} \right\}, \quad (8.2)$$

where the standard deviation σ_α of the IADF is a parameter that is estimated during the calibration of the model.

8.2.2.2 Feature scale transport of plasma species

The feature scale module of the simulator uses flux values, angle and energy distributions of ion and neutral species defined at the sheath boundary above the microstructure. With these values, it then calculates local fluxes and local angular distributions of the considered plasma species at each individual point of the simulated surface profile.

For the calculation of neutral transport within the microstructure, the software uses a newly implemented transport model[104], where such effects as adsorption and resorption of species are considered. That is, the total flux Φ_{tot} of any neutral species at any point of the surface consists of two fluxes – the flux coming directly from the plasma as well as the flux of reflected species.

In terms of adsorption of fluorine or oxygen atoms at the target surfaces, a very important parameter is a *sticking coefficient* – a probability that the atom of the species arriving at the surface will stay there (stick) and will not be reflected. The sticking coefficients commonly depend on the target material, its temperature and on that how clean is the target material. To determine the adsorption rate, the implemented model uses Langmuir adsorption kinetics. Using the adsorption of F species on silicon as an example, the adsorption rate will be expressed as

$$R_{\text{ads}} = S_{\text{F}}\Phi_{\text{F}}(1 - \Theta_{\text{F}}) = S_{\text{eff}}\Phi_{\text{F}}, \quad (8.3)$$

where Φ_{F} is the total fluorine flux, S_{F} is the temperature dependent sticking coefficient of fluorine on a clean silicon surface, Θ_{F} is the fluorine surface coverage. Terms are grouped to define S_{eff} , the effective fluorine sticking coefficient which depends on fluorine surface coverage Θ_{F} :

$$S_{\text{eff}} = S_{\text{F}}(1 - \Theta_{\text{F}}). \quad (8.4)$$

Based on the data from literature[128], the oxygen sticking coefficient S_{O} on a bare silicon at low temperature is assumed to be unity in all simulations of the current work, while the fluorine sticking coefficient is estimated during the model calibration procedure.

Ion transport calculations depend on the ion angle distribution and the ion flux predefined at the sheath lower boundary. Subsequent transport to the surface depends on sample geometry which determines the magnitude of ion shadowing by the mask as well as modification of the original ion trajectory by sidewall reflections and/or by the sample surface charging.

Several assumptions are made in the model to calculate ion trajectories. Like for the plasma sheath, the mean free path of the ions in the intra-feature area is assumed to be long in comparison to the dimensions of the etched features. Hence, changes to ion trajectories due to particle-particle collisions are not considered. Mask surface charging was found negligible in initial experiments with the simulator charging component module[1]. Thus, to increase the simulation efficiency the charging module was not employed. Given that local electric fields are negligible, the energy of the incident ions at any point of the microstructure surface is considered equal to that at the lower sheath boundary (calculated by Eq. 8.1).

Ion reflection at the feature sidewalls is an important component in the considered simulations. Ions coming with off-normal angles of incidence may be reflected at the feature sidewalls, such that the reflection probability is zero at normal ion incidence and increases with off-normal angle, approaching unity at grazing incident angles[138]. This reflection phenomenon is complicated by the fact that ions are not always reflected at perfectly specular angles, but often have a distribution which tends to broaden with increasing the ion mass[139].

Moreover, the mass of the ion as well as its incident angle and energy also have an impact on the ion reflection number efficiency and the ion reflection energy efficiency. Ion-assisted chemical etching of silicon depends on the ion incident angle[140, 141], where the etching yield curve is fairly flat and decreases monotonically with off-normal angle. In the model considered here, it is taken into account that the effective ion flux decreases with the incident angle (Lambert's cosine law). Additionally, it is considered that the ions which are hitting the sidewalls at grazing angles could also be reflected, which also decreases the number of ions involved in etching of the sidewalls. That is, the monotonic decrease in the etching yield with off-normal angle of incidence is also partly due to the ion reflection at the sidewalls[139].

In the developed model, after reflection, the ions are considered hot neutrals[139] the number of which and the energy is considered in the model to be negligible for etching after reflection to a new part of the surface. This only holds for short enough etching times as the experimental data shows the micro-trenching phenomenon occurs after particular etching depth. For instance, under almost identical conditions[13], the experimental study showed micro-trenching only after etching 5 microns in a 1.4 μm feature size. However for the regime addressed here, no evidence of micro-trenching developing was confirmed experimentally. For that reason in the current work, the ion reflections at the feature sidewalls are not considered explicitly (i.e. through Monte Carlo simulations), but only implicitly represented it in the form of the etching yield curve, which is discussed in more details in the next section. With this assumption, it is enough for the model to consider only direct line-of-sight ion shadowing to determine local ion flux as well as local ion angle distribution at each point of the simulated surface profile.

8.2.2.3 Surface kinetics and the importance of the oxygen sputtering yield

As already discussed in chapter 4: *Plasma etching of silicon*, the plasma-surface interaction in the context of silicon plasma etching is a complicated process and to simplify the model, at this point, mask erosion and its consequences is not considered. Three basic etch silicon etching mechanisms can be distinguished: chemical etching, physical sputtering and ion-assisted chemical etching (or reactive ion etching (RIE)). The total etching rate (ER_{tot}) as a combination of these three components[142]:

$$ER_{\text{tot}} = ER_{\text{chem}} + ER_{\text{sp}} + ER_{\text{i}}, \quad (8.5)$$

where ER_{chem} is the pure chemical etch rate, ER_{sp} is the etch rate due to physical sputtering mechanism and ER_{i} is the etch rate due to the ion-assisted etching.

For silicon etching in SF_6/O_2 plasmas, the etching rate during simultaneous exposure to ion

and neutral fluxes is much faster than the sum of the physical sputtering and chemical etching rates[143]. Thus for our process conditions, the influence of the physical Si sputtering on the total etch rate is insignificant[8] and can be neglected.

Under that condition, the total etch rate of silicon is given by

$$ER_{\text{tot}} = \frac{1}{\rho_{\text{Si}}} \left(\frac{\chi_{\text{F}}\sigma_{\text{Si}}\Theta_{\text{F}}}{4} + Y_{\text{Si}}\Phi_{\text{i}}\Theta_{\text{F}} \right), \quad (8.6)$$

where the first term in the sum represents the pure chemical etching, and the second one stands for the ion-assisted chemical etching. In Eq. 8.6, ρ_{Si} is the silicon density, $\chi_{\text{F}}\sigma_{\text{Si}}$ is the chemical etch reaction rate constant (χ_{F} is the coefficient defining the reaction frequency and σ_{Si} is the surface density of silicon atoms) and Y_{Si} is the ion-assisted etch yield. Furthermore, SiF_4 is considered the primary etch product of the F-Si chemical etch reaction[44] (giving the factor 4 in the chemical etch term $\chi_{\text{F}}\sigma_{\text{Si}}\Theta_{\text{F}}/4$).

The ion-assisted etch yield Y_{Si} comprises the yields of all kinds of etch reactions induced by the ion bombardment at the silicon surface removing some amount of Si atoms into the gasphase. The yield depends on the energy and incident angle of the impinging ions. In the current model, the incident ion energy E_{ion} is equal for any surface point and is determined by Eq. 8.1, while the local angular distribution of incident ions at each point of the target surface is determined by the ion transport model. Due to the study conducted by Steinbrüchel [21] (see also section 4.2: *Sputtering* in chapter 4: *Plasma etching of silicon*), the sputter yield Y_{sp} for silicon etching is proportional to the square root of the incident ions' energy E_{ion} :

$$Y_{\text{sp}}(E_{\text{ion}}) \approx A \left(\sqrt{E_{\text{ion}}} - \sqrt{E_{\text{th}}} \right), \quad (8.7)$$

where the constant A and the sputtering threshold energy E_{th} depend on the particular projectile-target combination.

Eq. 8.7 does not account for the impact angle which can significantly change the yield, for instance as shown by Rangelow[50]. The ion-assisted etching yield decreases with off-normal ion incident angles[138, 140, 141]. This is partially due to the ion reflection phenomenon, which in turn depends on the target surface state[144].

Hence, Eq. 8.7 is modified considering the yield dependence $f(\alpha_{\text{in}})$ on the ion angle of incidence α_{in} , in the implemented model, such that the general form of the yield per one incident ion is given by the expression

$$Y(E_{\text{ion}}, \alpha_{\text{in}}) = A \left(\sqrt{E_{\text{ion}}} - \sqrt{E_{\text{th}}} \right) f(\alpha_{\text{in}}), \quad (8.8)$$

where the parameter A and the sputtering threshold energy E_{th} depend on the particular projectile-target combination.

In order to determine the total yield at an individual point of the target surface, one needs to evaluate the integral over all incident angles ($-90^\circ \leq \alpha_{\text{in}} \leq 90^\circ$) accounting for the actual local

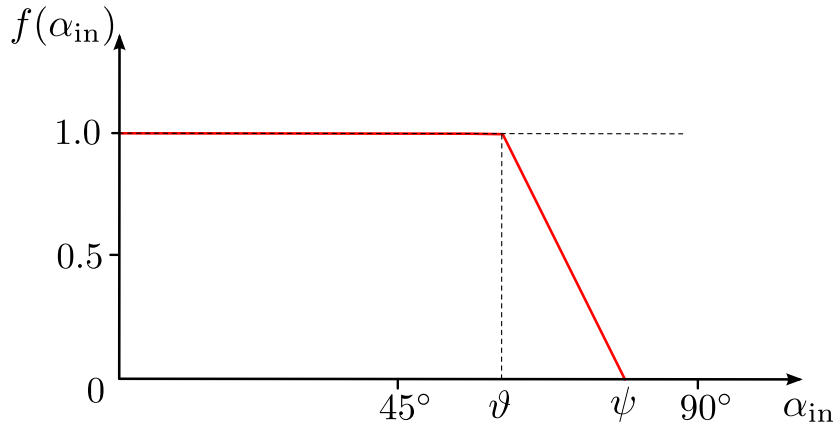


Figure 8.2: The form of the yield dependency on the ion angle of incidence in the developed model. The yield is constant (1.0) near normal incidence and decreases with increasing incidence angle. Final form of the dependency is defined by the combination of ϑ and ψ parameters.

angular distribution for incident ions at that point.

Similar to form of the yield angle dependence that was used by Marcos *et al.*[127] and Belen *et al.*[100], the yield curve is assumed to have the form shown in Fig. 8.2, where the yield is constant (1.0) near normal incidence and monotonically decreases with the angle of incidence. This dependence is defined in the developed model by a pair of parameters (see Fig. 8.2): ϑ is the largest incidence angle value with the yield still equal to 1.0, while for all angles of incidence larger than ψ , the yield vanishes. The dependency is also symmetric with respect to the ordinate axis (Fig. 8.2). In further description of the model, the form of the yield angle dependency will be described by the following notation: $f(\alpha_{in}) = \{\vartheta : \psi\}$, where ϑ and ψ will be given in degrees.

In the model, two yield dependencies are considered, the silicon yield and the oxygen yield. Consistent with established literature values[100, 127, 141], the ion incident angle dependency of the silicon etch yield Y_{Si} was assumed to have the form $f(\alpha_{in})_{Si} = \{60^\circ : 85^\circ\}$ and was kept unchanged in the all simulations.

From initial modeling of the experimental data, consideration of the oxygen sputtering yield from the SiO_xF_y film appears to be a crucial part of the profile evolution of the etched features. As oxidation competes with halogenation, the silicon is covered with a SiO_xF_y film[68, 71]. The exact composition and stoichiometry of this layer is not known and may vary. To investigate this, developed model parameterizes the form of the oxygen sputtering yield dependency on the ion angle of incidence (denoted as $f(\alpha_{in})_O = \{\vartheta : \psi\}$) [101, 131] and furthermore, considers its variation as a function of feature size and oxygen flux. It is expected as the oxygen content is increased relative to the fluorine, reaction layers with more oxygen atoms are created. Ultimately the layer will approach SiO_2 -like layers, this will have a different dependency on ion bombardment than an oxygen deficient layer[68]. In addition, features of different width will have different compositions because the oxygen transport will change with when feature sizes vary. Such transport effects as neutral and ion shadowing as well as Knudsen transport of neutrals are the main reasons for the aspect ratio dependent etching (ARDE) phenomenon[5] (see section 5.2.3: *Pattern shape effects* in chapter 5: *Transport phenomena*). ARDE is the dependence of etching rate on the feature

Table 8.2: Summary of the model parameters to be determined.

Model parameter	Estimation method
Fluorine flux, Φ_F	Variation with plasma conditions is obtained from fitting during the calibration process, using auxiliary data taken from literature [145]. Absolute value is estimated by matching simulated profiles with experiments.
Oxygen flux, Φ_O	Variation with plasma conditions is obtained from fitting during the calibration process. Auxiliary data taken from literature[45]
Fluorine sticking coefficient on a clean Si surface, S_F	Estimated by matching simulated profiles with experiments
Oxygen sticking coefficient on a clean Si surface, S_O	Taken from literature [99, 100, 128] and kept constant (1.0)
Chemical etch rate constant, $\chi_F \sigma_{Si}$	Estimated by matching simulated profiles with experiments
O recombination constant, $\eta_O \sigma_{Si}$	Taken from literature[100] and kept constant ($4 \times 10^{13} \text{ cm}^{-2} \text{ s}^{-1}$)
Ion flux, Φ_i	Taken from literature[100] and kept constant ($1 \times 10^{16} \text{ cm}^{-2} \text{ s}^{-1}$)
Standard deviation of the ion angular distribution, σ_α	Estimated by matching simulated profiles with experiments
Silicon yield proportionality constant, A_{Si}	Estimated by matching simulated profiles with experiments
Oxygen yield proportionality constant, A_O	Estimated by matching simulated profiles with experiments
Ion incident angle dependency of silicon etch yield, $f(\alpha_{in})_{Si}$	Assumed to be $\{60^\circ : 85^\circ\}$ and is kept unchanged in all simulations
Ion incident angle dependency of oxygen sputtering yield, $f(\alpha_{in})_O$	Estimated by matching simulated profiles with experiments
Silicon etching threshold energy, $E_{th,Si}$	Taken from literature[100] and kept constant (15 eV)
Oxygen sputtering threshold energy, $E_{th,O}$	Taken from literature[100] and kept constant (10 eV)

aspect ratio, where it is imperative that etching rates are determined as a function of time for several feature widths[5].

Previous studies[101, 131] only looked at features of one size but here in the current work, considering both size and oxygen flux, the importance of the variation of the strength of the SiO_xF_y passivant with these parameters becomes apparent. The parameter A_O in the oxygen sputtering yield, Y_O as well as the variables ϑ and ψ of the $f(\alpha_{\text{in}})_O$ parameter in Y_O were fit within the simulations by matching simulated profiles with experimental results to investigate this effect.

The last thing to develop in the model is to consider the surface coverages for fluorine and oxygen, Θ_F and Θ_O . The fluorine and oxygen surface coverages are determined by means of Langmuir-Hinshelwood-type surface site balances. Here the model uses the assumptions employed by Belen *et al.* in their simulation model[100]. That is the only way fluorine and oxygen atoms stick to the surface is a direct adsorption onto available surface sites. F may desorb from the surface by means of spontaneous etching mechanism in form of SiF_4 volatile products or it may leave the surface through the ion-assisted mechanism in form of SiF_2 product. Oxygen atoms are assumed to leave the surface also by two mechanisms: either by O-to-O recombination forming O_2 or by ion-enhanced sputtering of oxygen. Overall surface site balances are given by:

$$\sigma_{\text{Si}} \frac{d\Theta_F}{dt} = S_F \Phi_F (1 - \Theta_F - \Theta_O) - \chi_F \sigma_{\text{Si}} \Theta_F - 2Y_{\text{Si}} \Phi_i \Theta_F, \quad (8.9)$$

and

$$\sigma_{\text{Si}} \frac{d\Theta_O}{dt} = S_O \Phi_O (1 - \Theta_F - \Theta_O) - \eta_O \sigma_{\text{Si}} \Theta_O - Y_O \Phi_i \Theta_O, \quad (8.10)$$

where S_F and S_O are the fluorine and oxygen sticking coefficients on a clean silicon surface, Θ_F and Θ_O are the F and O surface coverages, Φ_F and Φ_O are the fluorine and oxygen fluxes and $\eta_O \sigma_{\text{Si}}$ is the oxygen recombination constant.

Assuming pseudo-steady-state conditions, the F and O surface coverages can be written as

$$\Theta_F = \frac{1}{1 + \left(\frac{\chi_F \sigma_{\text{Si}} + 2Y_{\text{Si}} \Phi_i}{S_F \Phi_F} \right) \left(1 + \frac{S_O \Phi_O}{\eta_O \sigma_{\text{Si}} + Y_O \Phi_i} \right)}, \quad (8.11)$$

and

$$\Theta_O = \frac{1}{1 + \left(\frac{\eta_O \sigma_{\text{Si}} + Y_O \Phi_i}{S_O \Phi_O} \right) \left(1 + \frac{S_F \Phi_F}{\chi_F \sigma_{\text{Si}} + 2Y_{\text{Si}} \Phi_i} \right)}. \quad (8.12)$$

After the model was integrated into the **ViPER** simulator, it was necessary to calibrate it for the cryogenic plasma etch hardware and processes tested. Therefore, a series of experiments and simulations were conducted to estimate the most critical parameters of the model. A summary of all the model parameters and which ones require calibration is shown in Table 8.2.

8.2.2.4 Chemical etching parameters calibration

To determine the model parameters representing the chemical etching mechanism, one needs to conduct experiments where this mechanism is the prevailing component of the silicon etch rate. To do so, sidewall passivation and ion-assisted etch mechanism must be negligible. To this end, first series of experiments was conducted, where silicon samples were etched in a pure SF₆ plasma, in order to eliminate the influence of oxygen additions to the feed gas (some oxygen will be present for example, due to oxygen containing components being etched in the chamber). The rf power at the cathode was switched off in order to mitigate the impact of ion bombardment on the etching process (DC bias was assumed to be equal to zero). The plasma etch recipe used is shown in Table 8.3. Trenches etched with this recipe having widths of 2 μm, 1.3 μm, 700 nm and 500 nm were simulated.

Table 8.3: Plasma etch recipe used for the calibration of chemical etching parameters.

Recipe parameter	Value
SF ₆ gas flow rate	38 sccm
Pressure	6 mTorr
ICP Power	700 W
DC bias	0 V
Wafer temperature	-120°C
Etch duration	1 min.

Assuming that only the chemical etch component is dominant and neglecting ion-assisted etching, Eq. 8.6 can be simplified such that the total silicon etching rate can be written as follows:

$$ER_{\text{tot}} = \frac{1}{\rho_{\text{Si}}} \frac{\chi_{\text{F}} \sigma_{\text{Si}} \Theta_{\text{F}}}{4}, \quad (8.13)$$

and Eq. 8.11, the F surface coverage in Eq. 8.13 will be expressed as

$$\Theta_{\text{F}} = \frac{1}{1 + \frac{\chi_{\text{F}} \sigma_{\text{Si}}}{S_{\text{F}} \Phi_{\text{F}}}}. \quad (8.14)$$

The parameters that need to be determined via the calibration step are the fluorine flux Φ_{F} , fluorine sticking coefficient on a clean silicon surface S_{F} and the chemical etch rate constant $\chi_{\text{F}} \sigma_{\text{Si}}$. After running numerous simulations with different combinations of the parameters, the parameters which yield the best agreement between simulated and experimental results were determined and are shown in Table 8.4. Fig. 8.3 shows the simulation results and fits using these parameters and there is an very good fit to the trench profiles obtained in the experiment.

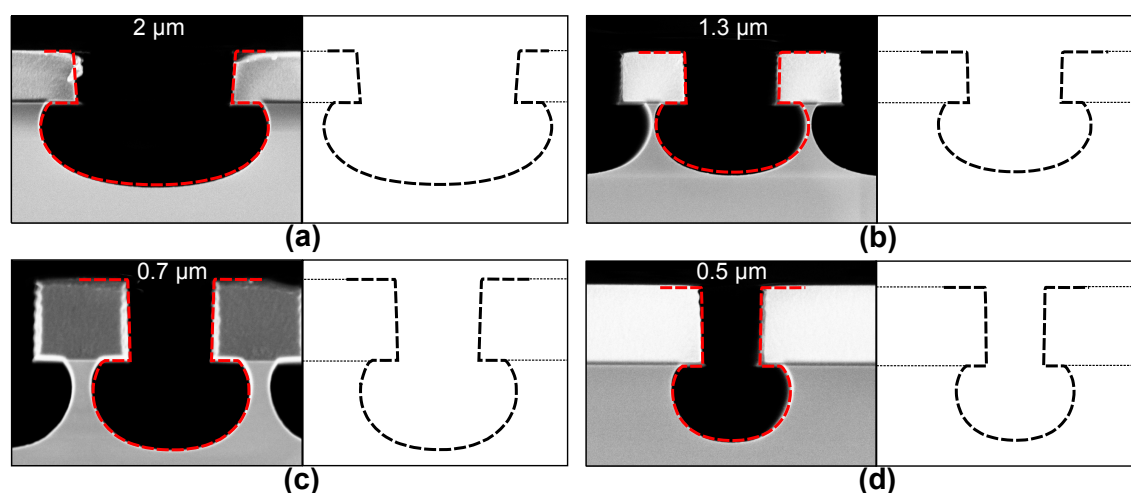


Figure 8.3: Calibration of chemical etch parameters. After calibration, the simulated profiles are in a good agreement with the feature profiles obtained in the experiment. (a): 2 μm feature, (b): 1.3 μm feature, (c): 700 nm feature, (d): 500 nm feature.

Table 8.4: The model chemical etch parameters' values determined during the calibration.

Chemical etch parameter	Value
Fluorine flux, Φ_{F} [$\text{cm}^{-2}\text{s}^{-1}$]	0.7×10^{18}
F sticking coefficient on a clean Si surface, S_{F}	0.75
Chemical etch rate constant, $\chi_{\text{F}}\sigma_{\text{Si}}$ [$\text{cm}^{-2}\text{s}^{-1}$]	3.0×10^{18}

8.2.2.5 Ion-assisted etching parameters calibration

After the determination of chemical etching parameters, the ion-assisted etching parameters of the implemented model are estimated. To this end, in addition to the previously used plasma etch recipe using pure SF_6 plasma (Table 8.3), the rf power at the cathode was switched on to significantly increase the influence of ion bombardment. The modified recipe is shown in Table 8.5.

Table 8.5: Plasma etch recipe used for the calibration of ion-assisted etching parameters.

Recipe parameter	Value
SF_6 gas flow rate	38 sccm
Pressure	6 mTorr
ICP Power	700 W
DC bias	-90 V
Wafer temperature	-120°C
Etch duration	1 min. and 3 min.

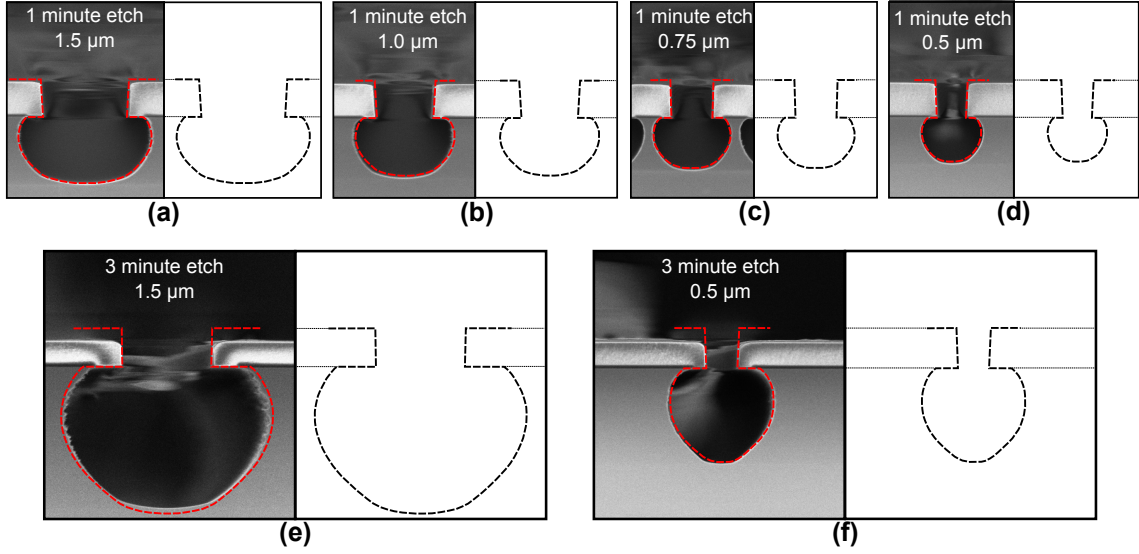


Figure 8.4: Calibration of ion-assisted etch parameters. After the calibration, the simulated profiles are in a very good agreement with the feature profiles obtained in the experiments. Duration of etching: 1 minute etching in (a), (b), (c) and (d); 3 minute etching in (e) and (f). Feature widths: 1.5 μm in (a) and (e); 1 μm in (b); 750 nm in (c); 500 nm in (d) and (f).

Accounting for the appearing ion-assisted component, the total etching rate is given by

$$ER_{\text{tot}} = \frac{1}{\rho_{\text{Si}}} \left(\frac{\chi_{\text{F}} \sigma_{\text{Si}} \Theta_{\text{F}}}{4} + Y_{\text{Si}} \Phi_{\text{i}} \Theta_{\text{F}} \right), \quad (8.15)$$

where the fluorine surface coverage is calculated by

$$\Theta_{\text{F}} = \frac{1}{1 + \left(\frac{\chi_{\text{F}} \sigma_{\text{Si}} + 2Y_{\text{Si}} \Phi_{\text{i}}}{S_{\text{F}} \Phi_{\text{F}}} \right)}. \quad (8.16)$$

Using the calibrated parameters from Table 8.4, the additional parameters to be calibrated within these experiments relate to the ion-assisted silicon etch yield, Y_{Si} . Recalling Eq. 8.8, the Y_{Si} , depends on the silicon yield proportionality constant A_{Si} and ion incident angle, $f(\alpha_{\text{in}})_{\text{Si}}$. A_{Si} is determined within the calibration while, as mentioned earlier (see Table 8.2), the dependency of Y_{Si} on the ion incident angle is assumed to be $f(\alpha_{\text{in}})_{\text{Si}} = \{60^\circ : 85^\circ\}$ and is kept constant during the all simulations. In the absence of sidewall passivation (no oxygen in the discharge), the etching process remains highly isotropic. Predominantly isotropic processes do not allow exact determination of the standard deviation parameter σ_{α} of the ion angular distribution (Eq. 8.2), within the isotropic calibration its influence is considered for this insignificant. During this calibration, the value of $\sigma_{\alpha} = 0.08$ was used and the parameter was estimated in subsequent experiments producing anisotropic profiles.

In terms of the considered calibration of ion-assisted etch parameters, two experiments (see the recipe in Table 8.5) were simulated with duration of 1 and 3 minutes. The results after the calibration process are shown in Fig. 8.4.

In comparison to the previous experiment with no rf power at the cathode, the fluorine flux has

slightly increased with the additional DC bias. It is supposed that additional rf power generates additional dissociation and slightly increased the intensity of the fluorine flux. This is also confirmed experimentally (Fig. 8.3 and Fig. 8.4). The calibrated parameters are shown in Table 8.6.

Table 8.6: *The model parameters for simulating the best match with experiments described in Table 8.5.*

Parameter	Value
Fluorine flux, Φ_F [$\text{cm}^{-2}\text{s}^{-1}$]	0.75×10^{18}
F sticking coefficient on a clean Si surface, S_F	0.75
Chemical etch rate constant, $\chi_F \sigma_{\text{Si}}$ [$\text{cm}^{-2}\text{s}^{-1}$]	3.0×10^{18}
Ion flux, Φ_i [$\text{cm}^{-2}\text{s}^{-1}$]	1.0×10^{16}
Standard deviation of the ion angular distribution, σ_α	0.08
Silicon yield proportionality constant, A_{Si}	4.0
Silicon yield dependency on the ion angle of incidence, $f(\alpha_{\text{in}})_{\text{Si}}$	$\{60^\circ : 85^\circ\}$
Silicon etching threshold energy, $E_{\text{th,Si}}$, [eV]	15.0

8.2.3 Aspect ratio dependent etching and the effect on passivation composition

The next step in the calibration process is to understand the role oxygen plays in the profile evolution. The model calibration now considers processes using SF_6/O_2 with different amounts of oxygen in the plasma discharge. A series of experiments were simulated, where 1.5, 1.0 and 0.5 μm wide features were etched as a function of the SF_6/O_2 flow rate ratio (the details are shown in Table 8.7). With these experiments, the formation of the SiO_xF_y passivation layer is probed depending on the oxygen content in the feed gas and how its composition and sputtering yield correlates with the aspect ratio dependent etching phenomenon.

Table 8.7: *Plasma etch recipe used for the calibrations with different oxygen content in the feed gas.*

Recipe parameter	Value
Total SF_6/O_2 gas flow rate	50 sccm
O_2 flow rates in total gas feed studied	0,2,4,6,8,10,12 sccm
Pressure	6 mTorr
ICP Power	700 W
DC bias	-83 V
Wafer temperature	-120°C
Etch duration	3 min.

This approach to this simulation study was to determine model parameters such as the standard deviation value σ_α of the ion angular distribution function, which can not be determined from the isotropic processes simulated in the previous experiments. It is possible to estimate this parameter if sufficient amounts of oxygen are introduced to make the overall profile shape dominantly anisotropic but which are at the same time not enough for formation of a very strong passivant at the silicon surface, characteristic of the over-passivation regime.

For the case of no O_2 content in the SF_6/O_2 feed gas (50–0 sccm), the absolute value of the effective fluorine flux Φ_F was determined using the previously found parameter values shown in Table 8.6 (S_F , $\chi_F \sigma_{Si}$, Φ_i , σ_α , A_{Si} , $f(\alpha_{in})_{Si}$, $E_{th,Si}$) together with Eqs. 8.15 and 8.16. The variation of the effective fluorine and oxygen fluxes with O_2 content in the feed gas was determined by combining literature dependencies and fits of the simulated feature profiles. First, the work of Pateau *et al.*[145] was used to set the fluorine flux as a function of oxygen in the feed gas. Accordingly, the baseline flux, determined from simulations of Fig. 8.5(a) where the oxygen content was zero, was increased as O_2 in the feed gas increased. Using these fluorine fluxes, the O flux was determined via simulations of the experimental profiles. The considered variation of oxygen flux as a function of O_2 content in the feed gas generally corresponds to the variation of O atomic concentration with the increase of O_2 content in the SF_6/O_2 reported by D'Agostino and Flamm[45] in their experimental study. To consider the presence of some O_2 amount in the feed gas in the remaining experiments of the current study, some additional parameters of the model need to be estimated. These are the oxygen yield proportionality constant, A_O , and the O yield dependency on the ion angle of incidence, $f(\alpha_{in})_O = \{\vartheta; \psi\}$.

In terms of the SiO_xF_y passivation layer formation, A_O and $f(\alpha_{in})_O$ parameters of the implemented model have an important influence on the etched trench profile evolution. Both of them depend on the strength of the SiO_xF_y passivant and in fact this is a very important point of this part of the work. The amount of oxygen atoms removed from the passivation layer per one incident ion (regardless of its angle of incidence), A_O parameter represents how effectively the passivant is eroded by ion bombardment. This parameter has the biggest impact on the vertical etching rate at the trench bottom. Smaller A_O parameter means the SiO_xF_y passivant is more resistant to normally incident ion at the trench bottom resulting in lower overall etching rates. This can be accomplished by increasing oxygen in the feed gas to make a more oxygen rich SiO_xF_y layer. Hence in this study, A_O was decreased with the increasing O_2 content to be consistent with this phenomenon.

While the A_O parameter is dominant when considering the etch rate at the bottom of the evolving trench (all ions effectively normal incident), the $f(\alpha_{in})_O$ parameter has the dominant effect on etching rate at the feature sidewalls (ions hitting the surface at grazing angles and thus the O sputtering yield is reduced). This parameter starts playing a significant role in particular in the over-passivation regime at which the increased strength of the passivation film leads to positively tapered profile of the etched features. To obtain the best simulated fit of experimental profiles as a function of oxygen content in the feed gas, the $f(\alpha_{in})_O$ parameter (values of ϑ and ψ) was varied to the corresponding experimental results in the over-passivation regime. As the values of ϑ and ψ decrease, the strength of the passivant increases.

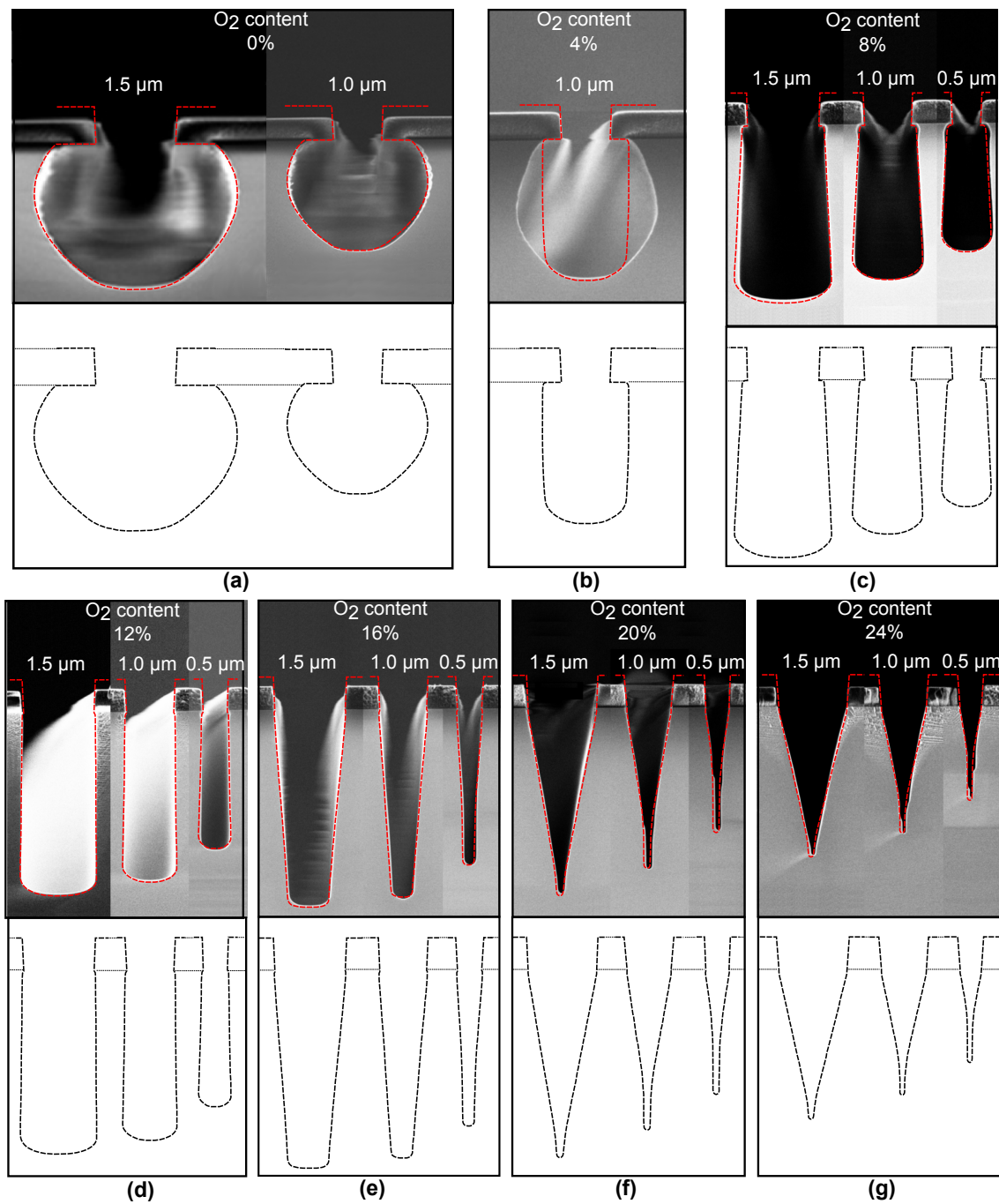


Figure 8.5: Calibration of the model using different values of oxygen content in the feed gas. Used SF_6/O_2 gas flow ratios: (a) 50–0 sccm, (b) 48–2 sccm, (c) 46–4 sccm, (d) 44–6 sccm, (e) 42–8 sccm, (f) 40–10 sccm, (g) 38–12 sccm. Mask height before etching: 700 nm.

The parameters providing the best matching of the simulated profiles to the experiments are presented in Table 8.8 while Fig. 8.5 shows simulated fits to the experimental results.

Overall all, simulated profiles are in a good agreement with the etched feature profiles obtained in the experiments. However, there is one significant deviation as shown in Fig. 8.5(b). This is in the low oxygen regime, 4% of total feed gas supply. This deviation at very low oxygen content values may be due to an additional O surface loss mechanism, not included in the model, but significant

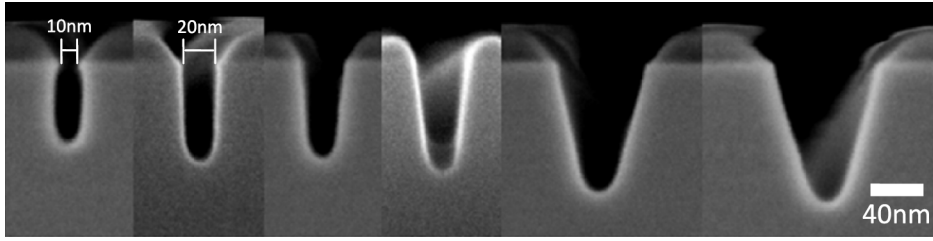


Figure 8.6: Nanoscale silicon cryoetching experiments conducted by Liu et al[13]. The original picture can be found in Ref. 13. Different feature sizes after 20 s etching, 10, 20, 30, 40, 90, 110 nm from left to right. Mask height before etching: 60 nm.

at lower oxygen covers. With such O coverage, the etching will be more isotropic than determined by the simulation.

Beyond the determination of A_O and $f(\alpha_{in})_O$, these simulations allowed us to determine the standard deviation value of the ion angular distribution function, σ_α . Simulations shown in Fig. 8.5(c) and Fig. 8.5(d) were particularly useful because the used amounts of oxygen have been sufficient to make the overall profile shapes predominantly anisotropic and at the same time still not enough to bring the process to the over-passivation regime. The σ_α parameter was found to have the value of 0.05 and was kept constant for all simulations of this study.

With respect to the A_O and $f(\alpha_{in})_O$ values, feature size dependent effects were found. In the over-passivation regime (the simulated profiles in Fig. 8.5(e), Fig. 8.5(f) and Fig. 8.5(g)), $f(\alpha_{in})_O$ parameter slightly changes with respect to the trench width. The combination $\{\vartheta; \psi\}$ has greater values with decreasing the width of the etched feature whereas the O yield proportionality constant A_O remains constant. This dependency indicates that in particular in the over-passivation regime and under the same plasma etching recipe conditions, the SiO_xF_y layer becomes weaker when the feature width is reduced.

The author of this work believes this is a consequence of Knudsen transport[132], where the neutral species with higher sticking coefficient are depleted faster with aspect ratio[128]. Oxygen radicals, which have a higher sticking coefficient than fluorine radicals will be depleted faster due to aspect ratio effects introduced by the mask. With a constant mask height, the mask aspect ratio (MAR): $MAR = \text{mask height} / \text{mask aperture}$ is larger for narrower features. This difference leads to additional shadowing with smaller features because the overall aspect ratio ($AR = \text{feature depth} / \text{feature width}$ where $\text{feature width} \approx \text{mask aperture}$) also included the mask height. In the considered study, the mask height was 700 nm whereas the mask aperture value varied from 1500 nm to 500 nm, namely the mask aspect ratio varied from 0.47 to 1.4. In this case, the influence of the additional shadowing has a small but notify effect on the strength of the SiO_xF_y passivation layer. The significance of the effect becomes more dramatic for much smaller nanofeatures where the range of the mask aspect ratio change may be much larger. For example, Fig. 8.6 shows nanoscale silicon cryoetching experiments[13] for feature widths between 10 to 110 nm with an initial mask height of 60 nm. Here, the mask aspect ratio varies from ≈ 0.55 to 6.0. To obtain enough passivant to provide anisotropic profiles in the smallest features the oxygen content in the feed gas was increased from 6 sccm (for large features in Fig. 8.5) to 16 sccm with a total flow 50 sccm (Note:

the ICP power is 1000 W as compared to 700 W in Fig. 8.5 but this is inconsequential to the present discussion.) This higher level of oxygen produces an anisotropic, approximate straight-walled profile for the 10 nm feature, results in a positively tapered profile; the larger aperture / smaller aspect ratio allows more oxygen to reach the bottom of the feature, strengthening the passivant. Overall, this difference in oxygen transport with changing aspect ratios (in large part due to the constant mask height) produces a profile angle dependent on feature width. Hence, the process window for vertical profiles as a function of feature size is much narrower.

8.2.4 Nanoscale cryoetching simulation

After the implemented cryo etch simulation model has been tested and calibrated in terms of the micro-features etching (trench widths in the range of $2\ \mu\text{m} - 500\ \text{nm}$), it was employed for simulation of silicon cryoetching at the nanoscale. Self-assembled soft organic materials, e.g., block

Table 8.9: *Plasma etch recipe used for the anisotropic nanoscale cryoetching of 35 nm wide features.*

Recipe parameter	Value
Total SF ₆ /O ₂ gas flow rate	50 sccm
SF ₆ to O ₂ ratio in the total gas feed	34-16 sccm
Pressure	6 mTorr
ICP Power	1000 W
DC bias	-30 V
Wafer temperature	-120°C
Etch duration	15 sec.

copolymers have received significant attention in terms of patterning arrays of nanostructures[146, 147]. For the considered testing of the model, an etch experiment was used where anisotropic nanofeatures (35 nm width) were etched in silicon using a block copolymer mask[73]. Although there are no infinite length trenches in the chosen etched pattern, the utilization of a 2D approach is supposed to be still feasible here, since very shallow mask is considered and the ratio of the etching depth to the feature width is in the range of two to three. Moreover, there are no sharp corners or curvatures in the structures considered in the simulation. For that reason, the influence of the length of the trenches is considered negligible. The utilized plasma etch recipe is shown in Table 8.9. In the used plasma etch recipe, the already discussed tuning for nanofeatures etching was employed (O₂ fraction in the SF₆/O₂ gas feed increased to 34-16 sccm, ICP power increased to 1000 W). The ICP power was higher than the initial calibration as it was found to give better results. The initial calibration measurements were extrapolated to this slight change in plasma discharge configuration. With this high level of oxygen, the O yield proportionality constant A_O was reduced to 1.0. For obtaining the best simulation results, the O yield was found to be independent of ion angle of incidence for angle values between 0° and 60°, which means that the passivant is not strong enough for the formation of positively tapered feature profile at least at the considered aspect ratio. This may be attributed to the very low mask aspect ratio (the mask height was only 6 nm). Moreover,

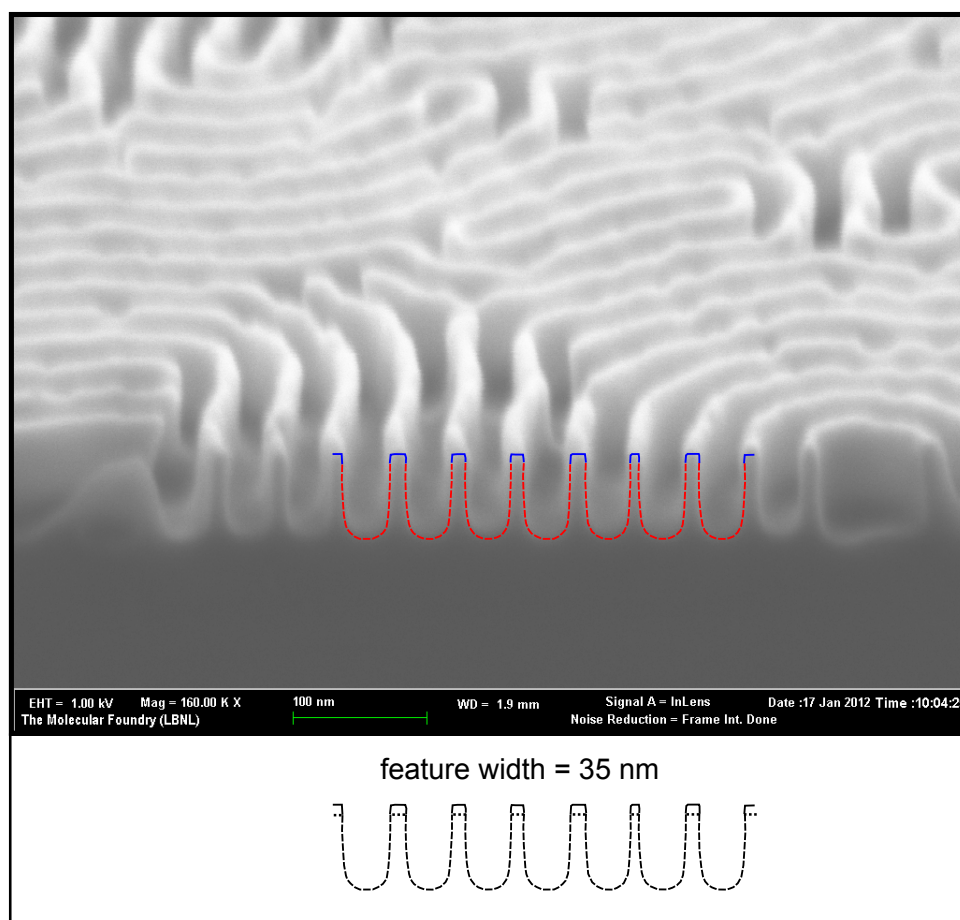


Figure 8.7: Utilization of the implemented model for simulation of cryogenic silicon etching at the nanoscale (feature width 35 nm, mask height 6 nm). The processed wafer is patterned using a block-copolymer mask[73] (the original picture as well as the full details of the considered experiment can be found in Ref.73). The simulation demonstrates a very good agreement with the experiment.

this effect can be also amplified due to a lower DC bias value used in the considered experiment (in comparison to the experiment described in the previous section). The ions with lower energy have larger average angle of incidence[128], and thus the erosion of the sidewall passivation is relatively stronger. Therefore, $f(\alpha_{in})_O$ parameter was assumed to be equal to $\{60^\circ : 85^\circ\}$ and σ_α parameter was chosen to have a larger value of 0.1. All other model parameters were chosen accounting for the data obtained in the previous series of simulations.

The overlay of the simulated profiles and experimental results is shown in Fig 8.7. The simulation results are in a good agreement with the experiment. The model parameters used in the simulation are listed in Table 8.10.

8.3 Conclusion to the implemented cryogenic etch simulation model

Cryogenic etching of silicon has significant advantages in terms of increased soft-mask selectivity and smooth walled high aspect ratio feature etching / nanoscale etching for device miniaturization in nanoelectronics and NEMS. A new simulation model of the cryogenic etching of silicon was

Table 8.10: *The model parameters for simulating the best match with the experiment described in Table 8.9.*

Parameter	Value
Fluorine flux, Φ_F [$\text{cm}^{-2}\text{s}^{-1}$]	1.5×10^{18}
Oxygen flux, Φ_O [$\text{cm}^{-2}\text{s}^{-1}$]	1.3×10^{17}
F sticking coefficient on a clean Si surface, S_F	0.75
O sticking coefficient on a clean Si surface, S_O	1.0
Chemical etch rate constant, $\chi_F \sigma_{Si}$ [$\text{cm}^{-2}\text{s}^{-1}$]	3.0×10^{18}
O recombination constant, $\eta_O \sigma_{Si}$ [$\text{cm}^{-2}\text{s}^{-1}$]	4×10^{13}
Ion flux, Φ_i [$\text{cm}^{-2}\text{s}^{-1}$]	1.1×10^{16}
Standard deviation of the ion angular distribution, σ_α	0.1
Silicon yield proportionality constant, A_{Si}	4.0
Oxygen yield proportionality constant, A_O	1.0
Ion incident angle dependency of Si etch yield $f(\alpha_{in})_{Si}$	$\{60^\circ : 85^\circ\}$
Ion incident angle dependency of O sputtering yield, $f(\alpha_{in})_O$	$\{60^\circ : 85^\circ\}$
Silicon etching threshold energy, $E_{th,Si}$ [eV]	15.0
Oxygen sputtering threshold energy, $E_{th,O}$ [eV]	10.0

developed herein and integrated into the **ViPER** simulation software to understand the SF_6/O_2 cryogenic process applications for nanoscale etching. The considered semi-empirical model was developed with high accuracy because the model can be distinctly calibrated to the etching equipment utilized. By proper calibration, the developed model can help to estimate the parameters (like, for example, fluxes of key plasma species to the sample, sticking coefficients, dependence of etch and sputtering yields on incident angle and energy of impinging ions, etc.) which are usually very complicated or impossible to determine in terms of experiments. Starting by etching features from 500 nm to 2 microns, the model was calibrated and relevant parameters fit. Extending the model to the deep nanoscale, the author of this work was able to simulate silicon etching of 25 nm half-pitch using a very thin mask derived from block copolymer lithography. The model showed that the experimental finding that nanoscale features need more oxygen for vertical anisotropic profiles [13, 14], is a consequence of the combination of Knudsen transport depleting oxygen faster than fluorine due to the higher sticking coefficient of oxygen and the SiO_xF_y passivation layer sputtering yield is strongly dependent on the oxygen content in the feed gas. Mask charging was

found to be a negligible effect to the erosion of the passivant layer and the process overall as presumed in the experimental work[14]. Excellent simulation fits were found for the simulated features except in the very small oxygen regime (4% O₂ in the SF₆/O₂ feed gas). This suggests an additional, not considered by the model, O surface loss mechanism at the very low oxygen end. The simulation model provided a very good insight into the cryogenic etching process and its application to nanoscale feature etching.

Utilization of the model can greatly simplify further development of the process while trying to etch high aspect ratio features with sizes of several nanometers. By reducing the needed number of experiments, the model can significantly economize the time and costs in terms of further research on cryogenic etching of silicon at the nanoscale.

As a perspective for the developed model, the author of this work sees its further extension by various calibrations with respect to different regimes of plasma etch experiments (different values of the chamber pressure and ICP power), depending on the demands of further research in terms of cryogenic silicon etching by SF₆/O₂ plasma.

Chapter 9

Conclusions and outlook

In terms of this work, two objectives were pursued and accomplished.

The first one was a creation of simulation model, which allows modelling the influence of local surface charging on the evolving feature profile during plasma etching simulations. The developed model simulates the transport of charged particles (electrons and positive ions) from the lower plasma sheath boundary to the target surface through electric field, induced by surface charging of insulating materials of the sample. As a result of charging simulation, the model yields positive ion flux distribution along the simulated profile surface, which is then used in the etch rate calculations for the modelling of feature profile evolution on a considered time step of the conducted plasma etching simulation.

For electric field calculations, the developed model employs a finite element method (FEM) together with a two-dimensional triangular mesh generator [117], which allows handling complicated geometries of the area of interest that can arise during gas chopping plasma etching simulations. As an additional feature, the developed charging effect model is able to allow for electric field not only in the gas-phase within the microstructure but also in insulating materials of the sample (photoresist mask, underlying oxide, etc.). Such additional simulation possibilities can be very useful when trying to estimate the impact of either different mask configurations or oxide layer thickness on the surface charging, thus, on the profile shape evolution. It has been shown that for the problem is sufficient, to solve Laplace differential equation which yields an electric potential distribution in the simulation area. To obtain the solution, corresponding boundary conditions were developed. For the lower plasma sheath boundary, a Dirichlet boundary condition is imposed, implying the electric field of the plasma sheath has there no more significant influence on the velocity of charged particles coming from the plasma. A homogeneous Neumann boundary condition is imposed at the left and right side of the area of interest thus implementing a mirroring of the simulation area to the left and to the right. Hence, the influence of electric fields from adjacent features is also taken into account. The influence of surface charging, expressed by charged density values at nodes of the simulated profile surface, is considered by using inhomogeneous Neumann boundary condition. In this work, the corresponding formula was developed for two kinds of boundary interfaces: insulator – conductor and insulator – insulator.

For the transport of charged particles in the intra-feature area, the model employs a Monte Carlo method. Using angular and energy distribution functions for ions and electrons in the vicinity of the sample, which were previously calculated by the plasma sheath model, the simulated particles are generated at the lower sheath boundary and then tracked through the simulation area until they reach the target surface or are repelled back into the plasma. For particle trajectory calculation, the model employs the FEM mesh which was previously created during the electric field calculation. Each simulated particle is tracked from one finite element to another, whereas equation of motion for the particle is two times analytically integrated over the time at each of the elements. Since the next finite element, the particle flies in, is automatically known and one does not need to search for it among all finite elements of the mesh, the utilized approach greatly reduces the computational time, thus making the model much more effective.

The developed charging model was validated using experimental data provided by Oxford Instruments Plasma Technology. By the simulation of plasma etching experiment using gas chopping method, it was shown that the model can capture well the notching and bowing effects and yield plausible results.

For the first time, the charging effect was simulated during the entire course of the etching process and the obtained results were compared with the corresponding experimental data demonstrating very good agreement. Furthermore, regarding the considered experiment, the model has shown how the resulting profile appeared, namely by the etching of the profile ripples on the side-walls during the overetching, thus giving more insight into the surface profile evolution dynamics.

The author of this work believes, that further utilization of the model within the **ViPER** simulation software gives great possibility to understand large number of secondary effects and learn how to prevent them, concerning not only plasma etching but also plasma deposition processes. As an outlook to the model, it is instructive to test the model in simulations of experiments, in which different kinds of plasma etching processes are used to obtain features of different sizes and aspect ratios. Application of the developed charging effect simulation model to plasma etching of nano-features is of particular interest.

The second objective of this work was to develop a model within the **ViPER** simulator which would allow simulations of cryogenic silicon etching. In terms of the work, a new semi-empirical feature-scale model was implemented and integrated into the **ViPER** program code. The model gives the software a possibility to conduct simulations addressing cryogenic high aspect ratio etching of silicon by SF_6/O_2 plasma. Since the developed model provides feature scale simulations without tool scale modelling, it was critically important to conduct a large number of cryoetching experiments in order to estimate numerous internal model parameters in terms of the model calibration. The experiments were conducted in the context of strong and very productive cooperation of the Department of Micro- and Nanoelectronic Systems (MNES) of Ilmenau University of Technology and the Nanofabrication Facility of the Molecular Foundry, Lawrence Berkeley National Laboratory, USA.

By proper calibration, the developed model can help to estimate the parameters (like, for example, fluxes of key plasma species to the sample, sticking coefficients, dependence of etch and

sputtering yields on incident angle and energy of impinging ions, etc.) which are usually very complicated or impossible to determine in terms of experiments. Such an additional insight into the physical and chemical phenomena occurring during the etching process can greatly simplify further development of the process while trying to etch high aspect ratio features with sizes of several nanometers. By reducing the needed number of experiments, the model can significantly economize the time and costs in terms of further research on cryogenic etching of silicon at the nanoscale. Using different plasma etch experiments for calibration and testing of the model, it was shown that resulting simulated profiles are in a very good agreement with experimental results.

Using the model, simulated profiles are matched to those obtained in experiments as a function of process and substrate conditions (varying O_2 content in the feed gas, rf source power, feature size). A key insight from this work is that the passivation layer integrity changes with feature size and process conditions. This arises because the SiO_xF_y layer composition is not constant as a function of features size for the same plasma conditions. For instance, Knudsen transport will change the oxygen content with feature size allowing the SiO_xF_y to vary. This change in passivation integrity is reflected with a parameterized sputtering yield for oxygen which is varied as a function of feature size. Simulating this dependence allows us to understand why profile angle changes so dramatically as function of feature size at the sub-100 nm nanoscale[13, 14].

Extending the model to the deep nanoscale, the author of this work was able to simulate silicon etching of 25 nm half-pitch using a very thin mask derived from block copolymer lithography. The model showed that the experimental finding that nanoscale features need more oxygen for vertical anisotropic profiles[13, 14], is a consequence of the combination of Knudsen transport depleting oxygen faster than fluorine due to the higher sticking coefficient of oxygen and the SiO_xF_y passivation layer sputtering yield is strongly dependent on the oxygen content in the feed gas.

As a perspective for the developed model, the author of this work sees its further extension by various calibrations with respect to different regimes of plasma etch experiments (different values of the chamber pressure and ICP power), depending on the demands of further research in terms of cryogenic silicon etching by SF_6/O_2 plasma.

Appendix A

Neumann boundary condition between two insulators

The developed charging effect simulation model should calculate electric fields induced by surface charging of the insulating materials of the sample. Electric field does not vanish in non conductive materials. This becomes an additional issue for the formulation of a Neumann boundary condition if the electric field in these materials should also be taken into account. In this section, we will discuss the boundary conditions in a particular boundary node, representing non-zero surface charge density and lying on the interface between two insulators.

For further considerations, Eq. 7.16 plays a crucial role and therefore is illustrated here once more:

$$\varepsilon_2 E_{n2} - \varepsilon_1 E_{n1} = \sigma. \quad (\text{A.1})$$

The equation shows interface condition for the electric intensity vector between two media with permittivities ε_1 and ε_2 . E_{n1} and E_{n2} stand for the corresponding normal components of the electric intensity vector in these media at the interface between them. σ is the homogeneously distributed surface charge density at the selected infinitesimal interface area. Being already discussed in section **7.5.1: Definition of the boundary conditions**, variables E_{n1} and E_{n2} are two unknowns in the equation. The contributions from both of them should be determined in order to consider Neumann boundary condition at the interface of the media.

To do that, let us consider a line segment S_{bi} with endpoints B_1 and B_2 . S_{bi} lies on the interface between two insulating materials with permittivities ε_1 and ε_2 , belonging simultaneously to two triangular finite elements T_{i1} and T_{i2} (see Fig. A.01). P_1 and P_2 are the vertices of appropriately T_{i1} and T_{i2} , not lying on the boundary and representing different materials. Considering the boundary segment from each of the elements, \vec{n}_{i1} and \vec{n}_{i2} are the corresponding outer normal vectors with respect to T_{i1} and T_{i2} (see Fig. A.01).

Solving Eq. A.1 for E_{n1} results in

$$E_{n1} = -\frac{\sigma}{\varepsilon_1} + \frac{\varepsilon_2}{\varepsilon_1} E_{n2}, \quad (\text{A.2})$$

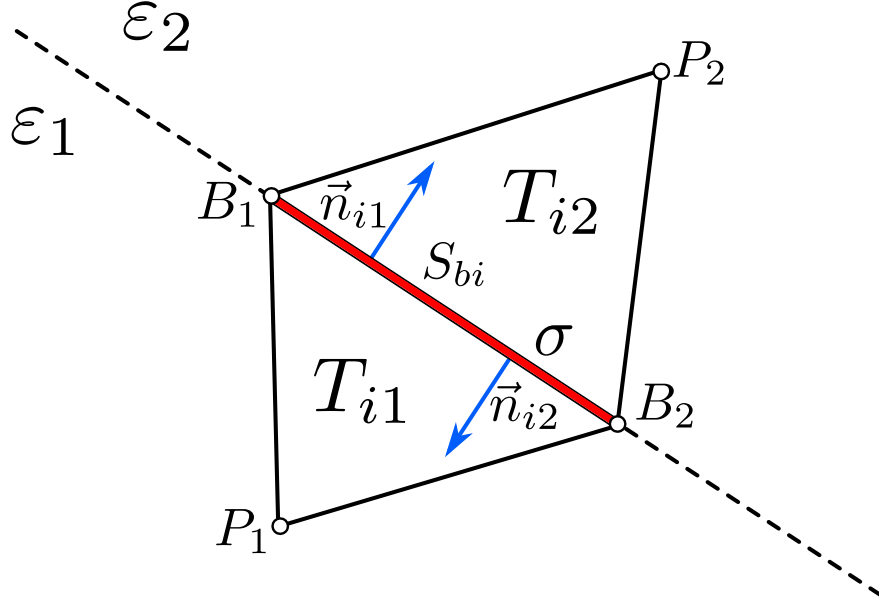


Figure A.01: Boundary segment between two insulating media with permittivities ε_1 and ε_2 . T_{i1} and T_{i2} are the corresponding boundary interface finite elements. \vec{n}_{i1} and \vec{n}_{i2} – outer normal vectors on the boundary with respect to appropriately T_{i1} and T_{i2} . Charge density σ is considered homogeneously distributed along the boundary segment.

Recalling the directions of \vec{E}_{n1} and \vec{E}_{n2} vectors, that were determined in section **7.5.1: Definition of the boundary conditions** (the direction is the same with that of \vec{n}_{i1}), Eq. A.2 can be rewritten with respect to the direction of \vec{n}_{i1} vector:

$$\vec{E}_{n1} \cdot \vec{n}_{i1} = -\frac{\sigma}{\varepsilon_1} + \frac{\varepsilon_2}{\varepsilon_1} \vec{E}_{n2} \cdot \vec{n}_{i2} \quad \Leftrightarrow \quad E_{1,\vec{n}_{i1}} = -\frac{\sigma}{\varepsilon_1} + \frac{\varepsilon_2}{\varepsilon_1} E_{2,\vec{n}_{i1}}, \quad (\text{A.3})$$

where $E_{1,\vec{n}_{i1}} = E_{n1}$ and $E_{2,\vec{n}_{i1}} = E_{n2}$.

Using Eq. 7.3, we obtain the first of the two contributions of the normal derivative to the inhomogeneous Neumann boundary condition at a particular node of the interface between two insulators:

$$\left[\frac{\partial \varphi}{\partial \vec{n}_{i1}} \right]_1 = \frac{\sigma}{\varepsilon_1} - \frac{\varepsilon_2}{\varepsilon_1} E_{2,\vec{n}_{i1}}, \quad (\text{A.4})$$

where $E_{2,\vec{n}_{i1}}$ is the component of the electric intensity vector in finite element T_{i2} with respect to \vec{n}_{i1} vector.

The main idea of the developed approach is to express $E_{2,\vec{n}_{i1}}$ on element T_{i2} using its node variables. Having such an expression would allow to eliminate the unknown variable $E_{2,\vec{n}_{i1}}$ by means of modification of the FEM linear equation system due to the obtained node variables' coefficients – once the coefficients are calculated, they are added to the appropriate components of the FEM stiffness matrix.

For the derivation, an arbitrary triangular finite element T_i will be used. Let φ_1 , φ_2 and φ_3 be the node variables of T_i . φ_x and φ_y stand for the derivatives of the electric potential distribution approximating function φ correspondingly with respect to x and y . We also introduce vector

$\vec{n}(n_x, n_y)$ having the same direction regarding element T_i as that of \vec{n}_{i1} regarding element T_{i2} . The electric field intensity vector inside T_i is denoted as \vec{E}_i in the considered formulation.

According to Eq. 7.3, the components of electric field \vec{E}_i are as follows:

$$E_{i_x} = -\varphi_x, \quad E_{i_y} = -\varphi_y. \quad (\text{A.5})$$

Due to the FEM element-related formulation, used by the charging simulation model and discussed in section **7.5.2.2: The FEM element-related formulation**, derivatives φ_x and φ_y on the reference element T_0 are expressed by means of the chain rule:

$$\begin{aligned} \varphi_x &= \varphi_\xi \xi_x + \varphi_\eta \eta_x, \\ \varphi_y &= \varphi_\xi \xi_y + \varphi_\eta \eta_y. \end{aligned} \quad (\text{A.6})$$

According to the used linear approach, approximating function φ in the reference element T_0 writes as

$$\varphi(\xi, \eta) = \alpha_1 + \alpha_2 \xi + \alpha_3 \eta, \quad (\text{A.7})$$

whereas the needed partial derivatives are as follows:

$$\varphi_\xi = \alpha_2, \quad \varphi_\eta = \alpha_3. \quad (\text{A.8})$$

Due to Eq. 7.57, $\alpha_2 = -\varphi_1 + \varphi_2$ and $\alpha_3 = -\varphi_1 + \varphi_3$. Substituting these values in Eq. A.8, one expresses the derivatives by means of the node variables:

$$\varphi_\xi = -\varphi_1 + \varphi_2, \quad \varphi_\eta = -\varphi_1 + \varphi_3. \quad (\text{A.9})$$

To make the derivation more clear, the expressions for ξ_x , η_x , ξ_y and η_y are illustrated once again:

$$\begin{aligned} \xi_x &= \frac{y_3 - y_1}{J}, & \eta_x &= -\frac{y_2 - y_1}{J}, \\ \xi_y &= -\frac{x_3 - x_1}{J}, & \eta_y &= \frac{x_2 - x_1}{J}, \end{aligned} \quad (\text{A.10})$$

where J is the Jacobian determinant expressed in Eq. 7.38, which writes as

$$J = (x_2 - x_1)(y_3 - y_1) - (x_3 - x_1)(y_2 - y_1). \quad (\text{A.11})$$

Substituting the data from Eq. A.9 and Eq. A.10 into Eq. A.6, one describes derivatives φ_x and φ_y by means of the element node variables:

$$\begin{aligned} \varphi_x &= (-\varphi_1 + \varphi_2) \xi_x + (-\varphi_1 + \varphi_3) \eta_x, \\ \varphi_y &= (-\varphi_1 + \varphi_2) \xi_y + (-\varphi_1 + \varphi_3) \eta_y. \end{aligned} \quad (\text{A.12})$$

Now using Eq. A.5, the electric field components write as

$$\begin{aligned} E_{i_x} &= (\varphi_1 - \varphi_2) \xi_x + (\varphi_1 - \varphi_3) \eta_x, \\ E_{i_y} &= (\varphi_1 - \varphi_2) \xi_y + (\varphi_1 - \varphi_3) \eta_y. \end{aligned} \quad (\text{A.13})$$

After transformation of the equations with respect to the node variables, the expression looks like this:

$$\begin{aligned} E_{i_x} &= \varphi_1(\xi_x + \eta_x) - \varphi_2 \xi_x - \varphi_3 \eta_x, \\ E_{i_y} &= \varphi_1(\xi_y + \eta_y) - \varphi_2 \xi_y - \varphi_3 \eta_y. \end{aligned} \quad (\text{A.14})$$

The projection of \vec{E}_i vector on the direction of \vec{n} vector is expressed as follows:

$$E_{i_n} = \vec{E}_i \cdot \vec{n} = E_{i_x} n_x + E_{i_y} n_y. \quad (\text{A.15})$$

Using Eq. A.14 and Eq. A.15, one obtains the desired expression of electric field component E_{i_n} in terms of the element T_i node variables:

$$\begin{aligned} E_{i_n} &= \varphi_1(\xi_x n_x + \eta_x n_x + \xi_y n_y + \eta_y n_y) + \\ &\quad \varphi_2(-\xi_x n_x - \xi_y n_y) + \\ &\quad \varphi_3(-\eta_x n_x - \eta_y n_y). \end{aligned} \quad (\text{A.16})$$

The sought electric field component is defined unambiguously, depending on the coordinates of any considered finite element (see Eq. A.10 and Eq. A.11).

Following the same way, one determines the remaining second contribution of the normal derivative to the inhomogeneous Neumann boundary condition at a particular node on the interface between two insulators. Taking Eq. A.1 and solving it for E_{n2} results in

$$E_{n2} = \frac{\sigma}{\varepsilon_2} + \frac{\varepsilon_1}{\varepsilon_2} E_{n1}. \quad (\text{A.17})$$

Once again, taking into account the directions of \vec{E}_{n1} and \vec{E}_{n2} vectors, assigned earlier (the directions are opposite to that of \vec{n}_{i2}), Eq. A.17 can be rewritten with respect to the direction of \vec{n}_{i2} vector:

$$\vec{E}_{n2} \cdot \vec{n}_{i2} = \frac{\sigma}{\varepsilon_2} + \frac{\varepsilon_1}{\varepsilon_2} \vec{E}_{n1} \cdot \vec{n}_{i1} \quad \Leftrightarrow \quad E_{2,\vec{n}_{i2}} = -\frac{\sigma}{\varepsilon_2} + \frac{\varepsilon_1}{\varepsilon_2} E_{1,\vec{n}_{i2}}, \quad (\text{A.18})$$

where $E_{2,\vec{n}_{i2}} = -E_{n2}$ and $E_{1,\vec{n}_{i2}} = -E_{n1}$.

Using Eq. 7.3, Eq. A.18 allows to formulate the desired second remaining contribution to the boundary condition:

$$\left[\frac{\partial \varphi}{\partial \vec{n}_{i2}} \right]_2 = \frac{\sigma}{\varepsilon_2} - \frac{\varepsilon_1}{\varepsilon_2} E_{1,\vec{n}_{i2}}, \quad (\text{A.19})$$

where $E_{1,\vec{n}_{i2}}$ is the component of the electric intensity vector in finite element T_{i1} with respect to \vec{n}_{i2} vector.

As a conclusion of the calculations carried out in this section, the developed normal derivative contribution formulas for the inhomogeneous Neumann boundary condition at a particular node on the interface between two insulators are put together:

$$\boxed{\begin{aligned} \left[\frac{\partial \varphi}{\partial \vec{n}_{i1}} \right]_1 &= \frac{\sigma}{\varepsilon_1} - \frac{\varepsilon_2}{\varepsilon_1} E_{2,\vec{n}_{i1}}, \\ \left[\frac{\partial \varphi}{\partial \vec{n}_{i2}} \right]_2 &= \frac{\sigma}{\varepsilon_2} - \frac{\varepsilon_1}{\varepsilon_2} E_{1,\vec{n}_{i2}}. \end{aligned}} \quad (\text{A.20})$$

Final step is to take into account the formulated normal derivative contributions during the FEM linear equation system assembly. To do this, the boundary integral (addressed in Eq. 7.31 and Eq. 7.32) should be considered in the way how it is described in section **7.5.2.4: Consideration of the boundary integral**. Using the same denotation rules employed in the mentioned section, one can obtain from Eq. A.20 the total normal derivative contribution to the boundary condition in the context of any considered m th boundary segment:

$$\chi = \frac{\sigma}{\varepsilon_1} + \frac{\sigma}{\varepsilon_2} - \frac{\varepsilon_2}{\varepsilon_1} E_{2,\vec{n}_{i1}} - \frac{\varepsilon_1}{\varepsilon_2} E_{1,\vec{n}_{i2}}. \quad (\text{A.21})$$

Taking this normal derivative into account will result in contributions to the both, right-hand-side and left-hand-side parts of the FEM linear equation system. Considering signs while moving appropriate terms to the left-hand-side, the normal derivative contributions are given by

$$\chi_l = \frac{\varepsilon_2}{\varepsilon_1} E_{2,\vec{n}_{i1}} + \frac{\varepsilon_1}{\varepsilon_2} E_{1,\vec{n}_{i2}} \quad (\text{A.22})$$

for the left-hand-side, and

$$\chi_r = \frac{\sigma}{\varepsilon_1} + \frac{\sigma}{\varepsilon_2} \quad (\text{A.23})$$

correspondingly for the right-hand-side.

Finally both, χ_l and χ_r , are used in Eq. 7.70 in the context of the boundary integral calculations. This yields the contributions of the inhomogeneous Neumann boundary condition for a particular boundary node on the interface between two insulating materials, leading to modification of the left-hand-side and the right-hand-side of the appropriate equation in the FEM linear equation system.

Bibliography

- [1] Valentyn Ishchuk, Burkhard E. Volland, Maik Hauguth, Mike Cooke, and Ivo W. Rangelow. Charging effect simulation model used in simulations of plasma etching of silicon. *Journal of Applied Physics*, 112(8):084308, 2012.
- [2] Ivo W. Rangelow. Critical tasks in high aspect ratio silicon dry etching for microelectromechanical systems. *Journal of Vacuum Science & Technology A: Vacuum, Surfaces, and Films*, 21(4):1550–1562, 2003.
- [3] Ivo W. Rangelow and Hans Löschner. Reactive ion etching for microelectrical mechanical system fabrication. *Journal of Vacuum Science & Technology B: Microelectronics and Nanometer Structures*, 13(6):2394–2399, 1995.
- [4] I. W. Rangelow, P. Thoren, K. Maßeli, R. Kassing, M. Engelhardt, and S. Schwarzl. Secondary effects of single crystalline silicon deep-trench etching in a chlorine-containing plasma for 3-dimensional capacitor cells. *Microelectronic Engineering*, 5(1-4):387–394, 1986.
- [5] Richard A. Gottscho, Charles W. Jurgensen, and D. J. Vitkavage. Microscopic uniformity in plasma etching. *Journal of Vacuum Science & Technology B: Microelectronics and Nanometer Structures*, 10(5):2133–2147, 1992.
- [6] J. I. Ulacia F. and S. Schwarzl. The physics of plasma etching. *Physica Scripta*, 1991(T35):299, 1991.
- [7] B. E. Volland. *Profile simulations of gas chopping etching processes : model development and comparison with experiments*. PhD thesis, University of Kassel, 2004.
- [8] B. E. Volland, Tzv. Ivanov, and I. W. Rangelow. Profile simulation of gas chopping based etching processes. *Journal of Vacuum Science & Technology B: Microelectronics and Nanometer Structures*, 20(6):3111–3117, 2002.
- [9] Valentyn Ishchuk, Burkhard E. Volland, and Ivo W. Rangelow. ViPER: simulation software for high aspect ratio plasma etching of silicon. *Microsystem Technologies*, 2013.
- [10] M. Hauguth. *Modellierung von Transportprozessen neutraler und ionisierter Spezies in mikro- und nanostrukturierenden Ätzprozessen*. PhD thesis, Ilmenau University of Technology, 2012.

- [11] M. Hauguth, B. E. Volland, V. Ishchuk, D. Dressler, T. Danz, I. W. Rangelow, G. Kokkoris, E. Gogolides, A. Goodyear, and M. Cooke. Integrated plasma processing simulation framework, linking tool scale plasma models with 2D feature scale etch simulator. *Microelectronic Engineering*, 86(4-6):976 – 978, 2009. MNE '08 - The 34th International Conference on Micro- and Nano-Engineering (MNE).
- [12] Shinichi Tachi, Kazunori Tsujimoto, and Sadayuki Okudaira. Low-temperature reactive ion etching and microwave plasma etching of silicon. *Applied Physics Letters*, 52(8):616–618, 1988.
- [13] Zuwei Liu, Ying Wu, Bruce Harteneck, and Deirdre Olynick. Super-selective cryogenic etching for sub-10 nm features. *Nanotechnology*, 24(1):015305, 2013.
- [14] Y. Wu, D. L. Olynick, A. Goodyear, C. Peroz, S. Dhuey, X. Liang, and S. Cabrini. Cryogenic etching of nano-scale silicon trenches with resist masks. *Microelectronic Engineering*, 88(8):2785–2789, 2011.
- [15] Michael. A Lieberman and Allan J. Lichtenberg. *Principles of plasma discharges and materials processing*. Wiley., Hoboken, New Jersey, 111 River Street, Hoboken, NJ, 07030, 2 edition, 2005.
- [16] Gerhard Franz. *Low Pressure Plasmas and Microstructuring Technology*. Springer Berlin Heidelberg, 2009.
- [17] Brian Chapman. *Glow Discharge Processes*. John Wiley & Sons, New York, 1980.
- [18] Francis F. Chen and Jane P. Chang. *Lecture notes on principles of plasma processing*. Kluwer Academic / Plenum Publishers, New York, Boston, Dordrecht, London, Moscow, 233 Spring Street, New York, NY 10013, 2003.
- [19] Gerhard Franz. *Niederdruckplasmen und Mikrostrukturtechnik*. Springer-Verlag Berlin Heidelberg New York, 3 edition, 2004.
- [20] Walter Greiner. *Classical Electrodynamics (Classical Theoretical Physics)*. Springer-Verlag New York, Inc., 175 Fifth Avenue, New York, NY 10010, USA, 1998.
- [21] Christoph Steinbrüchel. Universal energy dependence of physical and ion-enhanced chemical etch yields at low ion energy. *Applied Physics Letters*, 55(19):1960–1962, 1989.
- [22] Mikhail R. Baklanov, Jean-Francois de Marneffe, Denis Shamiryan, Adam M. Urbanowicz, Hualiang Shi, Tatyana V. Rakhimova, Huai Huang, and Paul S. Ho. Plasma processing of low-k dielectrics. *Journal of Applied Physics*, 113(4):041101, 2013.
- [23] John W. Coburn. *Plasma etching and reactive ion etching*. American Institute of Physics, Inc., 335 East 45 Street, New York, NY 10017, USA, 1982.
- [24] F. Becker, I. W. Rangelow, and R. Kassing. Ion energy distributions in SF₆ plasmas at a radio-frequency powered electrode. *Journal of Applied Physics*, 80(1):56, 1996.

- [25] J. Liu, G. L. Huppert, and H. H. Sawin. Ion bombardment in rf plasmas. *Journal of Applied Physics*, 68(8):3916, 1990.
- [26] M. A. Lieberman, J. P. Booth, P. Chabert, J. M. Rax, and M. M. Turner. Standing wave and skin effects in large-area, high-frequency capacitive discharges. *Plasma Sources Science and Technology*, 11(3):283–293, 2002.
- [27] J. Hopwood. Review of inductively coupled plasmas for plasma processing. *Plasma Sources Science and Technology*, 1(2):109–116, 1992.
- [28] N. C. M. Fuller, Vincent M. Donnelly, and Irving P. Herman. Electron temperatures of inductively coupled $\text{Cl}_2 - \text{Ar}$ plasmas. *Journal of Vacuum Science & Technology A: Vacuum, Surfaces, and Films*, 20(1):170, 2002.
- [29] M. D. Henry. *ICP etching of silicon for micro and nanoscale devices*. PhD thesis, California Institute of Technology, 2010.
- [30] R. J. Shul, G. B. McClellan, S. a. Casalnuovo, D. J. Rieger, S. J. Pearton, C. Constantine, C. Barratt, R. F. Karlicek, C. Tran, and M. Schurman. Inductively coupled plasma etching of GaN. *Applied Physics Letters*, 69(8):1119, 1996.
- [31] Banqiu Wu, Ajay Kumar, and Sharma Pamarthy. High aspect ratio silicon etch: A review. *Journal of Applied Physics*, 108(5):051101, 2010.
- [32] J. W. Coburn. Surface-science aspects of plasma-assisted etching. *Applied Physics A Solids and Surfaces*, 59(5):451–458, 1994.
- [33] John W. Coburn and Harold F. Winters. Plasma etching—A discussion of mechanisms. *Journal of Vacuum Science and Technology*, 16(2):391–403, 1979.
- [34] Harold F. Winters. The role of chemisorption in plasma etching. *Journal of Applied Physics*, 49(10):5165–5170, 1978.
- [35] Haruhiko Abe, Masahiro Yoneda, and Nobuo Fujiwara. Developments of Plasma Etching Technology for Fabricating Semiconductor Devices. *Japanese Journal of Applied Physics*, 47(3):1435–1455, 2008.
- [36] I. W. Rangelow. Reactive ion etching for high aspect ratio silicon micromachining. *Surface and Coatings Technology*, 97(1-3):140–150, 1997.
- [37] Shahid Rauf, William J. Dauksher, Stephen B. Clemens, and Kenneth H. Smith. Model for a multiple-step deep Si etch process. *Journal of Vacuum Science & Technology A: Vacuum, Surfaces, and Films*, 20(4):1177, 2002.
- [38] Ivo W. Rangelow. Dry etching-based silicon micro-machining for MEMS. *Vacuum*, 62(2-3):279–291, 2001.

- [39] Daniel L. Flamm, Vincent M. Donnelly, and John A. Mucha. The reaction of fluorine atoms with silicon. *Journal of Applied Physics*, 52(5):3633–3639, 1981.
- [40] Harold F. Winters, D. B. Graves, D. Humbird, and Sven Tougaard. Penetration of fluorine into the silicon lattice during exposure to F atoms, F₂, and XeF₂: Implications for spontaneous etching reactions. *Journal of Vacuum Science & Technology A: Vacuum, Surfaces, and Films*, 25(1):96–103, 2007.
- [41] Vincent M. Donnelly and Daniel L. Flamm. Studies of chemiluminescence accompanying fluorine atom etching of silicon. *Journal of Applied Physics*, 51(10):5273, 1980.
- [42] F. R. McFeely, J. F. Morar, and F. J. Himpsel. Soft X-ray photoemission study of the silicon-fluorine etching reaction. *Surface Science*, 165(1):277–287, 1986.
- [43] J. A. Yarmoff and F. R. McFeely. Mechanism of ion-assisted etching of silicon by fluorine atoms. *Surface Science*, 184(3):389–400, 1987.
- [44] Harold F. Winters and John W. Coburn. Surface science aspects of etching reactions. *Surface Science Reports*, 14(4-6):162–269, 1992.
- [45] Riccardo D’Agostino and Daniel L. Flamm. Plasma etching of Si and SiO₂ in SF₆ – O₂ mixtures. *Journal of Applied Physics*, 52(1):162–167, 1981.
- [46] D. L. Flamm. Mechanisms of silicon etching in fluorine- and chlorine-containing plasmas. *Pure and Applied Chemistry*, 62(9):1709–1720, 1990.
- [47] Peter Sigmund. Theory of Sputtering. I. Sputtering Yield of Amorphous and Polycrystalline Targets. *Physical Review*, 184(2):383–416, 1969.
- [48] Charles W. Jurgensen and Eric S. G. Shaqfeh. Kinetic theory of bombardment induced interface evolution. *Journal of Vacuum Science & Technology B: Microelectronics and Nanometer Structures*, 7(6):1488–1492, 1989.
- [49] Sung-woon Cho, Chang-koo Kim, Jin-Kwan Lee, Sang Heup Moon, and Heeyeop Chae. Angular dependences of SiO₂ etch rates in C₄F₆/O₂/Ar and C₄F₆/CH₂F₂/O₂/Ar plasmas. *Journal of Vacuum Science & Technology A: Vacuum, Surfaces, and Films*, 30(5):051301, 2012.
- [50] I. W. Rangelow. Computer simulation of line edge profiles undergoing ion bombardment. *Journal of Vacuum Science & Technology A: Vacuum, Surfaces, and Films*, 1(2):410–414, 1983.
- [51] J. W. Coburn. Plasma-assisted etching. *Plasma Chemistry and Plasma Processing*, 2(1):1–41, 1982.
- [52] John W. Coburn and Harold F. Winters. Ion- and electron-assisted gas-surface chemistry—An important effect in plasma etching. *Journal of Applied Physics*, 50(5):3189, 1979.
- [53] D. J. Oostra, A. Haring, A. E. de Vries, F. H. M. Sanders, and K. Miyake. Ion-assisted etching of silicon by SF₆. *Applied Physics Letters*, 46(12):1166–1168, 1985.

- [54] D. J. Oostra, A. Haring, A. E. de Vries, F. H. M. Sanders, and G. N. A. van Veen. Etching of silicon by SF₆ induced by ion bombardment. *Nuclear Instruments and Methods in Physics Research Section B: Beam Interactions with Materials and Atoms*, 13(1-3):556–560, 1986.
- [55] R. Kassing and I. W. Rangelow. Etching processes for High Aspect Ratio Micro Systems Technology (HARMST). *Microsystem Technologies*, 3(1):20–27, 1996.
- [56] Riccardo D’Agostino, Francesco Cramarossa, and Francesca Illuzzi. Mechanisms of deposition and etching of thin films of plasma-polymerized fluorinated monomers in radio frequency discharges fed with C₂F₆ – H₂ and C₂F₆ – O₂ mixtures. *Journal of Applied Physics*, 61(8):2754, 1987.
- [57] B. E. Volland and I. W. Rangelow. Aspect ratio dependent plasma polymer deposition of fluorocarbons. *Microelectronic Engineering*, 83(4-9):1174–1177, 2006.
- [58] Burkhard E. Volland, Maik Hauguth, Valentyn Ishchuk, Ivo W. Rangelow, and Andrew L. Goodyear. Irregular film thickness distribution in C₄F₈ inductively coupled plasma polymer deposition. *Microelectronic Engineering*, 98:524–527, 2012.
- [59] K. Tsujimoto, S. Tachi, K. Ninomiya, S. Okudaira, and S. Nishimatsu. A new side wall protection technique in microwave plasma etching using a Chopping Method. In *Extended abstracts of the 18th (1986 international) Conference on solid State Devices and Materials*, pages 229–232, Tokyo, 1986.
- [60] Ivo W. Rangelow. High-resolution tri-level process by downstream-microwave rf-biased etching. *Proc. SPIE 1392, Advanced Techniques for Integrated Circuit Processing*, pages 180–184, 1991.
- [61] I. W. Rangelow. Nano-resolution tri-level process by downstream- microwave rf-biased etching. *Microelectronic Engineering*, 17(1-4):349–352, 1992.
- [62] B. Volland, F. Shi, P. Hudek, H. Heerlein, and Ivo. W. Rangelow. Dry etching with gas chopping without rippled sidewalls. *Journal of Vacuum Science & Technology B: Microelectronics and Nanometer Structures*, 17(6):2768–2771, 1999.
- [63] Pran Mukherjee, Alexander Bruccoleri, Ralf K. Heilmann, Mark L. Schattenburg, Alex F. Kaplan, and L. Jay Guo. Plasma etch fabrication of 60:1 aspect ratio silicon nanogratings with 200 nm pitch. *Journal of Vacuum Science & Technology B: Microelectronics and Nanometer Structures*, 28(6):C6P70, 2010.
- [64] Martin J. Walker. Comparison of Bosch and cryogenic processes for patterning high aspect ratio features in silicon. In Uwe F. W. Behringer and Deepak G. Uttamchandani, editors, *Proceedings of SPIE*, volume 4407, pages 89–99, 2001.
- [65] M. A. Blauw, T. Zijlstra, and E. van der Drift. Balancing the etching and passivation in time-multiplexed deep dry etching of silicon. *Journal of Vacuum Science & Technology B: Microelectronics and Nanometer Structures*, 19(6):2930, 2001.

- [66] M. A. Blauw, G. Craciun, W. G. Sloof, P. J. French, and E. van der Drift. Advanced time-multiplexed plasma etching of high aspect ratio silicon structures. *Journal of Vacuum Science & Technology B: Microelectronics and Nanometer Structures*, 20(6):3106–3110, 2002.
- [67] Johann W Bartha, Johann Greschner, M. Puech, and P. Maquin. Low temperature etching of Si in high density plasma using SF₆/O₂. *Microelectronic Engineering*, 27(1-4):453–456, 1995.
- [68] Gottlieb S. Oehrlein and Yukinori Kurogi. Sidewall surface chemistry in directional etching processes. *Materials Science and Engineering: R: Reports*, 24(4):153–183, 1998.
- [69] X. Mellhaoui, R. Dussart, T. Tillocher, P. Lefauchaux, P. Ranson, M. Boufnichel, and L. J. Overzet. SiO_xF_y passivation layer in silicon cryoetching. *Journal of Applied Physics*, 98(10):104901, 2005.
- [70] J. Pereira, L. E. Pichon, R. Dussart, C. Cardinaud, C. Y. Duluard, E. H. Oubensaid, P. Lefauchaux, M. Boufnichel, and P. Ranson. In situ x-ray photoelectron spectroscopy analysis of SiO_xF_y passivation layer obtained in a SF₆/O₂ cryoetching process. *Applied Physics Letters*, 94(7):071501, 2009.
- [71] R. Dussart, X. Mellhaoui, T. Tillocher, P. Lefauchaux, M. Boufnichel, and P. Ranson. The passivation layer formation in the cryo-etching plasma process. *Microelectronic Engineering*, 84(5-8):1128–1131, 2007.
- [72] T. Tillocher, R. Dussart, X. Mellhaoui, P. Lefauchaux, N. Mekkakia Maaza, P. Ranson, M. Boufnichel, and L. J. Overzet. Oxidation threshold in silicon etching at cryogenic temperatures. *Journal of Vacuum Science & Technology A: Vacuum, Surfaces, and Films*, 24(4):1073–1082, 2006.
- [73] X. Gu, Z. Liu, I. Gunkel, S. T. Chourou, S. W. Hong, D. L. Olynick, and T. P. Russell. High Aspect Ratio Sub-15 nm Silicon Trenches From Block Copolymer Templates. *Advanced Materials*, 24:5688–5694, 2012.
- [74] Muhammad M. Mirza, Haiping Zhou, Philippe Velha, Xu Li, Kevin E. Docherty, Antonio Samarelli, Gary Ternent, and Douglas J. Paul. Nanofabrication of high aspect ratio (~ 50 : 1) sub-10 nm silicon nanowires using inductively coupled plasma etching. *Journal of Vacuum Science & Technology B: Microelectronics and Nanometer Structures*, 30(6):06FF02, 2012.
- [75] Michael A. Lieberman. Analytical solution for capacitive r.f. sheath. Technical Report UCB/ERL M87/71, EECS Department, University of California, Berkeley, 1987.
- [76] Andreas Fichelscher, Ivo W. Rangelow, and Andreas Stamm. Influence of sheath properties on the profile evolution in RIE-processes. In James A. Bondur and Terry R. Turner, editors, *Advanced Techniques for Integrated Circuit Processing*, volume 1392, pages 77–83, 1990.
- [77] Valery A. Godyak and Natalia Sternberg. Dynamic model of the electrode sheaths in symmetrically driven rf discharges. *Phys. Rev. A*, 42(4):2299–2312, 1990.

- [78] E. Kawamura, V. Vahedi, M.A. Lieberman, and C.K. Birdsall. Ion energy distributions in rf sheaths; review, analysis and simulation. *Plasma Sources Science and Technology*, 8(1):R45–R64, 1999.
- [79] Theodoros Panagopoulos and Demetre J. Economou. Plasma sheath model and ion energy distribution for all radio frequencies. *Journal of Applied Physics*, 85(7):3435–3443, 1999.
- [80] John C. Arnold, David C. Gray, and Herbert H. Sawin. Influence of reactant transport on fluorine reactive ion etching of deep trenches in silicon. *Journal of Vacuum Science & Technology B: Microelectronics and Nanometer Structures*, 11(6):2071–2080, 1993.
- [81] M. K. Abachev, Yu. P. Baryshev, V. F. Lukichev, A. A. Orlikovsky, and K. A. Valiev. Aperture effect in plasma etching of deep silicon trenches. *Vacuum*, 42(1-2):129–131, 1991.
- [82] J. Kiihamäki and S. Franssila. Pattern shape effects and artefacts in deep silicon etching. *Journal of Vacuum Science & Technology A: Vacuum, Surfaces, and Films*, 17(4):2280, 1999.
- [83] Henri Jansen, Meint de Boer, Remco Wiegerink, Niels Tas, Edwin Smulders, Christina Neagu, and Miko Elwenspoek. RIE lag in high aspect ratio trench etching of silicon. *Microelectronic Engineering*, 35(1-4):45–50, 1997.
- [84] J. Kiihamäki. Deceleration of silicon etch rate at high aspect ratios. *Journal of Vacuum Science & Technology A: Vacuum, Surfaces, and Films*, 18(4):1385, 2000.
- [85] V. F. Lukichev. A new approach to aspect ratio independent etching. *Microelectronic Engineering*, 41-42:423–426, 1998.
- [86] V. F. Lukichev and V. A. Yunkin. Scaling of silicon trench etch rates and profiles in plasma etching. *Microelectronic Engineering*, 46(1-4):315–318, 1999.
- [87] C. Hedlund, H. O. Blom, and S. Berg. Microloading effect in reactive ion etching. *Journal of Vacuum Science & Technology A: Vacuum, Surfaces, and Films*, 12(4):1962–1965, 1994.
- [88] Wei Guo and Herbert H Sawin. Review of profile and roughening simulation in microelectronics plasma etching. *Journal of Physics D: Applied Physics*, 42(19):194014, 2009.
- [89] N. S. Viswanathan. Simulation of plasma-etched lithographic structures. *Journal of Vacuum Science and Technology*, 16(2):388, 1979.
- [90] John L. Reynolds, Andrew R. Neureuther, and William G. Oldham. Simulation of dry etched line edge profiles. *Journal of Vacuum Science and Technology*, 16(6):1772, 1979.
- [91] I. W. Rangelow, P. Thoren, and R. Kassing. Computer simulation of pattern profiles through physical etching with shadow, trenching, and redeposition. *Microelectronic Engineering*, 3(1-4):631–638, 1985.
- [92] J. Ignacio Ulacia F. and James P. McVittie. A two-dimensional computer simulation for dry etching using monte carlo techniques. *Journal of Applied Physics*, 65(4):1484–1491, 1989.

- [93] M. J. Kushner. Distribution of ion energies incident on electrodes in capacitively coupled rf discharges. *Journal of Applied Physics*, 58(11):4024, 1985.
- [94] P. Thoren, I.W. Rangelow, R. Kassing, and P. Kücher. Three-dimensional simulation of sputter processes for sub- μm technologies. *Microelectronic Engineering*, 9(1-4):621–624, 1989.
- [95] John C. Arnold, Herbert H. Sawin, Manoj Dalvie, and Satoshi Hamaguchi. Simulation of surface topography evolution during plasma etching by the method of characteristics. *Journal of Vacuum Science & Technology A: Vacuum, Surfaces, and Films*, 12(3):620, 1994.
- [96] Burkhard E. Volland and Ivo W. Rangelow. The influence of reactant transport on the profiles of gas chopping etching processes: a simulation approach. *Microelectronic Engineering*, 67-68:338–348, 2003.
- [97] A. S. Shumilov, I. I. Amirov, and V. F. Lukichev. Simulation of the effects of deep grooving in silicon in the plasmochemical cyclic process. *Russian Microelectronics*, 38(6):385–392, 2009.
- [98] D. J. Cooperberg, V. Vahedi, and R. A. Gottscho. Semiempirical profile simulation of aluminum etching in a Cl_2/BCl_3 plasma. *Journal of Vacuum Science & Technology A: Vacuum, Surfaces, and Films*, 20(5):1536, 2002.
- [99] Rodolfo Jun Belen, Sergi Gomez, Mark Kiehlbauch, David Cooperberg, and Eray S. Aydil. Feature-scale model of Si etching in SF_6 plasma and comparison with experiments. *Journal of Vacuum Science & Technology A: Vacuum, Surfaces, and Films*, 23(1):99, 2005.
- [100] Rodolfo Jun Belen, Sergi Gomez, David Cooperberg, Mark Kiehlbauch, and Eray S. Aydil. Feature-scale model of Si etching in SF_6/O_2 plasma and comparison with experiments. *Journal of Vacuum Science & Technology A: Vacuum, Surfaces, and Films*, 23(5):1430, 2005.
- [101] Rodolfo Jun Belen, Sergi Gomez, Mark Kiehlbauch, and Eray S. Aydil. Feature scale model of Si etching in $\text{SF}_6/\text{O}_2/\text{HBr}$ plasma and comparison with experiments. *Journal of Vacuum Science & Technology A: Vacuum, Surfaces, and Films*, 24(2):350–361, 2006.
- [102] George Kokkoris, Andy Goodyear, Mike Cooke, and Evangelos Gogolides. A global model for C_4F_8 plasmas coupling gas phase and wall surface reaction kinetics. *Journal of Physics D: Applied Physics*, 41(19):195211, 2008.
- [103] George. Kokkoris, Apostolos Panagiotopoulos, Andy Goodyear, Mike Cooke, and Evangelos Gogolides. A global model for SF_6 plasmas coupling reaction kinetics in the gas phase and on the surface of the reactor walls. *Journal of Physics D: Applied Physics*, 42(5):055209, 2009.
- [104] M. Hauguth, T. Danz, B. E. Volland, V. Ishchuk, D. Dressler, and I. W. Rangelow. New method for the precise flux calculation of neutrals for arbitrary surfaces in profile etch simulations. *Microelectronic Engineering*, 85:982–984, 2008.
- [105] Gyeong S. Hwang and Konstantinos P. Giapis. On the origin of the notching effect during etching in uniform high density plasmas. *Journal of Vacuum Science & Technology B: Microelectronics and Nanometer Structures*, 15(1):70–87, 1997.

- [106] Demetre J. Economou and Richard C. Alkire. Effect of potential field on ion deflection and shape evolution of trenches during plasma-assisted etching. *Journal of The Electrochemical Society*, 135(4):941–949, 1988.
- [107] J. C. Arnold and H. H. Sawin. Charging of pattern features during plasma etching. *Journal of Applied Physics*, 70(10):5314–5317, 1991.
- [108] Hiroki Ootera, Tatsuo Oomori, Mutumi Tuda, and Keisuke Namba. Simulation of ion trajectories near submicron-patterned surface including effects of local charging and ion drift velocity toward wafer. *Japanese Journal of Applied Physics*, 33(Part 1, No. 7B):4276–4280, 1994.
- [109] Takashi Kinoshita, Masami Hane, and James P. McVittie. Notching as an example of charging in uniform high density plasmas. *Journal of Vacuum Science & Technology B: Microelectronics and Nanometer Structures*, 14(1):560–565, 1996.
- [110] M. A. Vyvoda, M. Li, and D. B. Graves. Hardmask charging during Cl_2 plasma etching of silicon. *Journal of Vacuum Science & Technology A: Vacuum, Surfaces, and Films*, 17(6):3293–3307, 1999.
- [111] Jun Matsui, Nobuhiko Nakano, Zoran Lj. Petrović, and Toshiaki Makabe. The effect of topographical local charging on the etching of deep-submicron structures in SiO_2 as a function of aspect ratio. *Applied Physics Letters*, 78(7):883–885, 2001.
- [112] Arnulf Kost. *Numerische Methoden in der Berechnung elektromagnetischer Felder*. Springer-Verlag, Berlin Heidelberg, 1994.
- [113] John P. Boyd. *Chebyshev and Fourier Spectral Methods*. DOVER Publications, Inc., 31 East 2nd Street, Mineola, New York 11501, 2 edition, 2001.
- [114] Hans Rudolf Schwarz. *Methode der finiten Elemente: Eine Einführung unter besonderer Berücksichtigung der Rechenpraxis*. Stuttgart: Teubner, 1991.
- [115] John T. Katsikadelis. *Boundary Elements Theory and Applications*. Elsevier Science & Technology, Oxford, United Kingdom, 2002.
- [116] O. C. Zienkiewicz and R. L. Taylor. *The finite element method*, volume 1. Butterworth-Heinemann, Linacre House, Jordan Hill, Oxford OX2 8DP, 5 edition, 2000.
- [117] Jonathan Shewchuk. Triangle: Engineering a 2d quality mesh generator and delaunay triangulator. In Ming Lin and Dinesh Manocha, editors, *Applied Computational Geometry Towards Geometric Engineering*, volume 1148 of *Lecture Notes in Computer Science*, pages 203–222. Springer Berlin / Heidelberg, 1996.
- [118] M. Boufnichel, S. Aachboun, F. Grangeon, P. Lefauchaux, and P. Ranson. Profile control of high aspect ratio trenches of silicon. I. Effect of process parameters on local bowing. *Journal of Vacuum Science & Technology B: Microelectronics and Nanometer Structures*, 20(4):1508–1513, 2002.

- [119] M. Boufnichel, S. Aachboun, P. Lefauchaux, and P. Ranson. Profile control of high aspect ratio trenches of silicon. II. Study of the mechanisms responsible for local bowing formation and elimination of this effect. *Journal of Vacuum Science & Technology B: Microelectronics and Nanometer Structures*, 21(1):267–273, 2003.
- [120] M. Boufnichel, P. Lefauchaux, S. Aachboun, R. Dussart, and P. Ranson. Origin, control and elimination of undercut in silicon deep plasma etching in the cryogenic process. *Microelectronic Engineering*, 77(3-4):327–336, 2005.
- [121] G. Craciun, M. A. Blauw, E. Van Der Drift, P. M. Sarro, and P. J. French. Temperature influence on etching deep holes with SF₆/O₂ cryogenic plasma. *Journal of Micromechanics and Microengineering*, 12(4):390–394, 2002.
- [122] Aref Bakhtazad, Xuan Huo, and Jayshri Sabarinathan. Cryogenic shallow reactive ion etch process for profile control on silicon on insulator platform. *Journal of Vacuum Science & Technology B: Microelectronics and Nanometer Structures*, 29(4):041001, 2011.
- [123] Ü. Sökmen, A. Stranz, S. Fündling, H-H. Wehmann, V. Bandalo, A. Bora, M. Tornow, A. Waag, and E. Peiner. Capabilities of ICP-RIE cryogenic dry etching of silicon: review of exemplary microstructures. *Journal of Micromechanics and Microengineering*, 19(10):105005, 2009.
- [124] Sergi Gomez, Rodolfo Jun Belen, Mark Kiehlbauch, and Eray S. Aydil. Etching of high aspect ratio structures in Si using SF₆/O₂ plasma. *Journal of Vacuum Science & Technology A: Vacuum, Surfaces, and Films*, 22(3):606–615, 2004.
- [125] G. Marcos, A. Rhallabi, and P. Ranson. Monte Carlo simulation method for etching of deep trenches in Si by a SF₆/O₂ plasma mixture. *Journal of Vacuum Science & Technology A: Vacuum, Surfaces, and Films*, 21(1):87–95, 2003.
- [126] G. Marcos, A. Rhallabi, and P. Ranson. Topographic and kinetic effects of the SF₆/O₂ rate during a cryogenic etching process of silicon. *Journal of Vacuum Science & Technology B: Microelectronics and Nanometer Structures*, 22(4):1912–1922, 2004.
- [127] G. Marcos, A. Rhallabi, and P. Ranson. Properties of deep etched trenches in silicon: Role of the angular dependence of the sputtering yield and the etched species redeposition. *Applied Surface Science*, 254(11):3576–3584, 2008.
- [128] M. A. Blauw, E. van der Drift, G. Marcos, and A. Rhallabi. Modeling of fluorine-based high-density plasma etching of anisotropic silicon trenches with oxygen sidewall passivation. *Journal of Applied Physics*, 94(10):6311, 2003.
- [129] Takahiro Maruyama, Takeshi Narukage, Ryota Onuki, and Nobuo Fujiwara. High-aspect-ratio deep Si etching in SF₆/O₂ plasma. I. Characteristics of radical reactions with high-aspect-ratio patterns. *Journal of Vacuum Science & Technology B: Microelectronics and Nanometer Structures*, 28(4):854–861, 2010.

- [130] Takahiro Maruyama, Takeshi Narukage, Ryota Onuki, and Nobuo Fujiwara. High-aspect-ratio deep Si etching in SF₆/O₂ plasma. II. Mechanism of lateral etching in high-aspect-ratio features. *Journal of Vacuum Science & Technology B: Microelectronics and Nanometer Structures*, 28(4):862–868, 2010.
- [131] Tomoharu Ikeda, Hirokazu Saito, Fumiaki Kawai, Kimimori Hamada, Toshimitsu Ohmine, Hideki Takada, and Vaibhav Deshpande. Development of SF₆/O₂/Si plasma etching topography simulation model using new flux estimation method. *2011 International Conference on Simulation of Semiconductor Processes and Devices*, pages 115–118, 2011.
- [132] J. W. Coburn and Harold F. Winters. Conductance considerations in the reactive ion etching of high aspect ratio features. *Applied Physics Letters*, 55(26):2730, 1989.
- [133] H. M. Anderson, J. A. Merson, and R W Light. A Kinetic Model for Plasma Etching Silicon in a SF₆/O₂ RF Discharge. *IEEE Transactions on Plasma Science*, 14(2):156–164, 1986.
- [134] Werner W. Brandt and Takuya Honda. Mass spectrometric transient study of dc plasma etching of Si in SF₆/O₂ mixtures. *Journal of Applied Physics*, 60(5):1595, 1986.
- [135] K. R. Ryan and I. C. Plumb. Gas-phase reactions in plasmas of SF₆ with O₂ in He. *Plasma Chemistry and Plasma Processing*, 8(3):263–280, 1988.
- [136] K. R. Ryan and I. C. Plumb. A model for the etching of silicon in SF₆/O₂ plasmas. *Plasma Chemistry and Plasma Processing*, 10(2):207–229, 1990.
- [137] Robert J Hoekstra and Mark J Kushner. Predictions of ion energy distributions and radical fluxes in radio frequency biased inductively coupled plasma etching reactors. *Journal of Applied Physics*, 79(5):2275, 1996.
- [138] Wei Guo and Herbert H. Sawin. Modeling of the angular dependence of plasma etching. *Journal of Vacuum Science & Technology A: Vacuum, Surfaces, and Films*, 27(6):1326, 2009.
- [139] Shahram Abdollahi-Alibeik, James P. McVittie, Krishna C. Saraswat, Valeriy Sukharev, and Philippe Schoenborn. Analytical modeling of silicon etch process in high density plasma. *Journal of Vacuum Science & Technology A: Vacuum, Surfaces, and Films*, 17(5):2485–2491, 1999.
- [140] Jane P. Chang, Arpan P. Mahorowala, and Herbert H. Sawin. Plasma-surface kinetics and feature profile evolution in chlorine etching of polysilicon. *Journal of Vacuum Science & Technology A: Vacuum, Surfaces, and Films*, 16(1):217–224, 1998.
- [141] Steven A. Vitale, Heeyeop Chae, and Herbert H. Sawin. Silicon etching yields in F₂, Cl₂, Br₂, and HBr high density plasmas. *Journal of Vacuum Science & Technology A: Vacuum, Surfaces, and Films*, 19(5):2197–2206, 2001.
- [142] David C. Gray, I. Tepermeister, and Herbert H. Sawin. Phenomenological modeling of ion-enhanced surface kinetics in fluorine-based plasma etching. *Journal of Vacuum Science & Technology B: Microelectronics and Nanometer Structures*, 11(4):1243–1257, 1993.

- [143] Vincent M. Donnelly and Avinoam Kornblit. Plasma etching: Yesterday, today, and tomorrow. *Journal of Vacuum Science & Technology A: Vacuum, Surfaces, and Films*, 31(5):050825, 2013.
- [144] B. A. Helmer and D. B. Graves. Molecular dynamics simulations of fluorosilyl species impacting fluorinated silicon surfaces with energies from 0.1 to 100 eV. *Journal of Vacuum Science & Technology A: Vacuum, Surfaces, and Films*, 15(4):2252–2261, 1997.
- [145] Amand Pateau, Ahmed Rhallabi, Marie-Claude Fernandez, Mohamed Boufnichel, and Fabrice Roqueta. Modeling of inductively coupled plasma SF₆/O₂/Ar plasma discharge: Effect of O₂ on the plasma kinetic properties. *Journal of Vacuum Science & Technology A: Vacuum, Surfaces, and Films*, 2013. doi: 10.1116/1.4853675.
- [146] Gottlieb S. Oehrlein, Raymond J. Phaneuf, and David B. Graves. Plasma-polymer interactions: A review of progress in understanding polymer resist mask durability during plasma etching for nanoscale fabrication. *Journal of Vacuum Science & Technology B: Microelectronics and Nanometer Structures*, 29(1):010801, 2011.
- [147] Nathan Marchack and Jane P Chang. Perspectives in nanoscale plasma etching: what are the ultimate limits? *Journal of Physics D: Applied Physics*, 44(17):174011, 2011.

List of Figures

2.1	Qualitative behaviour of sheath and presheath in contact with a plasma reactor wall	11
3.1	Approximate time-average potential versus distance plot for a capacitively coupled planar rf glow discharge system	17
3.2	Approximate cathode and plasma potential waveforms for a capacitively coupled discharge	18
4.1	Three basic types of reaction mechanisms in terms of plasma etching of silicon	25
4.2	Directionality of etching processes	26
5.1	Charging effect at plasma etching of SOI wafer	37
6.1	Common architecture of the ViPER simulator	42
7.1	Notching effect during plasma etching of silicon on SOI wafer using an SF ₆ /C ₄ F ₈ gas chopping approach	46
7.2	Position of the developed charging effect simulation model in the architecture of the ViPER simulator	48
7.3	Schematic representation of the implemented charging effect simulation model	49
7.4	Definition of the charging effect simulation area according to the developed model	51
7.5	Representation of the boundary conditions used by the charging model for electric field calculation in the simulation area	53
7.6	Interface conditions for electric displacement field	54
7.7	Representation of a linear shape function for finite element method	59
7.8	Mapping between the considered element T_i and the reference element T_0 by means of linear transformation	63
7.9	Behaviour of linear shape functions on the boundary of the considered triangular finite element	70

7.10	Two ways of meshing of the charging simulation area	72
7.11	Electric potential distribution calculated by the developed model for typical surface charge distribution during dry silicon etching for SOI wafers	72
7.12	Particle movement over the area of a triangular finite element under the influence of homogeneous electric field	74
7.13	Etching of silicon layer on a SOI wafer using gas chopping process	76
7.14	Simulated surface profile without utilization of the implemented charging effect simulation model	76
7.15	Simulated intermediate surface profile with utilization of the implemented charging effect simulation model	77
7.16	Electric potential distribution in the area of interest at the final stage of the profile simulation	77
7.17	Trajectories of positive ions during the simulation	78
7.18	Meshing by the FEM solver	78
7.19	Resulting surface profile after utilization of the implemented charging effect simulation model	79
8.1	Examples of ion angular distribution functions (IADFs) using Gaussian distribution	85
8.2	The form of the yield dependency on the ion angle of incidence in the developed cryo etch model	89
8.3	Calibration of chemical etch parameters	93
8.4	Calibration of ion-assisted etch parameters	94
8.5	<i>Calibration of the model using different values of oxygen content in the feed gas. Used SF₆/O₂ gas flow ratios: (a) 50–0 sccm, (b) 48–2 sccm, (c) 46–4 sccm, (d) 44–6 sccm, (e) 42–8 sccm, (f) 40–10 sccm, (g) 38–12 sccm. Mask height before etching: 700 nm.</i>	97
8.6	<i>Nanoscale silicon cryoetching experiments conducted by Liu et al[13]. The original picture can be found in Ref. 13. Different feature sizes after 20 s etching, 10, 20, 30, 40, 90, 110 nm from left to right. Mask height before etching: 60 nm.</i>	99
8.7	Utilization of the implemented model for simulation of cryogenic silicon etching at the nanoscale (features of 35 nm width)	101
A.01	Boundary segment between two insulating media with permittivities ϵ_1 and ϵ_2	110

List of Tables

8.1	<i>Common plasma etch recipe parameters used in the experiments</i>	83
8.2	<i>Summary of the model parameters to be determined.</i>	90
8.3	<i>Plasma etch recipe used for the calibration of chemical etching parameters.</i>	92
8.4	<i>The model chemical etch parameters' values determined during the calibration.</i>	93
8.5	<i>Plasma etch recipe used for the calibration of ion-assisted etching parameters.</i>	93
8.6	<i>The model parameters for simulating the best match with experiments described in Table 8.5.</i>	95
8.7	<i>Plasma etch recipe used for the calibrations with different oxygen content in the feed gas.</i>	95
8.8	<i>The model parameter values determined during the calibration with different oxygen content in the gas feed.</i>	98
8.9	<i>Plasma etch recipe used for the anisotropic nanoscale cryoetching of 35 nm wide features.</i>	100
8.10	<i>The model parameters for simulating the best match with the experiment in terms of the anisotropic nanoscale cryo etching of 35 nm wide features</i>	102

List of publications

- [1] Valentyn Ishchuk, Burkhard E. Volland, Maik Hauguth, Mike Cooke, and Ivo W. Rangelow. Charging effect simulation model used in simulations of plasma etching of silicon. *Journal of Applied Physics*, 112(8):084308, 2012. doi: 10.1063/1.4759005.
- [2] Valentyn Ishchuk, Burkhard E. Volland, and Ivo W. Rangelow. ViPER: simulation software for high aspect ratio plasma etching of silicon. *Microsystem Technologies*, 2013. ISSN 0946-7076. doi: 10.1007/s00542-013-1926-5.
- [3] M. Hauguth, B. E. Volland, V. Ishchuk, D. Dressler, T. Danz, I. W. Rangelow, G. Kokkoris, E. Gogolides, A. Goodyear, and M. Cooke. Integrated plasma processing simulation framework, linking tool scale plasma models with 2D feature scale etch simulator. *Microelectronic Engineering*, 86(4-6):976 – 978, 2009. ISSN 0167-9317. doi: 10.1016/j.mee.2009.02.012.
- [4] Burkhard E. Volland, Maik Hauguth, Valentyn Ishchuk, Ivo W. Rangelow, and Andrew L. Goodyear. Irregular film thickness distribution in C_4F_8 inductively coupled plasma polymer deposition. *Microelectronic Engineering*, 98:524–527, 2012. ISSN 01679317. doi: 10.1016/j.mee.2012.07.058.
- [5] M. Hauguth, T. Danz, B. E. Volland, V. Ishchuk, D. Dressler, and I. W. Rangelow. New method for the precise flux calculation of neutrals for arbitrary surfaces in profile etch simulations. *Microelectronic Engineering*, 85:982–984, May 2008. ISSN 0167-9317. doi: 10.1016/j.mee.2008.01.019.

Curriculum Vitae

Name	Ishchuk
First Name	Valentyn
Birthday	November 23rd, 1981
Birthplace	Kyiv, Ukraine
Father	Mykola Ishchuk
Mother	Olena Ishchuk
Family status	married
Nationality	Ukrainian

1989 – 1999 Secondary school with advanced study of English, Kyiv, Ukraine

June 20th, 1999 Certificate of Complete General Secondary Education

1999 – 2005 Studies of Computer-Aided Design (CAD) and Electronics, National Technical University of Ukraine (Kyiv Polytechnic Institute), Kyiv, Ukraine

November 1st, 2004 – six month professional internship, DAAD stipend, Informatics and
April 30th, 2005 Computational Mathematics, Magdeburg-Stendal University of Applied Sciences, Magdeburg, Germany

2004 – 2005 Diploma thesis "Multigrid methods for solving systems of discontinuous equations of very big dimensions, arising from finite element methods" under guidance of Prof. Dr. A. I. Petrenko

June 30th, 2005 Diploma degree

March 1st, 2007 Scientific assistant and a PhD student in the research group of Prof. Dr. Ivo W. Rangelow, Department of micro- and nanoelectronic systems, Faculty of electrical engineering, Ilmenau University of Technology, Ilmenau, Germany

Theses

1. Low-pressure, high density plasmas are used for anisotropic etching of materials. In high aspect ratio (HAR) silicon etching, plasma reactors with an inductively coupled plasma (ICP) source are most widely used, providing highly precise pattern transfer.
2. In terms of silicon dry etching, the highest etching rate can be achieved by using fluorine-containing processing gases (like SF_6).
3. Fluorine atoms attack silicon spontaneously, resulting in isotropic etch profiles. In order to keep high etch rates by fluorine and provide anisotropic etching, the plasma chemistry should contain species which adsorb on the silicon surface but do not etch it, creating an inhibitor film.
4. Inhibitor film at the etched silicon feature is removed by energetic ions only at the trench bottom. Thus, the trench sidewalls are protected from further fluorine attacks providing the profile anisotropy.
5. Keeping the sample at low temperature and adding oxygen to a typical SF_6 plasma discharge results in anisotropic, high aspect ratio profile due to adsorption of oxygen atoms on the silicon surface and creation of SiO_xF_y inhibitor film.
6. For the first time, the developed in the context of this work simulation model demonstrates simulation of cryogenic plasma etching of silicon at the nanoscale.
7. Local charging of insulating surfaces of the sample can induce electric fields sufficient for altering the trajectories of low energetic ions coming from plasma, which can lead to lateral etching thus greatly complicating the profile control.
8. The developed in terms of this work charging effect simulation model uses finite element method (FEM) together with a triangular mesh generator for electric field calculations. Hence, the model is able to handle complicated geometries of the calculation area.
9. In addition to the calculation of electric field in the gas-phase within the etched microstructure, the developed charging effect simulation model is able to consider electric field also in insulating materials of the sample.
10. For the first time, the developed charging effect simulation model can simulate the influence of local surface charging during the entire course of etching process yielding plausible results, which are confirmed by comparison with a real experiment. The model is able to capture well different types of feature profile distortions arising as a consequence of the local surface charging. Thus, the model proves its capability to reflect well the physics of the charging phenomenon.